TRANSPARENT CONDUCTING FILMS:

EXPERIMENT, THEORY AND APPLICATION

CHEN ZHANGXIAN

(M. Eng., HEFEI UNIVERSITY OF TECHNOLOGY)

A THESIS SUBMITTED

FOR THE DEGREE OF DOCTOR OF

PHILOSOPHY

DEPARTMENT OF CHEMISTRY

NATIONAL UNIVERSITY OF SINGAPORE

2014

DECLARATION

I hereby declare that this thesis is my original work and it has been written by me in its entirety, under the supervision of Professor Xu Guo Qin and Associate Professor Cheng Hansong, (in the laboratory S5-05-04), Chemistry Department, National University of Singapore, between Jan., 2010 and Dec., 2013.

I have duly acknowledged all the sources of information which have been used in the thesis.

This thesis has also not been submitted for any degree in any university previously.

The content of the thesis has been partly published in:

1. Fabrication of Highly Transparent and Conductive Indium-Tin Oxide Thin Films with a High Figure of Merit via Solution Processing

   Chen Z. X., Li W. C., Li R., Zhang Y. F., Xu G. Q., Cheng H. S.

   Langmuir, **2013**, 29, 13836-13842
2. Surface Modification of ITO Nanoparticles by Trimesic Acid: A Combined Experimental and DFT Study

   Chen Z. X., Zhang Q. F., Huang L., Li R., Li W. C., Xu G. Q., Cheng H. S.

   Journal of Physical Chemistry C, **2014**, 118, 21244-21249

Name	Signature	Date

ACKNOWLEDGEMENT

First and foremost I wish to thank my supervisor Professor Xu Guo Qin and co-supervisor Associate Professor Cheng Hansong for their valuable guidance and support during my PhD study. I must also thank my co-supervisors Professor Lin Jianyi (ICES, ASTAR) and Dr. Zhong Ziyi (ICES, ASTAR) for the useful discussion of experimental details. I'm also very grateful to Dr. James George Highfield (ICES, ASTAR) and his student Dr. Gong Dangguo for their kind arrangement of diffuse reflectance infrared Fourier transform spectroscopic measurement.

I would like to thank all the research staffs and students in Professor Xu Guo Qin's and Associate Professor Cheng Hansong's groups to provide me kind help and support. Especially I must thank Dr. Zhang Qingfan since he sacrificed his valuable time to guide me on the computational details.

National University of Singapore is greatly appreciated for providing me the research scholarship during my PhD study. High performance computing center is also acknowledged for the computational resources.

Finally, I am deeply indebted to my wife Qingxiu and my lovely daughter Candice for their sacrifice, love and constant support.

TABLE OF CONTENTS

DECLARATION ..... **i**

ACKNOWLEDGEMENT ..... **ii**

TABLE OF CONTENTS ..... **iii**

SUMMARY ..... **vii**

LIST OF TABLES ..... **x**

LIST OF FIGURES ..... **xi**

LIST OF PUBLICATIONS ..... **xv**

Chapter 1 Introduction **1**

1.1 Transparent Conductors 1

1.1.1 Transparent Conducting Oxides 1

1.1.1a: CdO-based TCOs 2

1.1.1b: ZnO-based TCOs 4

1.1.1c: SnO_2-based TCOs 5

1.1.1d: In_2O_3-based TCOs 6

1.1.1e: Other TCOs 9

1.1.2 Non-oxides 9

Graphene and Carbon Nanotubes 9

1.2 Properties of Transparent Conducting Oxides 10

1.2.1 Electrical Conductivity 10

1.2.1a: Carrier Concentration—n 11

1.2.1b: Carrier Mobility—μ 13

1.2.2 Optical Property 15

1.2.2a: Band Gap—Eg 15

1.2.2b: Plasma Frequency—λ_p 16

1.2.3 Figure of Merit—FOM 17
1.3 Depositions of Transparent Conducting Films 17
1.3.1 Vapor Deposition 18
1.3.2 Solution Deposition 18
1.4 Application 20
Surface Modification of ITO films for Applications in OLED and OPV 20
1.5 Motivations and Objectives 21
1.5.1 Solution Deposition of ITO Transparent Conducting Film 21
1.5.2 Theoretical Investigation of n-type Doped In_2O_3 Transparent Conductors 22
1.5.3 Single Layer Gallium Sulfide Transparent Conductor 23
1.5.4 Surface Modification of ITO Nanoparticles by Trimesic Acid 23
References 24
Chapter 2 Solution Deposition of Highly Transparent and Conductive ITO Thin Films with a High Figure of Merit 32
2.1 Introduction 32
2.2 Experiments 35
2.2.1 Film Deposition 36
2.2.2 Characterization 36
2.3 Results and Discussion 37
2.3.1 Crystal Structure and Film Resistivity 37
2.3.2 Film Microstructure and Morphology 39
2.3.3 Surface Composition of ITO Film 40
2.3.4 Optical, Electrical Property and Figure of Merit 43
2.3.5 Chelation Effect 45

2.4 Conclusion.....49
References.....49
Chapter 3 The Electronic Structures of n-type Doped Indium Oxides as the Transparent Conductors.....53
3.1 Introduction.....53
3.2 Computational Details.....54
3.3 Results and Discussion.....55
3.3.1 The Geometrical Structures of Pristine and n-type Doped In_2O_3.....55
3.3.2 The Electronic Structures of Pristine and n-type Doped In_2O_3.....57
3.3.3 Atomic Orbitals, Bader Charge Analysis and Charge Density Differences.....65
3.3.4 Formation Energies and Transition Levels.....70
3.4 Conclusion.....75
References.....76
Chapter 4 Geometrical Structures, Electronic and Transport Properties of a Novel Two-Dimensional GaS Transparent Conductor.....79
4.1 Introduction.....79
4.2 Computational Details.....80
4.3 Results and Discussion.....81
4.3.1 The Geometrical Structures of Bulk, Pure and H-doped 2-D GaS..81
4.3.2 The Electronic Structures of Bulk, Pure and H-doped 2-D GaS.....88
4.3.3 The Band Structures of Bulk, Pure and H-doped 2-D GaS.....92
4.3.4 The Transport Properties of H-doped 2-D GaS.....97
4.4 Conclusion.....101
References.....102

Chapter 5 Adsorption of Trimesic Acid on ITO Nanoparticles 105

5.1 Introduction 105

5.2 Experimental and Computational Details 106

5.2.1 Synthesis of ITO Nanoparticles.....106

5.2.2 Surface Modification by Trimesic Acid.....106

5.2.3 Characterization.....106

5.2.4 Electrochemical Measurement 107

5.2.5 Computational Details.....108

5.3 Results and Discussion.....109

5.3.1 Characterization of ITO Nanoparticles 109

5.3.2 Adsorption of Trimesic Acid on ITO Nanoparticles.....110

Raman Spectroscopy.....110

Diffuse Reflectance Infrared Fourier Transform Spectroscopy.....113

Transmission Fourier Transform Infrared Spectroscopy.....115

X-ray Photoelectron Spectroscopy 116

5.3.3 Adsorption of TMA on ITO (111) Surface 119

5.3.4 Cyclic Voltammetry 127

5.4 Conclusion.....128

References 129

Chapter 6 Summary and Future Work 132

6.1 Summary 132

6.2 Limitations and Future Work 134

Appendix.....136

SUMMARY

Transparent conducting films are of great significance in various electronic devices. Solution deposition of transparent conducting oxide thin films with improved qualities and properties is highly desired compared to the current technology. We have developed a solution process to deposit transparent and conductive indium-tin-oxide (ITO) thin films. The qualities and critical properties were comparable with the benchmark obtained by the dominant sputtering technique, including low sheet resistance (R_s~30 Ω/sq), high transparency (T~92%) and smooth surface (rms~1.1 nm). The results suggested that the control over hydrolysis process was crucial for the enhanced film qualities and properties.

ITO films are widely used in various electronics especially in displays where extremely thin (e.g. < 100 nm) but highly conductive and transparent ITO films are required. Tin is the most commonly used dopant for indium oxide to offer ITO film a better conductivity and transparency. However, other group IVA elements (e.g. Si and Ge) are also possibly effective dopants. Investigations on their electronic structures will be beneficial for the understanding about the origin. We have used the density functional theory to study the geometrical and electronic structures of In_2O_3 host doped with group IVA and fifth-period elements. Electronic structures revealed that Si, Ge and Sn were effective dopants which provided the host with a large conduction band width (>2 eV), a low effective mass (m^*~0.2 m_0) and a high electron group velocity (>8.3×10^5 m/s) across the Fermi level. The substitutional defect

of Sn displayed a relatively shallow donor level and low transition level under both indium-rich and oxygen-rich conditions.

Graphene analogs have shown very interesting electronic and optical properties. We employed the density functional theory to design a novel transparent conductor by using a graphene analog—hexagonal gallium sulfide. The doping was achieved by hydrogenation of sulfur atoms. After doping, the two-dimensional GaS showed a metallic band feature and Burstein-Moss shift of the optical band gap, implying an increased electrical conductivity and visible transmittance. A splitting of the valence band maximum was also observed. The semi-classic calculation of carrier transport properties indicated that the doped single layer GaS showed a low resistivity on the order of 10^{-4} Ω·cm when doping concentration achieved 8.98×10^{14} cm^{-2}. The resistivity was comparable with the typical value of ITO films prepared by physical vapor deposition techniques.

ITO films have wide application in organic electronics, for example, organic light-emitting diodes and organic photovoltaics. The application requires silanes, phosphonic acids and carboxylic acids, etc. to modify ITO films to improve the wettability of commonly used hole transporting layers (HTL) on ITO films and the charge transport through ITO/HTL interfaces. We have used trimesic acid to modify ITO nanoparticles to understand the adsorption behavior of the carboxylic acid on ITO surfaces. Various spectroscopies, including Raman spectroscopy and diffuse reflectance infrared Fourier transform spectroscopy, have been utilized to investigate the adsorption of trimesic acid on ITO nanoparticles. Density functional theory was also used to simulate the adsorption of acid molecules on the ITO (111)

surface. Both results revealed that the molecules were adsorbed in upstanding configurations by dissociation to form carboxylate.

LIST OF TABLES

2-1: The structural analysis of ITO films before and after annealing in H_2/Ar. 43

2-2: The properties of typical ITO films prepared by various deposition processes. 44

2-3: FTIR peak positions and corresponding assignments. 46

3-1: The relaxed geometrical parameters of pure and n-type doped In_2O_3 structures.....56

3-2: The electronic properties of pristine and n-type doped In_2O_3. 59

3-3: The Bader charges of the dopants and six nearest oxygen atoms.. 67

3-4: The formation enthalpy of host material and possible secondary phases. 72

4-1: The optimized geometrical parameters of different structures. 82

5-1: The Raman bands for solid and adsorbed TMA and the possible assignments.....112

5-2: The DRIFTS and FTIR absorption bands of TMA. 114

5-3: The bond lengths and dissociative chemisorption energies of the 24 possible adsorption configurations. 124

5-4: The Bader atomic charges in the 24 possible adsorption configurations. 125

LIST OF FIGURES

1-1: The single unit cell of face-centered cubic CdO crystal.....3

1-2: The crystal structures of wurtzite ZnO viewed along c-axis and a-axis.....4

1-3: The crystal structure of rutile SnO_2. 6

1-4: The conventional unit cell of body-centered cubic In_2O_3 and the local structures of the two different cationic positions. 7

1-5: Schematic band structures of undoped and doped semiconductor. 11

1-6: The electronic band structures of (a) pure bixbyite In_2O_3 and (b) 6.25 at% tin-doped In_2O_3. 14

1-7: The typical transmittance, reflection and absorption spectra of TCO films as a function of wavelength. 16

1-8: Schematic energy level diagrams of the major functional layers in OPV and OLED. 20

2-1: (a) XRD pattern of the ITO film (Sn%=10%); Dependence of the (b) XRD (222) peak positions, (c) lattice constants and (d) film resistivities versus dopant percentages. 37

2-2: Morphologies of ITO film (Sn=10%) after annealing in H_2/Ar: (a, b, and c) SEM images; (d) AFM image. 40

2-3: XPS spectra of ITO films after H_2 annealing: (a) survey scan; (b-f) core-level fine scans. 41

2-4: XRD pattern and AFM image of ITO film before annealing in H_2/Ar. ...42

2-5: UV-vis spectrum of ITO film (Sn=10%) after H_2 annealing. 44

2-6: FTIR spectra of the dried sol-gel samples prepared by dissolving $SnCl_4$ in (a) ethanol; (b) acetylacetone. 46

2-7: FTIR spectrum of the vacuum-dried sample and SEM image of ITO film prepared by conventional sol-gel process.....47
3-1: The binding energies vs. the volumes of pristine and n-doped In_2O_3. 55
3-2: The band structure and projected density of states of In_2O_3.. 58
3-3: The band structure and projected density of states of Si-doped In_2O_3. 60
3-4: The band structure and projected density of states of Ge-doped In_2O_3... 61
3-5: The band structure and projected density of states of Sn-doped In_2O_3.. ..61
3-6: The band structure and projected density of states of C-doped In_2O_3.....63
3-7: The band structure and projected density of states of Pb-doped In_2O_3. ...63
3-8: The band structure and projected density of states of Sb-doped In_2O_3.. ..64
3-9: The band structure and projected density of states of Te-doped In_2O_3.. ..64
3-10: The band structure and projected density of states of I-doped In_2O_3.. ...65
3-11: The calculated atomic orbital energies for the valence electrons of the dopant and host atoms. 66
3-12: The charge density differences for n-type doped In_2O_3.. 69
3-13: The formation energies of the substitutional defects at different conditions: (a) O-rich and (b) In-rich.. 73
3-14: The calculated transition levels for different substitutional dopants.....74
4-1: The optimized structure of bulk β-GaS unit cell viewed along a-axis and c-axis.....80
4-2: The optimized 2-D GaS structure..... 83
4-3: The optimized structure of H-doped (1 ×1 ×1) GaS supercell.. 84
4-4: The optimized structure of H-doped (2 ×2 ×1) GaS supercell.. 85
4-5: The relaxed structure of H-doped (3 ×3 ×1) GaS supercell.. 86
4-6: The optimized structure of H-doped (4 ×4 ×1) supercell.. 87

4-7: The total and partial density of states of bulk β-GaS.. 88

4-8: The total and partial DOS of the pure 2-D GaS at (a) wide energy region, (b) narrow region near E_F.. 90

4-9: (a) partial DOS, (b) total spin-polarized DOS of H-doped (1×1×1) GaS.. 91

4-10: The partial and total DOS of the different 2-D GaS supercells: (a) (2×2×1), (b) (3×3×1), and (c) (4×4×1).. 93

4-11: The band structure of bulk GaS.. 94

4-12: The band structure of pure 2-D GaS.....95

4-13: The band structures showing VBM of 2-D GaS from 1L to 6L.....96

4-14: The band structure of H-doped (1×1×1) GaS.. 97

4-15: The band structures of the H-doped (a) (2×2×1), (b) (3×3×1) and (c) (4×4×1) 2-D GaS.. 98

4-16: The transport properties of the 2-D GaS with (a) different doping concentrations and (b) different layers. 100

5-1: The XRD pattern of ITO nanoparticles. 109

5-2: (a-b) FESEM images, (c-d) TEM image and (d) SAED pattern of ITO nanoparticles. 110

5-3: The Raman spectra of (a) the bare ITO; (b) TMA-adsorbed ITO nanoparticles and (c) solid TMA.. 111

5-4: The DRIFT spectra of (a) the bare ITO; (b) TMA-adsorbed ITO nanoparticles and (c) solid TMA. 113

5-5: The FTIR spectra of (a) the bare ITO; (b) TMA-adsorbed ITO nanoparticles and (c) solid TMA. 115

5-6: The XPS spectra of ITO nanoparticles before (a, c, e) and after (b, d, f) the adsorption of TMA molecules. 117

5-7: The O1s and C1s core-level XPS spectra of ITO nanoparticles with (a, c) and without (b, d) the adsorption of TMA molecules. 118

5-8: The side view and top view of the relaxed ITO (111) surface slab. 120

5-9: The ITO (111) slab with the surface atoms labeled (left) and the optimized structure of trimesic acid (right).. 121

5-10: Perspective view of the six most stable structures of TMA adsorbed on ITO (111) surface. 122

5-11: The normalized cyclic voltammograms of different electrode materials towards 1 mM Fc/Fc^{+} in CH_3CN. 127

LIST OF PUBLICATIONS

1. Fabrication of Highly Transparent and Conductive Indium-Tin Oxide Thin Films with a High Figure of Merit via Solution Processing

   Chen Z. X., Li W. C., Li R., Zhang Y. F., Xu G. Q., Cheng H. S.

   Langmuir, **2013**, 29, 13836-13842.

2. Surface Modification of ITO Nanoparticles by Trimesic Acid: A Combined Experimental and DFT Study

   Chen Z. X., Zhang Q. F., Huang L., Li R., Li W. C., Xu G. Q., Cheng H. S.

   Journal of Physical Chemistry C, **2014**, 118, 21244-21249

3. DFT Study of a Novel Transparent Conductor: Two-dimensional GaS

   In preparation

4. First-Principles Understanding of the n-Type Doping in In_2O_3: Electronic Structures and Formation Energies

   Under Review

Chapter 1

Introduction

1.1 Transparent Conductors

Transparent conductors refer to the transparent and electrically conductive materials that are coated on a rigid or flexible substrate (e.g. glass, stainless steel, plastic, etc.). They are essentially used in various state-of-the-art opto-electronic devices, including flat-panel displays, light-emitting diodes and touch screens, where they are required to conduct the electricity and simultaneously allow the light passing into or out of the devices.[1-3]

Up to date, considerable transparent conducting materials have been developed, including n-typed doped oxides, metal nanowires, graphene and carbon nanotubes, etc. According to the compositions, they can be classified into two categories, transparent conducting oxides (TCOs) and non-oxides. Both will be reviewed in details in the next two sections.

1.1.1 Transparent Conducting Oxides

p-type TCOs suffer from poor conductivities due to the heavy hole effective mass which is generally larger than $1.5m_0$ (m_0: electron rest mass). The development of p-type TCOs is so far unsuccessful. Therefore, TCOs mainly refer to n-type doped metal oxides developed by introduction of higher-valence cations or lower-valence anions (mainly fluorine) into the metal-oxide hosts. The free carriers are generally created by the ionizable intrinsic defects (e.g., oxygen vacancies and interstitial cations) and/or the extrinsic dopants (e.g., higher-valence cations). The high visible

transmittances are resulted from the large band gaps of metal-oxide hosts (generally E_g>3 eV).[1]

The first TCO was reported by Baderker more than a century ago. The Cd thin film that was thermally oxidized in air after deposition, became visibly transparent while maintaining a good electrical conductivity.[2, 4] Since then, great attentions have been paid to develop different TCO materials. Varieties of TCOs have been successfully prepared, including F-doped SnO_2 (FTO), Sb-doped SnO_2 (ATO), Al-doped ZnO (AZO) and the most commonly used Sn-doped In_2O_3 (ITO). Based on their different host materials, conventional TCOs can be divided into four types: CdO-based, ZnO-based, SnO_2-based and In_2O_3-based TCOs.

1.1.1a: CdO-based TCOs

As shown in Figure 1-1, cadmium oxide has a rock salt (face-centered cubic, space group: $Fm\bar{3}m$) crystal structure with each unit cell containing four formula units.[5] It was reported as an intrinsic n-type semiconductor with a direct band gap of only 2.28 eV.[6] The carriers probably came from intrinsic oxygen vacancies, interstitial cadmium as well as interstitial hydrogen atoms. As a result, intrinsic carrier concentrations could be as high as 12×10^{20} cm^{-3}.[6-8] The greatly increased electron carriers occupy the conduction band minimum, which could significantly enhance the optical band gap of CdO by more than 0.6 eV (known as Burstein-Moss shift, see Section **1.2.2**). As a result, CdO films become optically transparent. The epitaxial CdO films grown on MgO (100) substrate by metal-organic chemical vapor deposition (MOCVD) have shown the electrical conductivity and carrier mobility as high

as 1.1×10^4 S/cm and 307 $cm^2/(V\ s)$, respectively.[7] The mobility is even twenty times that of commercial ITO films.

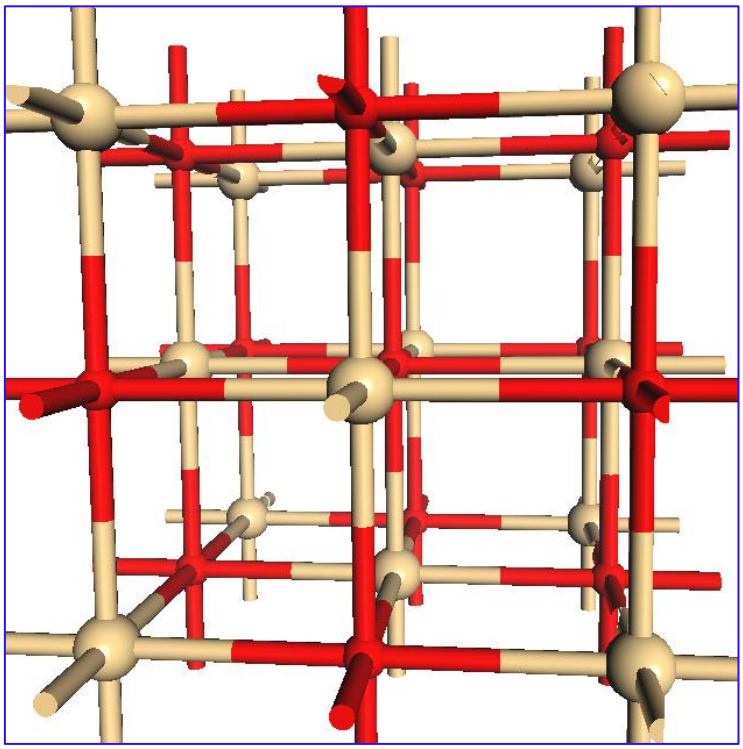

Figure 1-1: The single unit cell of face-centered cubic CdO crystal. (Small balls: O; big balls: Cd)

The n-type doping of CdO can be readily achieved by the substitutional replacement of Cd with extrinsic impurities, including tin, indium, yttrium and scandium.[9-11] The epitaxial Y-doped CdO thin films with even quite low doping levels (1.2~1.3 atom%) could have a significantly high conductivity (1.78×10^4 S/cm) and transparency (>80% in visible range).[11] An exceptionally high conductivity (4.2×10^4 S/cm) and carrier mobility (609 $cm^2/(V\ s)$) of Sn-doped CdO (CTO) thin films have been reported by Yan etc.[10] The CTO thin films were prepared on the MgO (111) substrate by pulse laser deposition (PLD) with the doping level of 2.5%. The high conductivity was attributed to the large carrier concentration (4.74×10^{20} cm^{-3}) and especially to the extremely high Hall mobility. The polycrystalline CTO films

fabricated on glass have shown an electrical conductivity (1460 S/cm) comparable to the benchmark of commercial TCOs. Although the intrinsic and extrinsically doped CdO thin films have exhibited the properties of a good transparent conductor, it is less desirable due to the high toxicity of cadmium.

1.1.1b: ZnO-based TCOs

ZnO with a large direct band (>3 eV) has attracted great attentions as a transparent conducting material.[12-13] It has three different structures: high pressure rock-salt phase, cubic zincblende phase and the most stable hexagonal wurtzite phase. The structure of wurtzite ZnO (hexagonal, space group: $P6_3mc$) is shown in Figure 1-2. It has two formula units in each unit cell with both Zn and O atoms in the tetrahedral coordination.

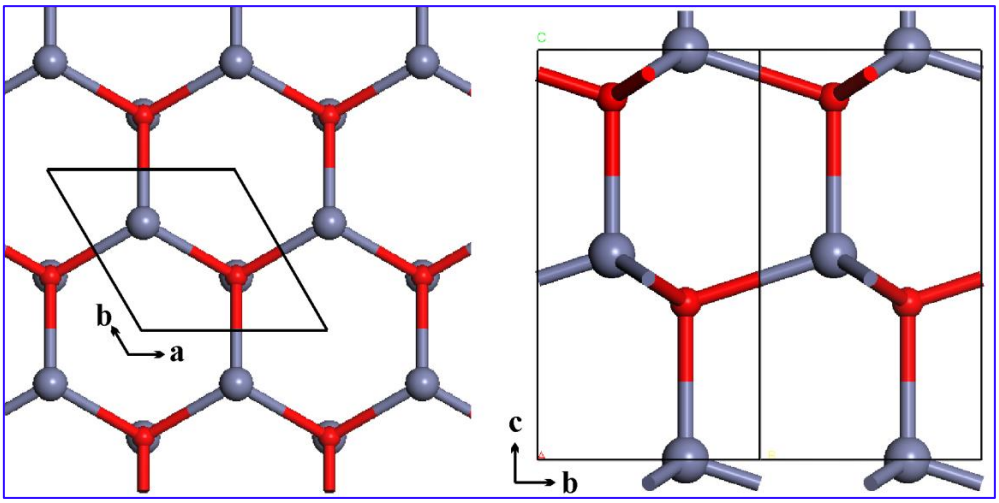

Figure 1-2: The crystal structures of wurtzite ZnO viewed along c-axis (left) and a-axis (right). (Small balls: O; big balls: Zn. Solid line shows a single unit cell.)

ZnO is an intrinsic n-type semiconductor, due to the oxygen vacancies and/or the interstitial zinc natively created during film deposition procedure, as well as hydrogen impurity incorporated during the post annealing in H_2.[14-16] The interstitial Zn and H are extremely shallow donors in ZnO lattice, since the transition levels are 30 meV below the conduction band minimum (CBM)

for interstitial Zn[14] and 0.34 eV above CBM for interstitial hydrogen. Compared with interstitial Zn and H, oxygen vacancies are rather deeper donors (0.5 eV below CBM).[17]

Although various shallow or deep donors are possibly available in intrinsic ZnO films, the doping of extrinsic impurities is still required to effectively improve carrier concentrations. Various dopants have been used to develop n-type doped ZnO transparent conductive thin films, including Si, In, Ge, Y and the widely used Ga and Al.[1-2, 18-22] Extremely high conductivities (Resistivity: $\rho<10^{-4}$ Ω·cm) of Al-doped (AZO) and Ga-doped ZnO (GZO) thin films have been reported by different groups, while average transmittance reached more than 88% in the visible range.[23-24] In addition to the large band gap, ZnO has several additional superiorities compared with other TCO materials, such as large abundance, low cost and low toxicity, etc. Therefore it has been extensively studied as the most promising substituent for Sn-doped In_2O_3 thin films which are dominantly used in current liquid-crystal displays.

1.1.1c: SnO_2-based TCOs

SnO_2 has been considered as another particularly important host material for transparent conducting oxides. Rutile SnO_2 (tetragonal, space group: $P4_2/mnm$) shows a large band gap of more than 3 eV,[25-26] which therefore offers SnO_2 thin films high visible transparency (generally T>80%). Each rutile SnO_2 unit cell contains two formula units with all the oxygen atoms trigonally coordinated while each tin atom octahedrally coordinated (Figure 1-3).

Various native defects, including oxygen vacancies, interstitial tin and hydrogen impurities, were believed to account for the n-type behavior of

intrinsic SnO_2 thin films.[27-29] Although carrier mobility ranged from 10 to 200 $cm^2/(V\ s)$, the carrier concentration of intrinsic SnO_2 was still too low (~10^{17} cm^{-3}) to be a good transparent conductor.[30] The conductivities of SnO_2 thin films can be significantly improved to be around 10^4 S/cm by the n-type doping with tantalum, niobium, antimony and fluorine etc.[1, 20, 26, 31-32]

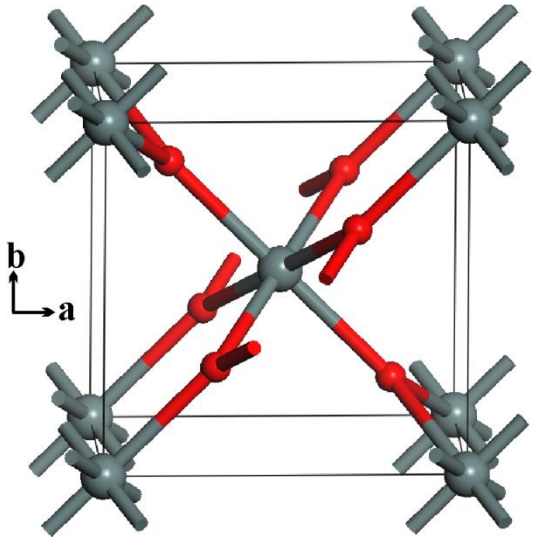

Figure 1-3: The crystal structure of rutile SnO_2. (Small balls: O; big balls: Sn)

Except tin-doped indium oxide (ITO), fluorine-doped tin dioxide (FTO) is the most widely used TCO material. It is more advantageous in terms of low cost, high thermal stability, high work-function as well as high chemical resistance to an acidic environment.[1-2, 20] Therefore, FTO is the dominant TCO material used in thin-film solar cells, especially in dye-sensitized solar cells (DSSC).

1.1.1d: In_2O_3-based TCOs

Indium oxide is reported to exist in three different crystal structures: two with body-centered cubic phases (space groups: $I2_13$ and $Ia\bar{3}$) and one in high-pressure rhombohedral phase (space group: $R\bar{3}c$).[33-35] Although the

rhombohedral structure of In_2O_3 is the so-called high-pressure phase, it was still capable of being deposited epitaxially under a normal pressure.[34] The most common In_2O_3-based TCO films show the body-centered cubic (bcc) bixbyite structure with space group $Ia\bar{3}$, since it is energetically more favorable than the other two rarely reported phases.[33]

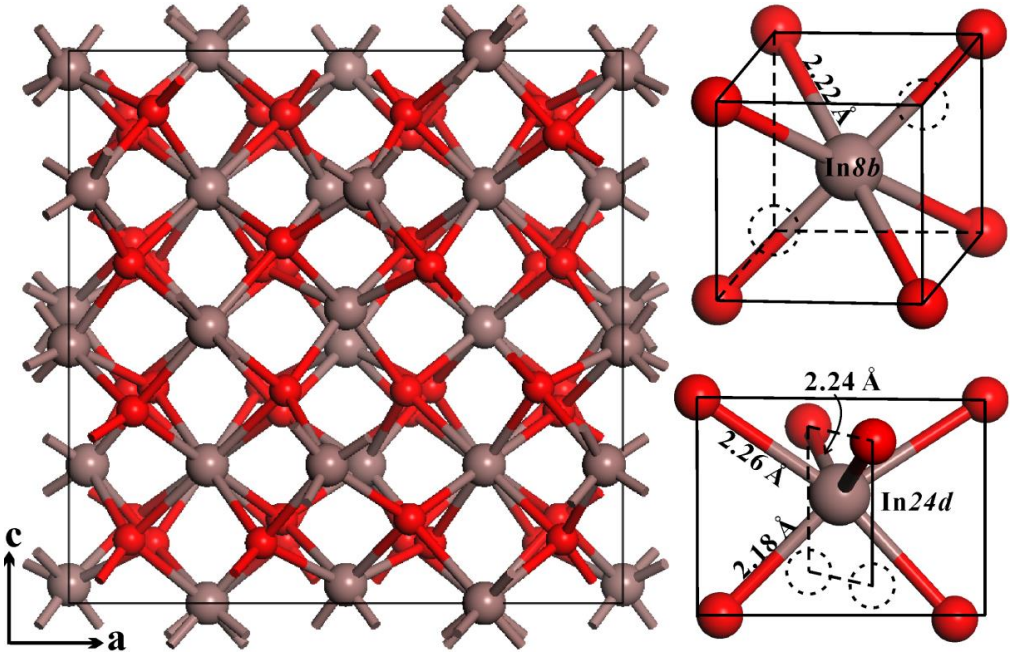

Figure 1-4: The conventional unit cell of body-centered cubic In_2O_3 (left) and the local structures of the two different cationic positions (right). (Small balls: O; big balls: In)

The crystal structure of bcc bixbyite In_2O_3 is presented in Figure 1-4. Each conventional unit cell contains 16 formula units with the lattice constant close to 10.12 Å.[36] All oxygen atoms are in equivalent positions, while the cationic atoms occupy two different sites. Eight indium atoms sit at the *8b* site which can be viewed as the center of a trigonally distorted octahedron due to the two missing oxygen atoms (Figure 1-4). The bond lengths are equally 2.22 Å for the six O-In_{8b} bonds. The remaining 24 cations occupy the *24d* position which

is the center of a tetragonally distorted octahedron. The lengths of the three pairs of O-In_{24d} bonds range from 2.18 to 2.26 Å.

The fundamental band gap of In_2O_3 was originally quoted as 3.75 eV.[37] Afterwards, it was experimentally determined to be much narrower (<2.9 eV).[38-39] The discrepancy of more than 0.8 eV was explained by the optical transition started at 0.8 eV below the valence band maximum, since the direct transition from VBM to CBM at Γ was formally forbidden due to the symmetry of bixbyite In_2O_3. The strong optical absorption only occurred from 0.81 eV below the VBM, where the transition matrix elements became large.[38]

Similar to other TCO host materials, intrinsic In_2O_3 thin films also display a n-type electrical behavior.[40] Oxygen vacancies, interstitial cations and hydrogen impurities existing in the intrinsic indium oxide films were responsible for the n-type conductivity.[17, 41-43] The carrier density of intrinsic In_2O_3 thin films generally varies from 7×10^{16} to 7.5×10^{18} cm^{-3}, although some exceptionally high concentrations were also reported.[40, 44-45]

The carrier concentrations can be significantly enhanced to 10^{21}~10^{22} cm^{-3} by doping In_2O_3 with various n-type dopants, including Sn, Ge, Mo, Nb and Ti.[1-2, 19-20, 46-47] Among them, tin-doped indium oxide (ITO) thin films give the lowest resistivity at the level of 10^{-4} Ω·cm when the thicknesses of TCO layers are within 100 nm. Furthermore, over other TCO materials, ITO takes advantages of better etchability, lower deposition temperature and higher deposition rate. Therefore, ITO is the most widely used TCO in liquid-crystal displays where a highly conductive and sufficiently thin TCO layer is required.[19-20]

1.1.1e: Other TCOs

The TCOs reviewed above are all binary according to the compositions of host materials. The versatility of material compositions provides additional opportunity for scientists to develop and study new TCO candidate materials. There have been considerable multi-component TCO materials developed up to date. The ternary TCOs, including intrinsic or doped $GaInO_3$, $ZnSnO_3$, $SrSnO_3$ and $BaSnO_3$ have shown potentially interesting properties as transparent conducting films (e.g. $\rho \sim 10^{-3}\ \Omega \cdot cm$, T>85%).[48-53]

One widely studied quaternary TCO is indium-gallium-zinc-oxide (IGZO).[54-55] A peculiar feature of IGZO is the layered structure formed by the repeating insulating layer (InO_2^-) and conducting layer ($Ga(ZnO)_n^+$) stacked along z-axis alternately. The unique feature was believed to facilitate the spatial separation of carriers in each layer and thus reduce charge carrier scattering,[43, 54] which can enhance the field-effect mobility (~80 $cm^2/(V\ s)$). Therefore it is a good n-type channel material for transparent thin-film transistor (TFT).[54]

1.1.2 Non-oxides

Besides the different metal-oxide based TCO materials reviewed in Section **1.1.1**, numerous non-oxide based materials have been developed as transparent conducting materials as well, including metal nanowires, conducting polymers, carbon nanotubes and graphene.[56-64]

Graphene and Carbon Nanotubes

Tremendous efforts have been made to develop carbon nanotubes (CNT) and graphene as transparent conducting films, due to their peculiar electronic properties. The electronic structure of atomically thin carbon layers is featured

by the Dirac cone shape band structure. The electrons are massless due to the linear dispersion relation at the Dirac point (K point in the first Brillouin zone). Therefore, the electron mobility could be extremely high (e.g. 10^4 $cm^2/(V\ s)$),[65-66] which is highly desirable for transparent conductors and other electronic devices.

Considerable works have been reported about the fabrication of transparent conducting films by using CNT and graphene.[62-63, 67] Highly conductive (Sheet resistance~100 Ω) and transparent (Transmittance~90%) CNT or graphene films could be facilely fabricated.[62-63, 68] In addition, the high bendability makes it very promising for their applications in flexible electronics, such as touch screens and curved OLED displays, especially when large-scale (~600 $inch^2$) deposition and roll-to-roll processing of graphene became possible.[69]

1.2 Properties of Transparent Conducting Oxides

Transparency and conductivity are the two major properties of transparent conductors. Due to the complexity of material compositions, here we only focus on the properties of transparent conducting oxide thin films.

1.2.1 Electrical Conductivity

The electrical conductivity (σ, in unit of S/cm) of TCO films can be expressed as:

$$\sigma = ne\mu \tag{1-1}$$

where n (cm^{-3}) and μ ($cm^2/(V\ s)$) refer to the carrier concentration and carrier mobility respectively. e is the fundamental charge of an electron (1.602×10^{-19} C). The typical conductivity of TCO films is around few thousands S/cm, while in contrast the value is about 10^5 S/cm for metal thin films.[2, 20]

More conventionally, resistivity (ρ, in unit of Ω·cm. ρ=1/σ) and sheet resistance (R_s: Ω/sq) are used to characterize the electrical conductivity of TCO films instead of conductivity. The resistivity of TCO films is typically on the order of 10^{-4} Ω·cm. Given the small thickness of TCO layer (t<200 nm in ITO case), the benchmark sheet resistance (R_s=ρ/t) is within 100 Ω/sq.

1.2.1a: Carrier Concentration—n

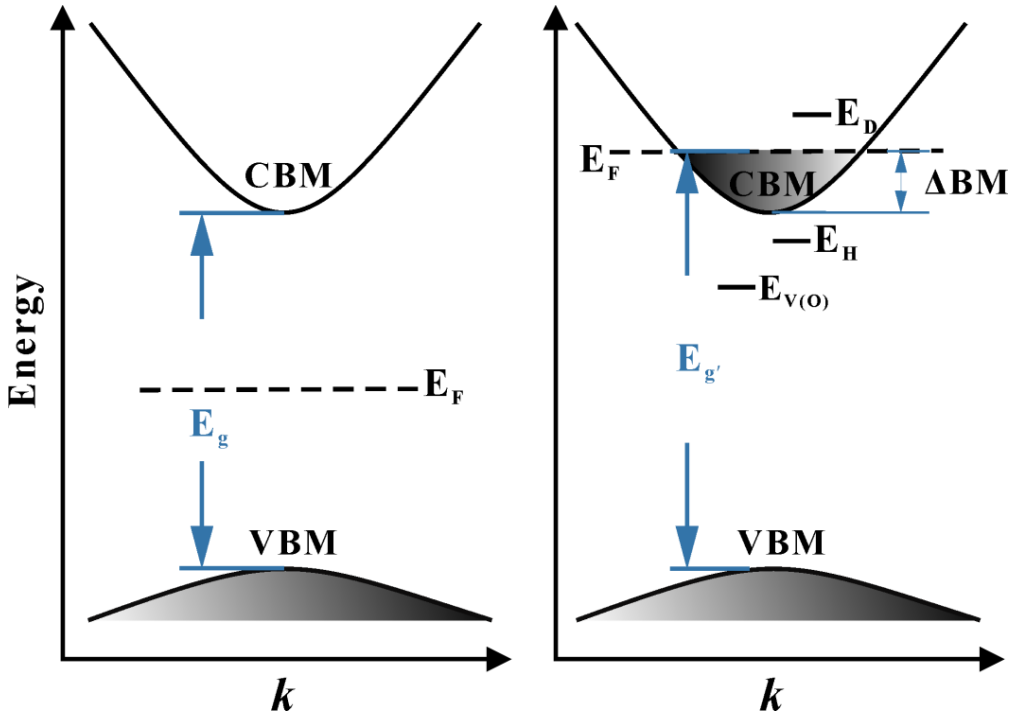

Figure 1-5: Schematic band structures of undoped (left) and doped (right) semiconductor. E_D, E_H and $E_{V(o)}$ denote the energy levels of donor, hydrogen impurity and oxygen vacancy respectively.

According to the band theory, the valence bands of a perfect semiconductor at T=0 K, are completely occupied while the conduction bands are entirely empty (Figure 1-5, left). Therefore, no free carriers are available for the electrical conduction. However, due to the thermal energy above 0 K and/or other perturbations, the carriers can be generated intrinsically from the optically and/or thermally excited defects (e.g. oxygen vacancies, interstitial cations).[14, 16-17, 29, 41]

The oxygen vacancy can be easily formed during film deposition process, which are thermally ionized to generate two electrons per vacancy:[2, 42]

$$O_O \rightleftharpoons V_O^{2+} + \tfrac{1}{2}O_2(g) + 2e \quad (1\text{-}2)$$

where V_O^{2+} denotes the oxygen vacancy. The equilibrium constant of the reaction is expressed as $K = [V_O^{2+}][e]^2 p_{O_2}^{1/2}$, where the brackets refer to the concentrations of oxygen vacancies and free carriers and p_{O_2} is the partial pressure of oxygen. Considering that $[V_O^{2+}] = \frac{1}{2}[e]$, the free carrier concentration resulted from oxygen vacancies is obtained as:

$$\mathrm{n} = [e] = (2K)^{1/3} / p_{O_2}^{1/6} \quad (1\text{-}3)$$

Equation 1-3 implies that the carrier concentration generated from oxygen vacancies is inversely proportional to the oxygen partial pressure. Therefore, a post-annealing in an inert or reducing atmosphere (e.g. Ar or forming gas of H_2/Ar) is helpful to enhance the electrical conductivity of TCO films, which has been commonly used especially for the solution-processed TCO films.[70]

From defect physics point of view, the intrinsic defects in TCOs have the energy levels around the conduction band minimum (Figure 1-5, right). Oxygen vacancies are deep donors with relatively high ionization energies, for example, 0.6 eV in ZnO[16] and 1.8 eV in SnO_2.[28] In contrast, the interstitial metal atoms have extremely shallow donor levels (e.g. CBM-30 meV for interstitial Zn[14]) or even spontaneous ionizations because of the donor levels located above CBM (e.g. CBM+203 meV for interstitial Sn[29]). Most intrinsic carrier densities for commonly used TCO films generally range from 10^{16} to 10^{18} cm^{-3}, much lower than that of metals (10^{22}~10^{23} cm^{-3}).

By the introduction of extrinsic dopants, the carrier concentrations of intrinsic TCO films can be significantly increased to 10^{21}~10^{22} cm^{-3}. These donors, including intentionally and substitutionally doped higher-valence cations and unintentionally doped hydrogen impurity, have shown the energy levels below and/or even above CBM. Therefore, under thermal activation, these donors are facilely ionized to donate the electrons to fill up the conduction band minimum (Figure 1-5).

1.2.1b: Carrier Mobility—μ

The carrier mobility is an intrinsic property of TCO materials, indicating the ease of carriers conducting current within TCO films. It is expressed as:

$$\mu = \frac{e\tau}{m^*} \tag{1-4}$$

The e, τ and m* refer to the elementary charge, average scattering time and effective mass of carriers, respectively.

Conventional TCO materials have the typical carrier effective mass less than 0.4 m_0 (m_0: electron rest mass).[44, 71] It is intrinsically related to the electronic band structures which show the feature of a free-electron-like conduction band, as indicated by the parabolic shape of the conduction band (Figure 1-6a). The conduction band minimum is predominantly contributed by the In-*5s* states which are highly delocalized.[43, 72] Therefore, the large band dispersion results in a large curvature at the conduction band minimum, which corresponds to a small effective mass (*m** is inversely proportional to the curvature at CBM).[73] The *5s* states of Sn dopant (6.25 atom%) were strongly hybridized with the O-*2p* states. Therefore, the parabolic shape feature of conduction band is well retained (Figure 1-6b), implying the small effective mass after doping.[43, 74]

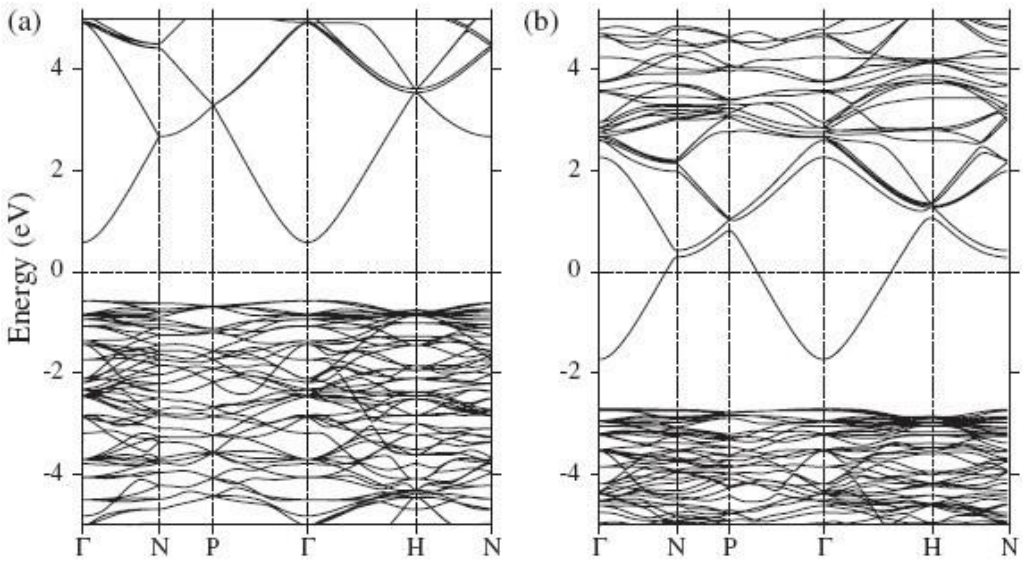

Figure 1-6: The electronic band structures of (a) pure bixbyite In_2O_3 and (b) 6.25 at% tin-doped In_2O_3. (Reproduced with permission from reference [74])

Since the effective mass is an intrinsic property of the host material, Equation 1-4 suggests that the carrier mobility of TCO films is simply related to the average time of each carrier scattering. The scattering of carriers can be from various sources, including neutral defects, ionized defects, grain boundaries, and phonon scatterings, etc.[2, 19] According to Matthiessen's rule, the overall carrier mobility is related to each scattering source by:[2]

$$\frac{1}{\mu_{total}} = \frac{1}{\mu_{impurity}} + \frac{1}{\mu_{defect}} + \frac{1}{\mu_{grain-boundary}} + \ldots \qquad (1\text{-}5)$$

As can be seen, all the possible sources of scattering contribute to the total carrier mobility of TCO films. Since the scattering mechanisms are complicated, quantitatively differentiating each component is currently impossible. However, the dominant scattering mechanism can be deduced from the relation between Hall mobility and temperature. For example, the mobility depending on temperature by $\mu \propto T^{3/2}$ indicates an ionized impurity scattering,[75] while $\ln \mu \propto -1/T$ and $\mu \propto 1/T$ imply that the carrier mobility

is limited by grain boundaries and phonons, respectively.[76-77]

For degenerate TCOs, the most important scattering comes from the ionized impurities. Increasing the doping concentrations can not only enhance the carrier concentration, but reduce the carrier mobility. To obtain the highest conductivity, a trade-off between these two parameters has to be made.[78-79] In general, polycrystalline TCO films have the carrier mobility less than 100 $cm^2/(V\ s)$, except in some particular cases (e.g. epitaxial CdO film and single-layer graphene).[7, 10, 66]

1.2.2 Optical Property

1.2.2a: Band Gap—E_g

The optical property is another important aspect to be considered for TCOs. As shown in Figure 1-5, the valence band and conduction band of crystalline semiconductors are separated by the band gap with an energy of E_g. Due to the ionization of intrinsic or extrinsic dopants, the conduction band minimum is filled with free carriers which shift the Fermi level close to or even into the conduction band. Therefore, the energy required for the intra-band transition is increased ($E_{g'}=E_g+\Delta BM$), which indicates a blue-shift of the onset absorption wavelength. This phenomenon is well-known as the Burstein-Moss shift. It is significantly helpful for the low band-gap TCO material which is originally not transparent. For example, the Burstein-Moss shift increases the optical gap of CdO from 2.28 eV to 3.27 eV upon being doped with Y.[11]

A typical transmission spectrum of TCO film is shown in Figure 1-7. TCO films generally have band gaps larger than 3 eV. The strong absorption occurs when the wavelength blue-shifts into the ultraviolet region. The transmittance of conventional TCO films can be as high as more than 92% in the visible

range. The minor loss of transparency is resulted from the reflection, refraction as well as scattering involved at the three interfaces of TCO films (air/glass, glass/TCO layer and TCO layer/air).

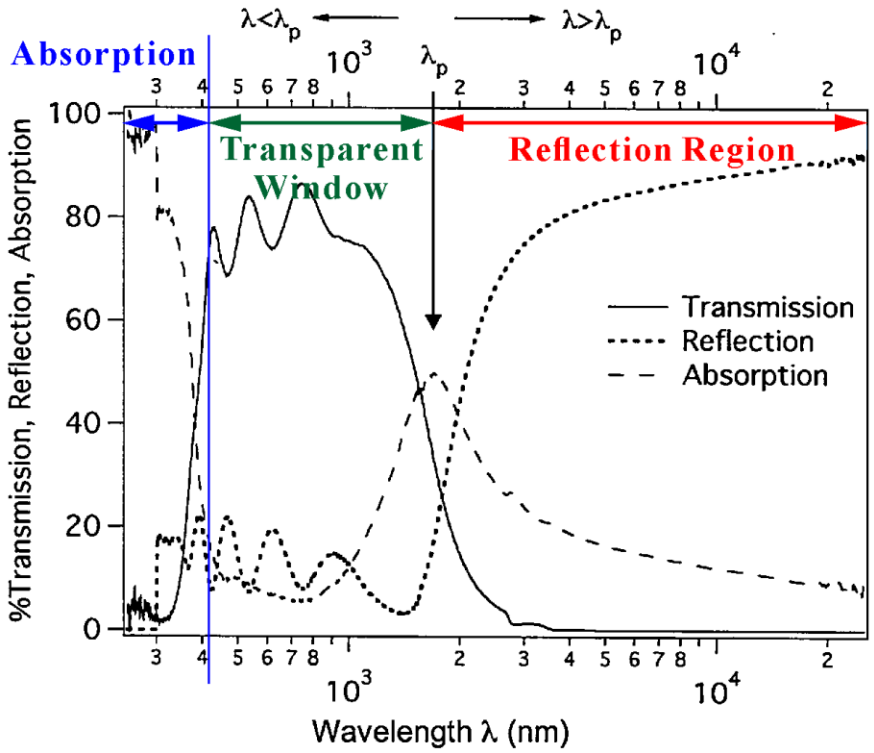

Figure 1-7: The typical transmittance, reflection and absorption spectra of TCO films as a function of wavelength. (Reproduced with permission from reference [2])

1.2.2b: Plasma Frequency—λ_p

As shown in Figure 1-7, a strong absorption occurs at the near-infrared region (NIR) with the maximum absorption at the wavelength of λ_p, known as the plasma wavelength. This is due to the oscillation of free carriers. According to the classical Drude transport model, the plasma wavelength (λ_p) is related to the carrier concentration (n) by:[2, 80]

$$\lambda_p \propto \frac{1}{\sqrt{n}} \tag{1-6}$$

The wave with $\lambda<\lambda_p$ can propagate through TCO layer, whereas the wave with $\lambda>\lambda_p$ is exponentially damped and cannot propagate.[81] Metal has much higher

carrier density and thus has the plasma wavelength in the ultraviolet region. TCOs have a typical plasma wavelength at the NIR region (e.g. λ_p~2.5 μm). Therefore, TCO films show a high visible transparency but a high reflection in IR region.

1.2.3 Figure of Merit—FOM

Electronic devices, especially high-end applications (e.g. displays), require TCO films to be as conductive (low sheet resistance) and transparent as possible. However, as reviewed in the previous section, the visible transmittance is reduced by a higher carrier concentration. Therefore, another trade-off exists in TCOs, between the conductivity and transmittance.

To quantitatively evaluate the performance of a transparent conductive film with different thickness, conductivity and transparency, Haccke proposed a revised figure of merit (FOM) defined by:[82]

$$\Phi_H = T^{10} / R_s \tag{1-7}$$

A higher FOM indicates a better performance of TCO films. However, the trade-off between the sheet resistance and transparency limits the FOM on the order of $10^{-2}\ \Omega^{-1}$ for the most polycrystalline TCO film.[83]

Besides the properties reviewed above, there are many other criteria to be considered depending on specific applications of TCOs, for example, thermal stability, chemical stability, resistance to hydrogen plasma, haze, etchability and deposition temperature, etc.[20] These properties are less important and will not be reviewed in this Chapter.

1.3 Depositions of Transparent Conducting Films

Up to date, there has been various deposition techniques developed to fabricate transparent conducting films, including spray pyrolysis, chemical

vapor deposition, direct-current sputtering, magnetron sputtering, atomic layer deposition and pulse laser deposition. According to the basic process involved in deposition procedure, they can be classified into two categories: vapor deposition and solution deposition.

1.3.1 Vapor Deposition

Vapor deposition techniques include chemical vapor deposition, sputtering, atomic layer deposition, pulse laser deposition, thermal evaporation and their various combinations. Their working principles differ significantly from each other. In general, they employ physical manners, for example, thermal heating, laser heating and energetic particles, to generate the vapor of TCO source materials which deposit onto a substrate to form TCO layers. Vapor deposition is delicate due to their good capabilities of controlling the film density, roughness, and crystalline microstructure, etc. Therefore, TCO films with benchmark properties ($\rho \sim 10^{-4}$ $\Omega \cdot$cm; T>85%) can be easily obtained by vapor depositions.[84]

1.3.2 Solution Deposition

Solution depositions (e.g. spray pyrolysis) of TCO films had been invented earlier than vapor deposition techniques (e.g. sputtering). These techniques include spin coating, spray pyrolysis, dip coating, ink-jet printing etc. Recently, it has attracted great attentions due to the potential advantages compared with vapor deposition, such as a low cost, a simple equipment and the non-vacuum processing condition.[2] The solution process mainly involves three steps: (1) preparing TCO solutions; (2) coating wet films with a dispersion/solution; (3) annealing of the wet film to eliminate organics and improve the film quality. According to the precursors used, solution deposition mainly includes two

routes: one using nanostructures dispersion (e.g. CNT and Ag nanowire dispersions) and the other employing the precursor solution (sol-gel solution).

The first route can leave the crystallization process at synthetic step. Therefore, a high-temperature post annealing of the nanostructured films might be avoided.[85] This method is widely used for the solution deposition of CNT and metal-nanowire (e.g. Au, Ag and Cu nanowires) films. However, it is not applicable to TCO nanostructures, since high solid loading (e.g. ITO and AZO nanoparticles) require large-molecule stabilizers (e.g. oleic acid[86] and trioctylamine[21]) to prevent the agglomeration of these nanostructures. Therefore, a high-temperature post annealing is indispensable to remove the organics and improve the film conductivity.[21, 86] Due to the porous structure among TCO nanoparticles and possible organic residual after thermal annealing, the film resistivities (ρ: 10^{-2}~10^{-3} Ω·cm, R_s>300 Ω/sq) remain relatively high.

Compared to the former, the other route using sol-gel solution is capable of delivering TCO films with denser structures and better qualities. Thus the benchmark resistivity (ρ~10^{-4} Ω·cm) could be facilely achieved by sol-gel process. For example, low resistive ITO films (2.1~6 ×10^{-4} Ω·cm) could be obtained by a dip coating method with various ITO sol-gel solutions.[87-92] AZO films with relatively higher resistivity (7~10 ×10^{-4} Ω·cm) can be prepared by similar dip-coating deposition with an alcoholic solution of zinc acetate and aluminum chloride.[93] The lower porosity (e.g. 28% vs. 52%[92]) was responsible for the lower resistivity compared with the films prepared by TCO nanoparticles.[94] Furthermore, this route takes over several advantages, including simple solution preparation, good control over the stoichiometry and

possible deposition of amorphous films.[2] Therefore, it is widely used in solution deposition of TCO thin films.

1.4 Application

Surface Modification of ITO films for Applications in OLED and OPV

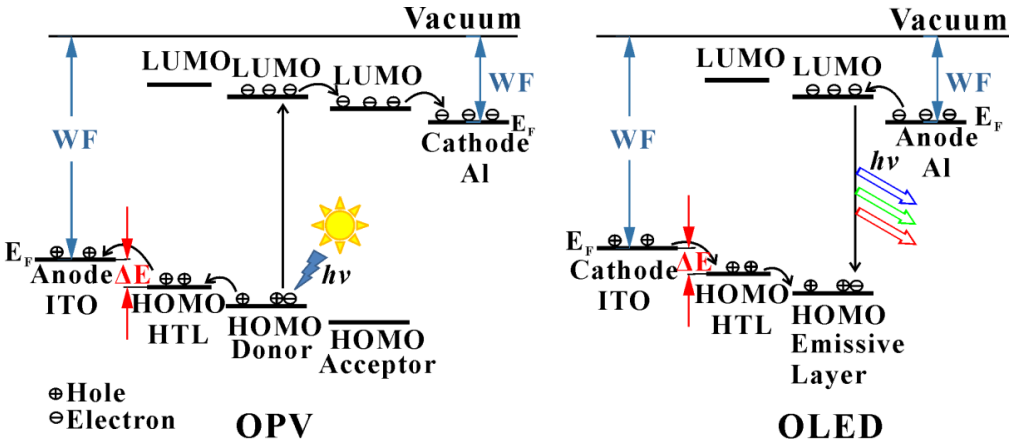

Figure 1-8: Schematic energy level diagrams of the major functional layers in OPV (left) and OLED (right). WF and ΔE refer to work function and energy barrier, respectively.

Transparent conducting films have wide applications in various opto-electronic devices, including flat-panel displays, touch screens, thin-film solar cells and light-emitting diode. Due to the better conductivity and higher work function (WF) compared with other TCOs, ITO films are more preferred in organic light emitting diodes (OLED) and organic photovoltaics (OPV). However, the work function of ITO films is still not high enough compared with the HOMO energy of commonly used hole transporting layers (e.g. 5.4 eV for NPB[95]). As a result, an energy barrier (ΔE) exists at the interface, which prevents the hole transfer, as illustrated in Figure 1-8. In addition, the poor wettability of hydrophobic hole transport materials on hydrophilic ITO surface deteriorates the device efficiency significantly. Therefore, a surface modification of ITO films and a fundamental understanding of the

physical/chemical process involved in the modification are very important for their applications in OLED and OPV.

Various small molecules have been utilized to modify ITO films, mainly including carboxylic acids, silanes and phosphonic acids.[96-97] The modifications can effectively alter the surface energies and tune the work functions of ITO films. As a result, the device efficiency could be significantly improved. In contrast to the diversity of silanes and phosphonic acids, the carboxylic acids used for the modification of ITO films are very limited, only including 3-thiophene acetic acid, ferrocene dicarboxylic acid and other ferrocene-based carboxylic acids.[98-100] Due to the complexity of polycrystalline ITO surfaces and carboxylic acid molecules, several adsorption models were tentatively proposed, including ester formation, chelation between carboxylic group and surface metal atoms and hydrogen bonding interactions.[97] It is interesting to modify ITO films with other carboxylic acids by tuning the surface chemistry of ITO films in a different way and further understand the interfacial bonding between the functional molecules and ITO films by investigating their fundamental adsorption behaviors on transparent conducting films.

1.5 Motivations and Objectives

1.5.1 Solution Deposition of ITO Transparent Conducting Film

As briefly reviewed in Section **1.3.2**, solution depositions of transparent conducting films are more advantageous than vapor depositions, in terms of, for example, simple instruments and non-vacuum processing conditions. However, the ITO film qualities and properties are inferior to those fabricated by vapor depositions, including high porosity, high resistivity and low

transparency. Therefore, the solution-processed ITO films generally exhibit a limited Haccke's figure of merit, due to their high sheet resistance and/or low transparency (Detailed review available in **Chapter 2**).

In **Chapter 2**, we aim to develop the solution process to deposit highly transparent and conductive ITO films. The critical film properties are comparable to the benchmark obtained by the most widely used vapor deposition technique—magnetron sputtering. The dependences of film structures and properties versus the compositions have been investigated. The properties of ITO films obtained by our solution process are significantly improved in comparison with these produced by other solution processes. The mechanism of the improvement is also discussed.

1.5.2 Theoretical Investigation of n-type Doped In_2O_3 Transparent Conductors

Among TCO films, the most conductive TCO is achieved by Sn-doped indium oxide. Therefore, ITO films are exclusively preferred in high-end applications, such as flat-panel display, where extremely thin film with low sheet resistance is required. The electronic structures have indicated that the Sn-*5s* states were strongly hybridized with O-*2p* after In_2O_3 host was doped with Sn. Thus, the conduction band features were well retained after the In_2O_3 host was doped with Sn, implying the effective doping of tin.[43]

In view of the effectiveness, we speculate the possibility of other n-type dopants, including the group IVA dopants (C, Si, Ge and Pb) as well as the fifth-period elements (Sb, Te and I). In **Chapter 3**, we employ the computational tools to investigate the geometrical and electronic structures of indium oxide doped with the above-mentioned elements. The band widths,

effective masses, electron group velocities and formation energies etc. are systematically compared for these n-doped indium oxide structures. A fundamental understanding of the properties versus dopant elements is also discussed.

1.5.3 Single Layer Gallium Sulfide Transparent Conductor

As briefly introduced in Section **1.1.2**, graphene has been successfully developed as transparent conducting films which have shown very promising properties, such as low sheet resistance (R_s~100 Ω) and high transparency (T~90%).[62-63, 68] In addition, the high bendability makes it very desirable in flexible electronics, such as touch screens and curved OLED displays.

Grapene analogs, such as BN, MoS_2, WSe_2, etc. have similar two-dimensional honeycomb structures to graphene. They display interestingly different electronic structures, from insulators to metals. In contrast to graphene, none of these analogs has been developed as a transparent conductor. Different from the semi-metal nature of graphene, hexagonal GaS is a typical semiconductor with a direct band gap of 3.05 eV and an indirect band gap of 2.5 eV.[101] **In Chapter 4**, density functional theory calculation is used to design transparent conductors using the graphene analog—hexagonal GaS. The geometries and electronic structures have been explored. The carrier transport properties have also been investigated.

1.5.4 Surface Modification of ITO Nanoparticles by Trimesic Acid

As reviewed in Section **1.4**, the application of ITO films in organic electronics requires the modification of ITO surface with various small functional molecules. The surface modifications of ITO films by phosphonic acids and silanes have been extensively studied both experimentally and

theoretically. In contrast, the modification by carboxylic acids is less studied and understood.

In **Chapter 5**, trimesic acid is used to modify ITO nanoparticles. Various spectroscopic techniques have been employed to learn the adsorption of the carboxylic acid molecules on ITO nanoparticles. In addition, the fundamental understanding of the adsorption has been investigated by the density functional theory simulation. The possible adsorption behaviors and potential application of the modified ITO nanoparticles have also been discussed.

References

1. Liu, H.; Avrutin, V.; Izyumskaya, N., et al., *Superlattice Microst.* **2010,** *48*, 458-484.
2. Pasquarelli, R. M.; Ginley, D. S.; O'Hayre, R., *Chem. Soc. Rev.* **2011,** *40*, 5406-5441.
3. Ellmer, K., *Nat. Photonics* **2012,** *6*, 808-816.
4. Badeker, K., *Ann. Phys. Berlin* **1907,** *22*, 749-766.
5. Cimino, A.; Marezio, M., *J. Phys. Chem. Solids* **1960,** *17*, 57-64.
6. Ueda, N.; Maeda, H.; Hosono, H., et al., *J. Appl. Phys.* **1998,** *84*, 6174-6177.
7. Metz, A. W.; Ireland, J. R.; Zheng, J.-G., et al., *J. Am. Chem. Soc.* **2004,** *126*, 8477-8492.
8. Speaks, D. T.; Mayer, M. A.; Yu, K. M., et al., *J. Appl. Phys.* **2010,** *107*, 113706.
9. Zhao, Z.; Morel, D. L.; Ferekides, C. S., *Thin Solid Films* **2002,** *413*, 203-211.

10. Yan, M.; Lane, M.; Kannewurf, C. R., et al., *Appl. Phys. Lett.* **2001,** *78*, 2342-2344.

11. Yang, Y.; Jin, S.; Medvedeva, J. E., et al., *J. Am. Chem. Soc.* **2005,** *127*, 8796-8804.

12. Klingshirn, C., *Phys. Status Solidi B* **1975,** *71*, 547-556.

13. Srikant, V.; Clarke, D. R., *J. Appl. Phys.* **1998,** *83*, 5447-5451.

14. Look, D. C.; Hemsky, J. W.; Sizelove, J. R., *Phys. Rev. Lett.* **1999,** *82*, 2552-2555.

15. Du, M.-H.; Biswas, K., *Phys. Rev. Lett.* **2011,** *106*, 115502.

16. Zhang, S.; Wei, S. H.; Zunger, A., *Phys. Rev. B* **2001,** *63*, 075205.

17. Ágoston, P.; Albe, K., *Phys. Rev. Lett.* **2009,** *103*, 245501.

18. Rashidi, N.; Kuznetsov, V. L.; Dilworth, J. R., et al., *J. Mater. Chem. C* **2013,** *1*, 6960-6969.

19. Minami, T., *Thin Solid Films* **2008,** *516*, 5822-5828.

20. Gordon, R. G., *MRS Bull.* **2000,** *25*, 52-57.

21. Della Gaspera, E.; Bersani, M.; Cittadini, M., et al., *J. Am. Chem. Soc.* **2013,** *135*, 3439-3448.

22. Kevin, M.; Tho, W. H.; Ho, G. W., *J. Mater. Chem.* **2012,** *22*, 16442-16447.

23. Park, S.-M.; Ikegami, T.; Ebihara, K., *Thin Solid Films* **2006,** *513*, 90-94.

24. Agura, H.; Suzuki, A.; Matsushita, T., et al., *Thin Solid Films* **2003,** *445*, 263-267.

25. Amma, D. S. D.; Vaidyan, V. K.; Manoj, P. K., *Mater. Chem. Phys.* **2005,** *93*, 194-201.

26. Liu, S.; Ding, W.; Gu, Y., et al., *Phys. Scripta* **2012,** *85*, 065601.

27. Bekisli, F.; Stavola, M.; Fowler, W. B., et al., *Phys. Rev. B* **2011,** *84*, 035213.

28. Singh, A. K.; Janotti, A.; Scheffler, M., et al., *Phys. Rev. Lett.* **2008,** *101*, 055502.

29. Kılıç, Ç.; Zunger, A., *Phys. Rev. Lett.* **2002,** *88*, 095501.

30. White, M. E.; Tsai, M. Y.; Wu, F., et al., *J. Vac. Sci. Technol. A* **2008,** *26*, 1300-1307.

31. Lee, S. W.; Kim, Y. W.; Chen, H., *Appl. Phys. Lett.* **2001,** *78*, 350-352.

32. Moholkar, A. V.; Pawar, S. M.; Rajpure, K. Y., et al., *Appl. Surf. Sci.* **2009,** *255*, 9358-9364.

33. Fuchs, F.; Bechstedt, F., *Phys. Rev. B* **2008,** *77*, 155107.

34. Wang, C. Y.; Cimalla, V.; Romanus, H., et al., *Appl. Phys. Lett.* **2006,** *89*, 011904.

35. Zachariasen, W. H., *Geologiska Föreningen i Stockholm Förhandlingar* **1929,** *51*, 123-123.

36. Bartos, A.; Lieb, K. P.; Uhrmacher, M., et al., *Acta Crystallogr. B* **1993,** *49*, 165-169.

37. Weiher, R. L.; Ley, R. P., *J. Appl. Phys.* **1966,** *37*, 299-302.

38. Walsh, A.; Da Silva, J. L. F.; Wei, S. H., et al., *Phys. Rev. Lett.* **2008,** *100*, 255501.

39. King, P. D. C.; Veal, T. D.; Fuchs, F., et al., *Phys. Rev. B* **2009,** *79*, 205211.

40. King, P.; Veal, T.; Payne, D., et al., *Phys. Rev. Lett.* **2008,** *101*, 116808.

41. Lany, S.; Zunger, A., *Phys. Rev. Lett.* **2007,** *98*, 045501.

42. Lany, S.; Zakutayev, A.; Mason, T. O., et al., *Phys. Rev. Lett.* **2012,** *108*, 016802.

43. Medvedeva, J. E.; Hettiarachchi, C. L., *Phys. Rev. B* **2010,** *81*, 125116.

44. Preissler, N.; Bierwagen, O.; Ramu, A. T., et al., *Phys. Rev. B* **2013,** *88*, 085305.

45. Libera, J. A.; Hryn, J. N.; Elam, J. W., *Chem. Mater.* **2011,** *23*, 2150-2158.

46. Gassenbauer, Y.; Schafranek, R.; Klein, A., et al., *Phys. Rev. B* **2006,** *73*, 245312.

47. Maruyama, T.; Tago, T., *Appl. Phys. Lett.* **1994,** *64*, 1395-1397.

48. Perkins, J. D.; del Cueto, J. A.; Alleman, J. L., et al., *Thin Solid Films* **2002,** *411*, 152-160.

49. Mizoguchi, H.; Chen, P.; Boolchand, P., et al., *Chem. Mater.* **2013,** *25*, 3858-3866.

50. Liu, H. R.; Yang, J. H.; Xiang, H. J., et al., *Appl. Phys. Lett.* **2013,** *102*, 112109.

51. Lee, I.-J.; Sung, N.-E.; Chae, K. H., et al., *Thin Solid Films* **2013,** *548*, 385-388.

52. Choi, Y. Y.; Kang, S. J.; Kim, H. K., *Curr. Appl. Phys.* **2012,** *12*, S104-S107.

53. Phillips, J. M.; Kwo, J.; Thomas, G. A., et al., *Appl. Phys. Lett.* **1994,** *65*, 115-117.

54. Nomura, K.; Ohta, H.; Ueda, K., et al., *Science* **2003,** *300*, 1269-1272.

55. Nomura, K.; Ohta, H.; Takagi, A., et al., *Nature* **2004,** *432*, 488-492.

56. Miller, M. S.; O'Kane, J. C.; Niec, A., et al., *ACS Appl. Mater. Inter.* **2013,** *5*, 10165-10172.

57. Park, S. E.; Kim, S.; Lee, D. Y., et al., *J. Mater. Chem. A* **2013,** *1*, 14286-14293.

58. Zhang, D.; Wang, R.; Wen, M., et al., *J. Am. Chem. Soc.* **2012,** *134*, 14283-14286.

59. Rathmell, A. R.; Wiley, B. J., *Adv. Mater.* **2011,** *23*, 4798-4803.

60. Rathmell, A. R.; Bergin, S. M.; Hua, Y. L., et al., *Adv. Mater.* **2010,** *22*, 3558-3563.

61. Sanchez-Iglesias, A.; Rivas-Murias, B.; Grzelczak, M., et al., *Nano Lett.* **2012,** *12*, 6066-6070.

62. Mirri, F.; Ma, A. W. K.; Hsu, T. T., et al., *ACS Nano* **2012,** *6*, 9737-9744.

63. Bult, J. B.; Crisp, R.; Perkins, C. L., et al., *ACS Nano* **2013,** *7*, 7251-7261.

64. Li, R.; Parvez, K.; Hinkel, F., et al., *Angew. Chem. Int. Ed.* **2013,** *52*, 5535-5538.

65. Novoselov, K. S.; Geim, A. K.; Morozov, S. V., et al., *Science* **2004,** *306*, 666-669.

66. Geim, A. K.; Novoselov, K. S., *Nature Mater.* **2007,** *6*, 183-191.

67. Wang, X.; Zhi, L.; Mullen, K., *Nano Lett.* **2008,** *8*, 323-327.

68. Geng, H. Z.; Kim, K. K.; So, K. P., et al., *J. Am. Chem. Soc.* **2007,** *129*, 7758-7759.

69. Bae, S.; Kim, H.; Lee, Y., et al., *Nature Nanotech.* **2010,** *5*, 574-578.

70. Seki, S.; Sawada, Y.; Ogawa, M., et al., *Surf. Coat. Tech.* **2003,** *169–170*, 525-527.

71. Scherer, V.; Janowitz, C.; Krapf, A., et al., *Appl. Phys. Lett.* **2012,** *100*, 212108.

72. Mryasov, O. N.; Freeman, A. J., *Phys. Rev. B* **2001,** *64*, 233111.

73. Lange, B.; Freysoldt, C.; Neugebauer, J., *Phys. Rev. B* **2010,** *81*, 224109.

74. Medvedeva, J., *Phys. Rev. Lett.* **2006,** *97*, 086401.

75. Ellmer, K., *J. Phys. D-Appl. Phys.* **2001,** *34*, 3097-3108.

76. Ellmer, K.; Mientus, R., *Thin Solid Films* **2008,** *516*, 4620-4627.

77. Pei, Z. L.; Sun, C.; Tan, M. H., et al., *J. Appl. Phys.* **2001,** *90*, 3432-3436.

78. Bel Hadj Tahar, R.; Ban, T.; Ohya, Y., et al., *J. Appl. Phys.* **1998,** *83*, 2631-2645.

79. Frank, G.; Kostlin, H., *Appl. Phys. A-Mater.* **1982,** *27*, 197-206.

80. Hummel, R., *Electronic Properties of Materials*, Springer New York, **2011**, 227-246.

81. Grundmann, M., *The Physics of Semiconductors*, Springer Berlin Heidelberg, **2010,** 265-307.

82. Haacke, G., *J. Appl. Phys.* **1976,** *47*, 4086-4089.

83. Betz, U.; Olsson, M. K.; Marthy, J., et al., *Surf. Coat. Tech.* **2006,** *200*, 5751-5759.

84. Ginley, D. S., *Handbook of Transparent Conductors*, Springer US, **2011**, 507-526.

85. Bühler, G.; Thölmann, D.; Feldmann, C., *Adv. Mater.* **2007,** *19*, 2224-2227.

86. Lee, J.; Lee, S.; Li, G. L., et al., *J. Am. Chem. Soc.* **2012,** *134*, 13410-13414.

87. Seki, S.; Sawada, Y.; Ogawa, M., et al., *Surf. Coat. Tech.* **2003,** *169*, 525-527.

88. Maruyama, T.; Kojima, A., *Jpn. J. Appl. Phys.* **1988,** *27*, L1829-L1831.

89. Tahar, R. B. H.; Ban, T.; Ohya, Y., et al., *J. Appl. Phys.* **1998,** *83*, 2139-2141.

90. Seki, S.; Sawada, Y.; Nishide, T., *Thin Solid Films* **2001,** *388*, 22-26.

91. Ota, R.; Seki, S.; Ogawa, M., et al., *Thin Solid Films* **2002,** *411*, 42-45.

92. Al-Dahoudi, N.; Aegerter, M. A., *Thin Solid Films* **2006,** *502*, 193-197.

93. Tang, W.; Cameron, D. C., *Thin Solid Films* **1994,** *238*, 83-87.

94. Gross, M.; Linse, N.; Maksimenko, I., et al., *Adv. Eng. Mater.* **2009,** *11*, 295-301.

95. Curiel, D.; Más-Montoya, M.; Chang, C.-H., et al., *J. Mater. Chem. C* **2013,** *1*, 3421-3429.

96. Hotchkiss, P. J.; Jones, S. C.; Paniagua, S. A., et al., *Accounts Chem. Res.* **2011,** *45*, 337-346.

97. Armstrong, N. R.; Veneman, P. A.; Ratcliff, E., et al., *Accounts Chem. Res.* **2009,** *42*, 1748-1757.

98. Carter, C.; Brumbach, M.; Donley, C., et al., *J. Phys. Chem. B* **2006,** *110*, 25191-25202.

99. Armstrong, N. R.; Carter, C.; Donley, C., et al., *Thin Solid Films* **2003,** *445*, 342-352.

100. Donley, C.; Dunphy, D.; Paine, D., et al., *Langmuir* **2002,** *18,* 450-457.

101. Wen, B.; Melnik, R.; Yao, S., et al., *Mat. Sci. Semicon. Proc.* **2010,** *13,* 295-297.

Chapter 2

Solution Deposition of Highly Transparent and Conductive ITO Thin Films with a High Figure of Merit

2.1 Introduction

As reviewed in **Chapter 1**, highly conductive and transparent TCO films have been conventionally deposited by various vapor deposition techniques with sputtering at a commercial scale.[1] Vapor deposition offers TCO films with dense structures and benchmark properties (resistivity: $\rho=1\sim2\times10^{-4}$ Ω·cm, transparency: T>85%). Unfortunately, the requirement of high vacuum and sophisticated equipment, indispensably associated with vapor deposition processes, severely limits the applicability of the technology for broad industrial utilities. The possibility of replacing vapor deposition with simple and solution-based methods to achieve similar quality of TCO films represents a great challenge for materials chemistry and surface science and has been a subject of intense research activities in recent years.[1-2] The solution deposition methods require no vacuum and sophisticated equipment and thus enable thin film fabrication with larger scalability and lower processing costs.[2-4] To date, two solution processes, one based on TCO nanoparticles and another on sol-gels, for film deposition have been proposed.

For a nanoparticle-based process, dispersions of TCO nanoparticles remain as a delicate choice. One can tune the sizes, morphologies, compositions and

dispersibilities of TCO nanoparticles in a nonpolar or polar solvent through careful control of synthesis conditions.[5-7] Recently, Lee et al. assembled an indium-tin-oxide (ITO) thin film from monodisperse nanoparticles with relatively low resistivity (5.2×10^{-3} Ω·cm) and high transparency (93%). The sheet resistance of 356 Ω/sq is the lowest of all reported ITO nanoparticulate films and essentially meets the requirement of touch screen.[6, 8] In general, long-chain surfactants or polymers are required to prevent agglomeration of nanoparticles. The decomposition of these organics during thermal annealing and packing of the nanoparticulate building blocks on a substrate give rise to high porosity of TCO films, which limits the film resistivity still at one to two orders of magnitude higher than the sputtering benchmark.[6-7, 9] In addition, the weak control of nanoparticle size, morphology and dispersibility in large-scale synthesis can exert a strong influence on the film roughness.

A competitive alternative is based on a sol-gel process, which has been shown to produce TCO films with better quality, lower porosity and lower resistivity.[10] It was reported that the resistivity of a sol-gel processed ITO film can even reach the level of 10^{-4} Ω·cm,[11-15] close to the standard value commonly achieved by sputtering. Only a reasonably thin ITO film at this level of resistivity may have a low sheet resistance and, at the same time, a high transparency.

To quantitatively evaluate the performance of a transparent conductive film with different thickness, resistivity and transparency, Haacke proposed a revised figure of merit (FOM), as defined by Equation (1-7).[16] A higher value of FOM indicates better performance of a film, which requires a low sheet resistance and high transparency. However, as reviewed in **Chapter 1**, a trade-

off exists between the conductivity and transparency due to the plasma absorption. As a consequence, the FOM value cannot be unlimitedly high.

With Φ_H as the basic criterion of film quality, nanoparticulate TCO films usually exhibit a low FOM on the order of 10^{-4} Ω^{-1}. Due to their high sheet resistance and/or low transparency, most sol-gel processed ITO films exhibit the same order or modestly higher value of FOM as nanoparticulate ITO films.[3, 13, 15, 17] One exceptionally high FOM of 1.17×10^{-2} Ω^{-1} was acquired by Seki,[14] which is comparable to that of the polycrystalline ITO film prepared by sputtering.[18] The minimum sheet resistance achieved is 7 Ω/sq which can meet high-end applications. Unfortunately, the transparency around 78% is much lower than the basic requirement for transparent conductors (T>85%). In addition, fabrication of the ITO film requires 30 coatings, which makes the process highly time-consuming and inefficient. The toxicity, high cost and inaccessibility of the metal alkoxide precursors further compromise the advantage of the sol-gel process.

Most sol-gel processes of ITO film deposition employ acetylacetone as the ligand to stabilize In^{3+} cations by forming chelation compounds to lower the hydrolysis rate of In^{3+}. The dopant from tin salts ($SnCl_2$, $SnCl_4$, etc.) is dissolved in alcohol (ethanol, methanol, isopropanol, etc.) to form an alcoholic solution. Prior to film coating, the two solutions are simply mixed.[11, 19-21] Several previous studies showed that the hydrolysis of tin (II) and tin (IV) readily occurs in ethanol to form SnO_2 nanocrystals (1 nm to 3 nm).[22-24] The pre-formed SnO_2 nanocrystal may act as a nucleation center to grow In_2O_3.[25] Non-uniform growth can lead to aggregation of nanoparticles and formation of islands,[26] which affect the film microstructures, uniformity and conductivity.

In this Chapter, we report a simple but effective sol-gel method to fabricate highly uniform, conductive and transparent ITO thin films. In a conventional sol-gel process, solutions of indium and tin salts were first made separately and then mixed together upon film deposition. This procedure may give rise to inconsistent quality and performance of ITO films due to the poor uniformity. In the present study, the indium and tin salts are both dissolved together in acetylacetone to stabilize Sn^{4+} cations. As a consequence, highly uniform, transparent and conductive ITO films are obtained. The film resistivity (7.2×10^{-4} Ω·cm), sheet resistance (30 Ω), transparency (90.2%) and surface roughness (1.14 nm) all surpass or become comparable to the best performance of recently developed nanoparticle-based solution processes and, more importantly, to the benchmark performance of DC sputtering. The film displays the best combination of conductivity and transparency, showing the highest figure of merit (1.19×10^{-2} Ω^{-1}) among all reported solution-processed ITO films.

2.2 Experiments

All chemicals were used without any purification. Indium nitrate hydrate (99.9%, Aldrich) and tin (IV) chloride hydrate (99.9%, Alfa) were dissolved together in acetylacetone with $[In^{3+}]$ =1 mol/L and different dopant percentages from 0% to 15%. Here the dopant percentage is defined as Sn%= Sn/(Sn+In) in atomic ratio. The solutions were kept at 60 ^{o}C overnight. After incubation, the solutions became transparently brown, indicating the formation of metal acetylacetonate complexes. The solutions were highly homogeneous and stable and can be stored for more than six months without formation of any precipitates.

2.2.1 Film Deposition

ITO/glass films were prepared by spin coating of the solutions at 4000 rpm for 60 seconds in air for simple fabrication of ITO films. Prior to spin coating, glass substrates (Asahi, 40 × 40 × 0.55 mm × mm × mm) were sequentially washed under sonication with acetone, de-ionized water and ethanol for 10 min each. The substrates were dried in an oven and then treated with a Novascan UV-ozone cleaner (PSDP-UV12T) for 15 min. After coating, the wet films were dried at 120 ^{o}C for 10 min and then annealed for 10 min at 400 ^{o}C in air. The procedure of coating, drying and annealing was repeated 5 times to achieve desired thickness. A final annealing in H_2/Ar gas mixture (v/v=5/95) was conducted in a tube furnace at 300 ^{o}C for 3 h with a heating ramp of 5 ^{o}C/min.

2.2.2 Characterization

X-ray diffraction (XRD) patterns were collected on a PANAlytical EMPYREAN X-ray diffractometer with Cu Kα source (λ=1.5418 Å), operating on a θ/2θ configuration at 40 kV and 30 mA. Scan range was from 20^{o} to 70^{o} with the step of 0.02^{o}. Jade 6.5 (Materials Data Inc.) was used to fit the XRD patterns and calculate lattice constants. Images of scanning electron microscopy (SEM) and atomic force microscopy (AFM) were taken from a JOEL JSM-6701F field emission SEM and a Veeco Nanoscope IIIa tapping-mode AFM, respectively. Transmittance of thin films was measured by a Shimadzu UV-2550 ultra-violet visible (UV-vis) spectrometer. Fourier transform infrared (FTIR) spectra were collected on a Varian 3100 FTIR spectrometer (resolution 2 cm^{-1}, 64 scans). Sheet resistance was recorded from a four-point probe station and source meter (Keithley 2400C) by an average of

five readings. X-ray photoelectron spectroscopy (XPS) was performed on a Kratos AXIS Ultra HAS spectrometer equipped with a monochromatic Al Kα X-ray source (hv=1486 eV), operating at 15 kV and 5 mA. Peak fitting was performed with the software XPSPEAK 4.1 and a Shirley background subtraction.

2.3 Results and Discussion

2.3.1 Crystal Structure and Film Resistivity

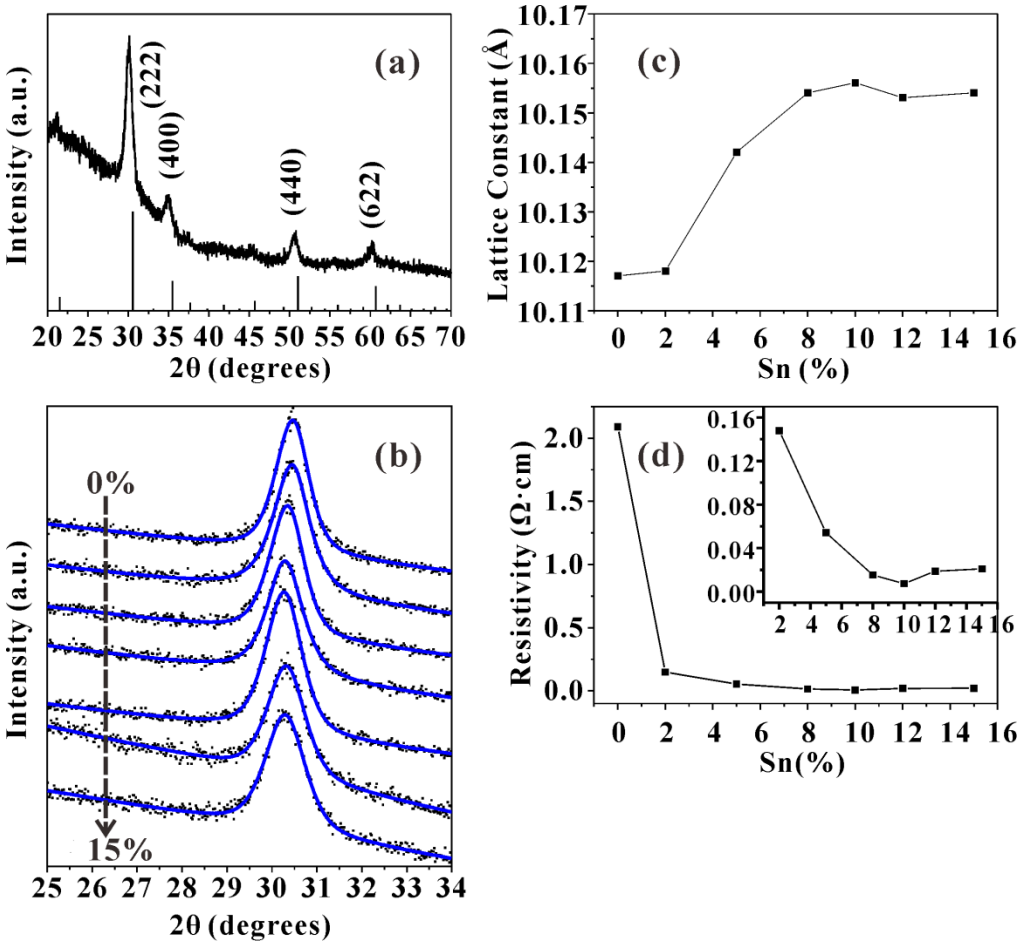

Figure 2-1: (a) XRD pattern of the ITO film (Sn%=10%); Dependence of the (b) XRD (222) peak positions, (c) lattice constants and (d) film resistivities versus dopant percentages: 0%~15%. (Blue lines are the corresponding fitted curves.)

A typical XRD pattern of the ITO film (Sn=10%) after annealing in H_2/Ar is shown in Figure 2-1a. All the diffraction peaks can be indexed to the body-centered cubic bixbyite In_2O_3 structure. The standard pattern (PDF no. 06-

0416) is given for the comparison. The increased background towards low angle is attributed to the amorphous glass substrate. The pattern shows three major diffraction peaks of (222), (440) and (400) Miller planes, similar to the pattern of randomly oriented powder. After peak fitting, the integrated peak area ratio of (222) to (440), $S_{(222)}/S_{(400)}$, is found to be 5.09, much larger than the random orientation ratio of 2.86. The ratio of $S_{(440)}$ to $S_{(400)}$ remains close to the standard (1.15 *vs.* 1.17). Therefore, the film shows a weak (222) texture, which has the lowest surface energy among the three low-index surfaces: $\gamma(100) > \gamma(110) > \gamma(222)$.[27]

Figure 2-1b displays the dependence of (222) peak positions *versus* dopant percentages. As the dopant percentage increases from 0% to 10%, the (222) peak position slightly shifts toward a lower angle. The variation of lattice constants of ITO films *vs* dopant percentage is obtained after peak fitting of the (222) diffraction plane. The results are presented in Figure 2-1c. Without doping with Sn, the lattice constant of In_2O_3 film (a=10.117 Å) is close to that of the standard In_2O_3 powder (a=10.118 Å). As the dopant percentage increases, the lattice constant increases significantly. The variation of the lattice constant contradicts the Vegard's law, which predicts a linear decrease of alloy lattice as the concentration of smaller size dopant increases.[28] Nevertheless, a similar trend of lattice variation upon doping was also observed by several studies.[29-30] Nadaud et al. demonstrated that an increase of tin content would simultaneously introduce interstitial oxygen atoms, which results in lattice expansion.[29] Beyond 10%, lattice parameters remain nearly constant, indicating that the solubility of Sn in In_2O_3 is around 10%.

Figure 2-1d shows the resistivities of ITO films varying with different dopant concentrations. Interestingly, with the increase of dopant concentration, the film resistivity exhibits an inversed trend compared with the lattice constant. The resistivity decreases dramatically as the tin concentration increases from 0% to 10%, indicating the effectiveness of Sn^{4+} doping in the In_2O_3 matrix. Further increasing the dopant concentration does not lead to the reduction of electrical resistivity. The resistivity reaches the minimum value of 7.32×10^{-3} Ω·cm when Sn%=10%. The slight increase of resistivity upon the dopant concentration exceeding 10% is attributed to the increased concentration of ionizable complex ($Sn_2^{\cdot}O_i^{''}$) and neutral complex $(Sn_2O_4)^x$, which reduces carrier mobility and doping efficiency.[12, 30] Therefore, Sn=10% is chosen as the focal dopant percentage in the present study to investigate the morphology, roughness, surface composition and optical property of ITO thin films.

2.3.2 Film Microstructure and Morphology

Figure 2-2 shows the morphologies of an ITO film (Sn=10%) after annealing in hydrogen gas. Figures 2-2a and 2b indicate that the ITO film has a very smooth and uniform surface without any large aggregates, which is a highly desired feature for applications in various electronic devices. The cross-section of the thin film displays a uniform thickness about 240 nm after five layers of ITO coating on a glass substrate (Figure 2-2c). The AFM image further confirms the smoothness and uniformity of the ITO film (Figure 2-2d). The particle size is around 5.2 nm based on the analysis of a 2μm×2μm area of AFM image. The average particle size is close to the result obtained from XRD pattern based on Scherrer equation (4.4 nm). The analysis of the AFM

image gives a root-mean-square roughness, R_{ms}, of 1.14 nm, comparable to that of the ITO film deposited by sputtering (1.1 nm).[18]

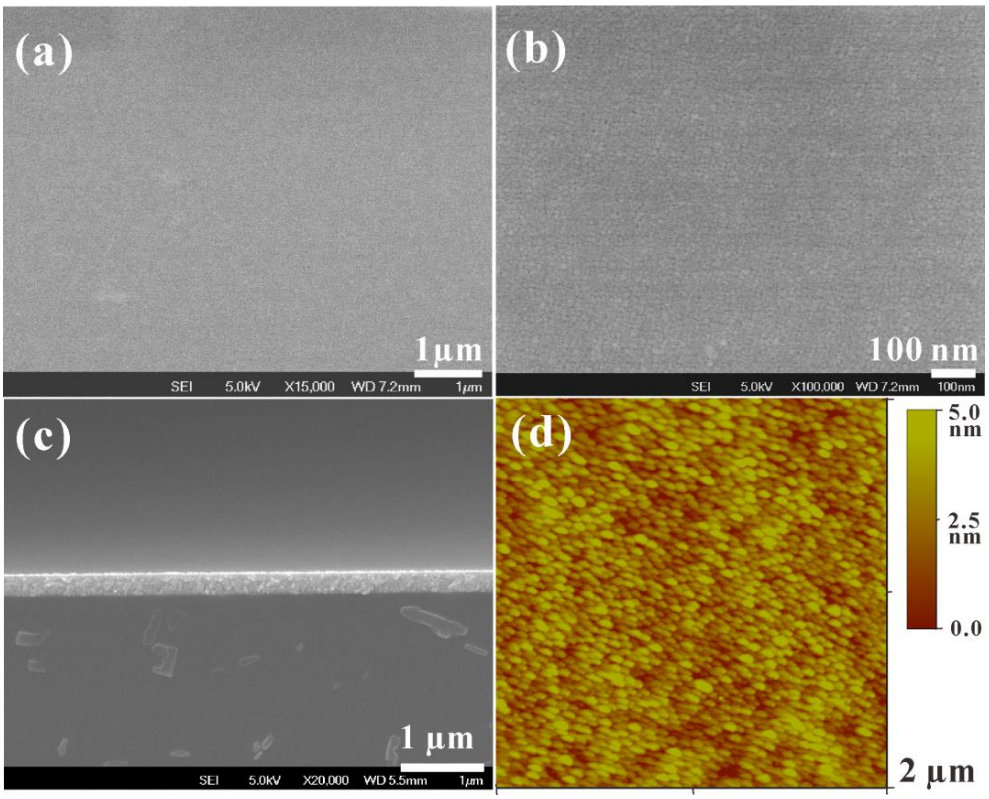

Figure 2-2: Morphologies of ITO film (Sn=10%) after annealing in H_2/Ar: (a, b, and c) SEM images; (d) AFM image. (Part c shows the film cross-section)

2.3.3 Surface Composition of ITO Film

The surface properties of TCO films, including work function and surface compositions are very important for their applications. A high work function of ITO films is always required to improve the hole-transport efficiency in organic electronics. The surface composition is even more important for their applications, since impurities can act as the surface trapping centers of free carriers to affect their electrical properties. The XPS survey scan on the ITO thin film indicates that no detectable elements are present on the film except carbon, oxygen, indium and tin. No contamination from nitrogen and chlorine was discerned during the fine scans (Figure 2-3a and 3b).

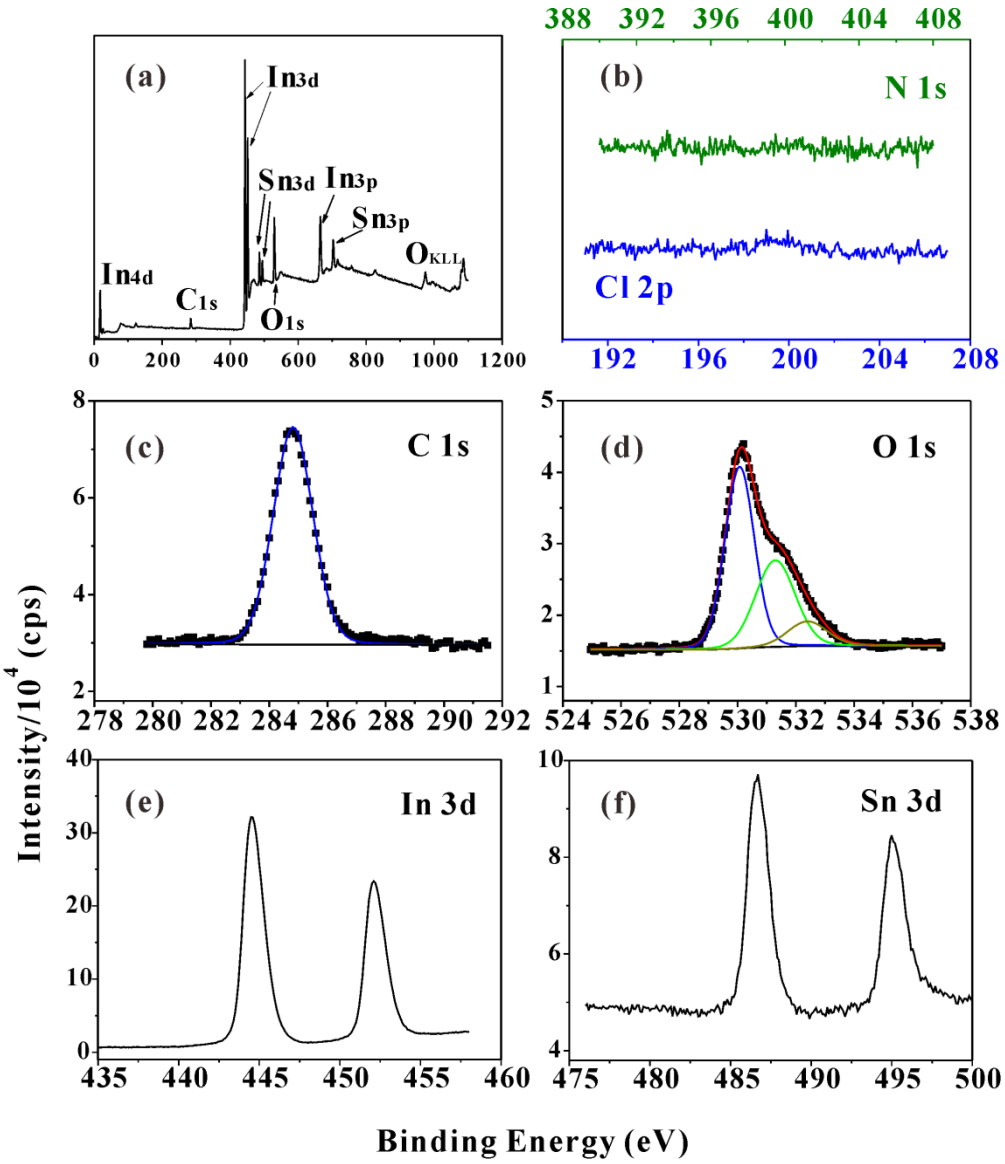

Figure 2-3: XPS spectra of ITO films after H_2 annealing: (a) survey scan; (b-f) core-level fine scans.

The C1s core-level spectrum of the ITO film upon annealing in a H_2/Ar mixed gas can be fitted into a single composition located at the binding energy of 284.8 eV (Figure 2-3c). This comes from the aliphatic airborne contamination, which can be removed through Ar^+ bombardment.[31] Fitting the O1s spectrum (Figure 2-3d) results in three components, situated at 530.07 eV, 531.29 eV and 532.39 eV, respectively. The first two are assigned to bulk oxide and surface oxygen-deficient oxide components. The third composition

arises from the surface hydroxyl groups.[32] The relative elemental ratio can be calculated by $\frac{S_A / ASF_A}{S_B / ASF_B}$, where *S* and *ASF* refer to the integrated peak area and atomic sensitivity factor, respectively. The atomic sensitivity factors are 4.3 and 3.9 for $Sn3d_{5/2}$ and $In3d_{5/2}$ core level electrons, respectively. The ratio of Sn/(Sn+In) was calculated to be 10.9%, modestly higher than the nominal dopant concentration of 10%, which was attributed to the surface segregation of tin dopants.[33]

The ITO film with Sn=10% shows the lowest sheet resistance around 310 Ω/sq, still much higher than the required 50 Ω/sq for most applications but slightly lower than the best nanoparticulate ITO film.[6, 8] To further reduce the resistivity, we undertook annealing of the thin film in a H_2/Ar gas for 3 h at 300 ^oC. As a consequence, one order of magnitude improvement in the sheet resistance was achieved. The film shows an average sheet resistance of 30 Ω/sq, corresponding to a specific resistivity of 7.2×10^{-4} Ω·cm, both comparable to those prepared by DC sputtering.[18]

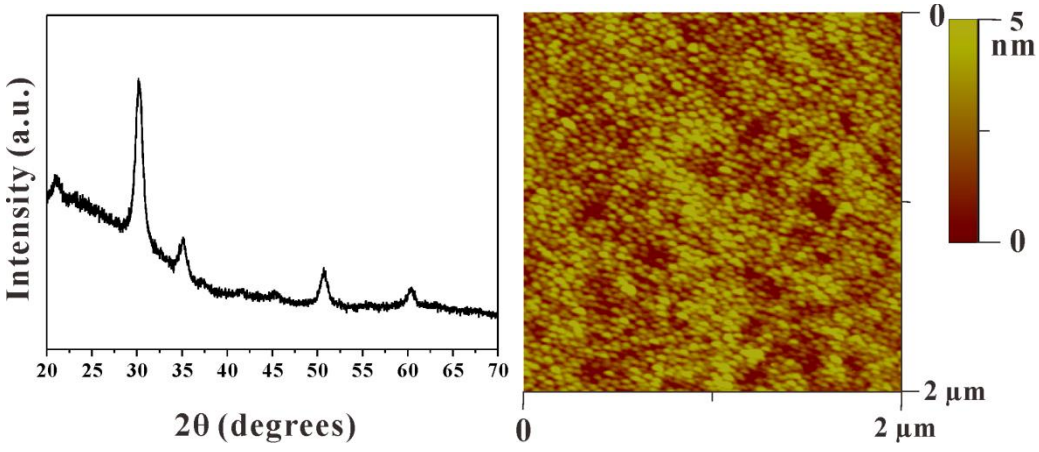

Figure 2-4: XRD pattern and AFM image of ITO film before annealing in H_2/Ar.

No significant difference in the phase and morphology was observed for ITO films before and after annealing in H_2/Ar, except the slightly increased

mean crystalline size (obtained by Scherrer equation) and improved surface smoothness after annealing (Figure 2-4 and Table 2-1). The improvement of conductivity can be attributed to the increased concentration of fully ionizable oxygen vacancies under reducing conditions,[2, 30] which can enhance carrier concentrations. In addition, an increased Hall mobility is also responsible for the improved conductivity after annealing in a reducing atmosphere.[14]

Table 2-1: The structural analysis of ITO films before and after annealing in H_2/Ar.

	Before Annealing	After Annealing
$S_{(222)}/S_{(440)}$	4.90	5.09
$S_{(440)}/S_{(400)}$	1.23	1.15
Mean crystalline size	4.1	4.4
R_{ms} roughness (nm)	1.68	1.14

2.3.4 Optical, Electrical Property and Figure of Merit

The transmittance of ITO film was measured by a UV-vis spectrometer. As shown in Figure 2-5, the film upon five-layer coating displays a transmittance higher than 82% in all the visible range from 400 nm to 700 nm. The spectrum of 0.55mm-thick bare glass substrate is also shown as the reference. The transmittance of the ITO film is as high as 90.22% at the standard wavelength of 550 nm. Based on these parameters, we obtained the Haacke's figure of merit of $1.191 \times 10^{-2}\ \Omega^{-1}$ for the ITO film. Table 2-2 compares the properties of typical ITO films prepared via sol-gel processes, nanoparticle dispersion and DC magnetron sputtering, respectively. To the best of our knowledge, this is

the highest FOM among polycrystalline ITO films deposited via a solution process.

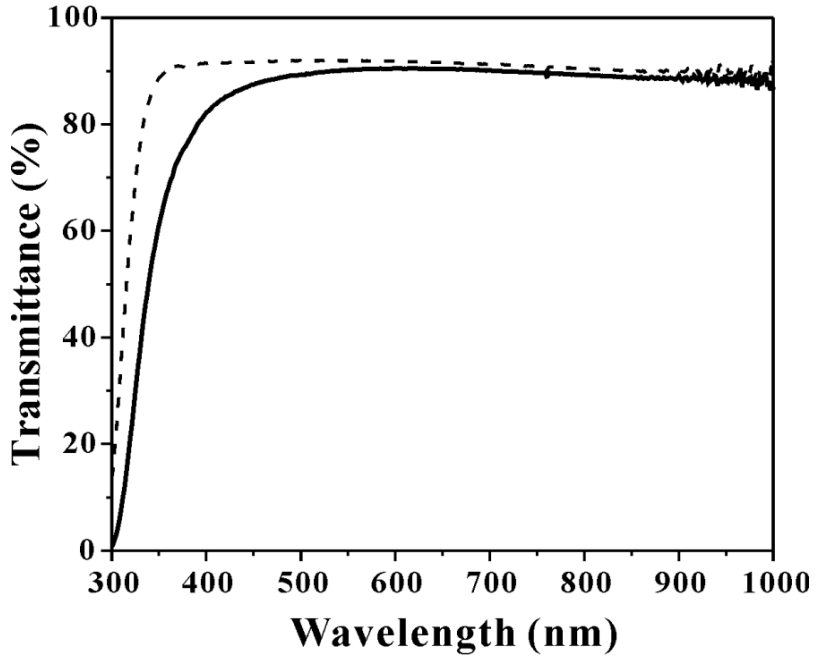

Figure 2-5: UV-vis spectrum of ITO film (Sn=10%) after H_2 annealing. (Dashed line shows the transparency of glass substrate.)

Table 2-2: The properties of typical ITO films prepared by various deposition processes.

No.	ρ (10^{-4} Ω·cm)	R_s (Ω)	t (nm)	T (%) 550	Φ_H (10^{-2} Ω^{-1})	Process	Ref.
1	45.9	379	121	~88	0.073	Spin coating	9
2	4.23 ~55	29.4 ~573	144 96	~96	0.116	Dip coating	17
3	3.2	21	150			Dip coating	18
4	5.8	64	90	~87	0.386	Dip coating	19
5	2.5	42	60	~85	0.469	Dip coating	21
6	2.1	7.1	295	~78	1.171	Dip coating	20
7	5.7	100	57	~70	0.028	Dip coating	23
8	52	356	146	93	0.136	Spin coating	12[a]
9	2.2	22	100	~92[c]	1.974	Sputtering	24[b]

10	7.2	30	241	90.2	1.191	Spin coating	This work

a: prepared via ITO nanoparticle dispersion;

b: prepared by DC magnetron sputtering;

c: the transmittance without glass substrate.

2.3.5 Chelation Effect

It is important to point out that the effective chelation of tin (IV) ions by acetylacetone that slows down the hydration rate of Sn^{4+} facilitates the uniform growth of ITO thin films. Previous investigations have shown that the growth of SnO_2 nanoparticles (from 1 nm to 3 nm) readily occurs via the hydrolysis of Sn^{2+} in an ethanolic solution under ambient conditions without heat or hydrothermal treatment.[22-23] The hydrolysis of Sn^{4+} is expected to occur more readily due to its higher charge/radius ratio, more in favor of nucleophilic reactions, such as hydrolysis.[34]

The FTIR spectroscopy was used to investigate the hydrolysis of $SnCl_4$ in ethanol. As shown in Figure 2-6a, there are several absorption bands below 1000 cm^{-1} assigned to the vibrations of SnO_2 lattice. The strong absorption bands around 1533 cm^{-1} and 1421 cm^{-1} are attributed to the overtones of asymmetric Sn-O-Sn modes.[35] Kim et al. also observed them in the *in-situ* Diffuse Reflectance Infrared Fourier Transform Spectroscopy (DRIFT) during the annealing process of ITO hydroxide precursor from 80 ^oC to 360 ^oC.[36] They found that the intensities of the two peaks increased with the increment of annealing temperature above 240 ^oC, where the hydroxide precursor started to form ITO nanocrystals. The corresponding assignments are listed in Table 2-3, based on the reported references.[35-37] The two unassigned peaks at 1340

cm^{-1} and 1023 cm^{-1} was retained after drying the pellet under vacuum at 80 ^{o}C for 72 h. Therefore, they should be aroused from the product upon hydrolysis, not the residual ethanol.

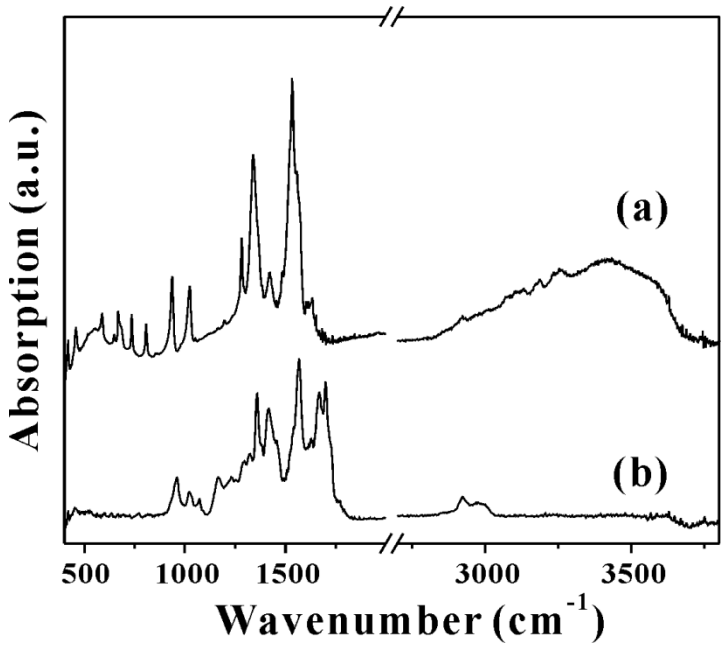

Figure 2-6: FTIR spectra of the dried sol-gel samples prepared by dissolving $SnCl_4$ in (a) ethanol; (b) acetylacetone.

Table 2-3: FTIR peak positions and corresponding assignments.

$SnCl_4$+Ethanol		$SnCl_4$+Acetylacetone	
Frequency (cm^{-1})	Assignment	Frequency (cm^{-1})	Assignment
585		956	δ(C=C)
647	ν(Sn-O)	1022	
670	ν(Sn-O)	1070	
684	ν(Sn-O)	1165	δ_{CH}
736	ν_{as}(Sn-O-Sn)	1357	δ(CH_3)
806		1412	δ(CH_3)
934	δ_{OH}(Sn-OH)	1563	ν(C=C)
1023		1630	δ_{OH}(H_2O)
1282	δ_{OH}(Sn-OH)	1666	ν(C=O)

1340		1700	ν(C=O)
1421	$2\nu_{as}$(Sn-O-Sn)	2921	$\nu(CH_3)$
1533	$2\nu_{as}$(Sn-O-Sn)	2979	ν(CH)
1630	$\delta_{OH}(H_2O)$		
3160~3600	$\nu_{OH}(H_2O)$		

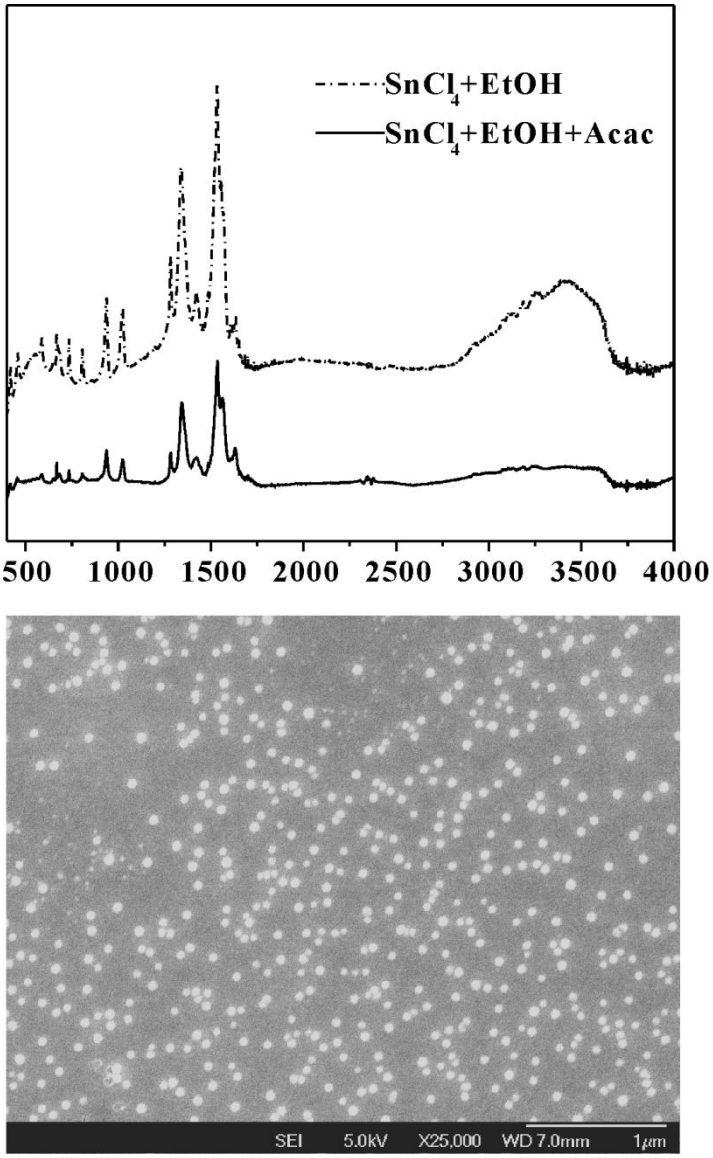

Figure 2-7: FTIR spectrum of the vacuum-dried sample and SEM image of ITO film prepared by conventional sol-gel process.

The previous FTIR spectrum suggests that the hydrolysis of tin (IV) cations already occurs upon the dissolution of $SnCl_4$ in ethanol. To examine the efficiency of the chelation of Sn^{4+} by acetylacetone after the hydrolysis, an equivalent volume of acetylacetone was added into the ethanolic solution of $SnCl_4$ to mimic the conventional process utilized in other references. The FTIR spectrum (Figure 2-7) does not show a major difference compared with that of ethanolic $SnCl_4$ solution, implying that the simple mixing process is ineffective to chelate the hydrolyzed product. In comparison, the chelation is more effective if $SnCl_4$ is directly dissolved in acetylacetone followed by heating at 60 ^oC. The IR spectrum is shown in Figure 2-6b, which displays completely different absorption features. The absorption bands around 1700 cm^{-1} and 1666 cm^{-1} are due to the stretching of C=O in keto and enol forms of free acetylacetone. The peak at 1563 cm^{-1}, corresponding to the conjugated C=C bond, clearly shows the chelation between Sn and acetylacetone.[38] The respective assignments are listed in Table 2-3, according to previous references.[38-40]

The controlled experiments we conducted indicate that ITO films have a relatively rough surface if without effective chelation of tin cations by acetylacetone (Figure 2-7). The small SnO_2 nanoparticles formed after hydrolysis of Sn^{4+} in ethanol may serve as the nucleation centers during the growth and crystallization of ITO nanocrystals. Therefore, non-uniform growth of ITO nanocrystals would result in rougher and more porous film microstructures,[26] leading to a much higher electrical resistivity (~4.4×10^{-2} Ω·cm). Therefore, by stabilizing both cations, our simplified sol-gel process

can improve the film quality effectively, leading to the enhanced performance of transparent conducting films.

2.4 Conclusion

We have developed a simple and effective sol-gel process to prepare transparent conductive ITO films. The chelation of Sn^{4+} by acetylacetone molecules prior to its hydrolysis can be effectively achieved, which facilitates the formation of more uniform and smooth film microstructures. As a consequence, the ITO thin film with Sn=10% displays a high transparency (90.2%) and low resistivity (7.2×10^{-4} Ω·cm) after annealing in a reducing gas. The highest figure of merit was achieved among all the solution-processed ITO films, even comparable to that of polycrystalline ITO film produced by DC magnetron sputtering. The high transparency, low sheet resistance (30 Ω/sq) and low surface roughness (1.14 nm) can meet the requirements for most practical applications. Compared with the nanoparticle-based solution processes, the new sol-gel process is stable and simple but capable of delivering highly reproducible performance of thin films with the sheet resistance an order of magnitude lower and FOM value an order of magnitude higher. While the cost of the new sol-gel process is substantially lower than that of DC sputtering, we show that the performance of the ITO thin films developed in the present study is comparable to that of sputtering. This makes the sol-gel process highly competitive for fabrications of TCO films at a large scale for broader optoelectronic applications.

References

1. Ellmer, K., *Nature Photon.* **2012,** *6*, 808-816.

2. Pasquarelli, R. M.; Ginley, D. S.; O'Hayre, R., *Chem. Soc. Rev.* **2011,** *40*, 5406-5441.

3. Sunde, T. O. L.; Garskaite, E.; Otter, B., et al., *J. Mater. Chem.* **2012,** *22*, 15740-15749.

4. Ahn, B. Y.; Lorang, D. J.; Duoss, E. B., et al., *Chem. Commun.* **2010,** *46*, 7118-7120.

5. Kanehara, M.; Koike, H.; Yoshinaga, T., et al., *J. Am. Chem. Soc.* **2009,** *131*, 17736-17737.

6. Lee, J.; Lee, S.; Li, G. L., et al., *J. Am. Chem. Soc.* **2012,** *134*, 13410-13414.

7. Della Gaspera, E.; Bersani, M.; Cittadini, M., et al., *J. Am. Chem. Soc.* **2013,** *135*, 3439-3448.

8. Geng, H. Z.; Kim, K. K.; So, K. P., et al., *J. Am. Chem. Soc.* **2007,** *129*, 7758-7759.

9. Gross, M.; Linse, N.; Maksimenko, I., et al., *Adv. Eng. Mater.* **2009,** *11*, 295-301.

10. Prodi-Schwab, A.; Luthge, T.; Jahn, R., et al., *J. Sol-Gel Sci. Techn.* **2008,** *47*, 68-73.

11. Maruyama, T.; Kojima, A., *Jpn. J. Appl. Phys.* **1988,** *27*, L1829-L1831.

12. Tahar, R. B. H.; Ban, T.; Ohya, Y., et al., *J. Appl. Phys.* **1998,** *83*, 2139-2141.

13. Seki, S.; Sawada, Y.; Nishide, T., *Thin Solid Films* **2001,** *388*, 22-26.

14. Seki, S.; Sawada, Y.; Ogawa, M., et al., *Surf. Coat. Tech.* **2003,** *169*, 525-527.

15. Ota, R.; Seki, S.; Ogawa, M., et al., *Thin Solid Films* **2002,** *411*, 42-45.

16. Haacke, G., *J. Appl. Phys.* **1976,** *47*, 4086-4089.

17. Ota, R.; Seki, S.; Sawada, Y., et al., *Surf. Coat. Tech.* **2003,** *169*, 521-524.

18. Betz, U.; Olsson, M. K.; Marthy, J., et al., *Surf. Coat. Tech.* **2006,** *200*, 5751-5759.

19. Nishio, K.; Sei, T.; Tsuchiya, T., *J. Mater. Sci.* **1996,** *31*, 1761-1766.

20. Yang, L. L.; Ge, D. T.; He, X. D., et al., *Thin Solid Films* **2009,** *517*, 5151-5156.

21. Chen, J. Z.; Huang, C. P.; Tseng, W. H., et al., *Appl. Surf. Sci.* **2011,** *257*, 10042-10044.

22. Leite, E. R.; Giraldi, T. R.; Pontes, F. M., et al., *Appl. Phys. Lett.* **2003,** *83*, 1566-1568.

23. Ribeiro, C.; Lee, E. J. H.; Giraldi, T. R., et al., *J. Phys. Chem. B* **2004,** *108*, 15612-15617.

24. Rizzato, A. P.; Broussous, L.; Santilli, C. V., et al., *J. Non-Cryst. Solids* **2001,** *284*, 61-67.

25. Kim, D. W.; Hwang, I. S.; Kwon, S. J., et al., *Nano Lett.* **2007,** *7*, 3041-3045.

26. Epifani, M.; Diaz, R.; Arbiol, J., et al., *Chem. Mater.* **2006,** *18*, 840-846.

27. Zhang, K. H. L.; Walsh, A.; Catlow, C. R. A., et al., *Nano Lett.* **2010,** *10*, 3740-3746.

28. Denton, A. R.; Ashcroft, N. W., *Phys. Rev. A* **1991,** *43*, 3161-3164.

29. Nadaud, N.; Lequeux, N.; Nanot, M., et al., *J. Solid State Chem.* **1998,** *135*, 140-148.

30. Frank, G.; Kostlin, H., *Appl. Phys. A-Mater.* **1982,** *27*, 197-206.

31. Chaney, J. A.; Pehrsson, P. E., *Appl. Surf. Sci.* **2001,** *180*, 214-226.

32. Bermudez, V. M.; Berry, A. D.; Kim, H., et al., *Langmuir* **2006,** *22*, 11113-11125.

33. Shigesato, Y.; Takaki, S.; Haranou, T., *Appl. Surf. Sci.* **1991,** *48-9*, 269-275.

34. Sakka, S., *Handbook of Sol-gel Science and Technology: Processing, Characterization, and Applications*, Kluwer Academic Publishers Boston, **2004**, 1, 105.

35. Amalric-Popescu, D.; Bozon-Verduraz, F., *Catal. Today* **2001,** *70*, 139-154.

36. Kim, S.; Bin Kim, S.; Choi, H. C., *B. Korean Chem. Soc.* **2012,** *33*, 194-198.

37. Orel, B.; Lavrencicstangar, U.; Crnjakorel, Z., et al., *J. Non-Cryst. Solids* **1994,** *167*, 272-288.

38. Frycek, R.; Jelinek, M.; Kocourek, T., et al., *Thin Solid Films* **2006,** *495*, 308-311.

39. Nakamoto, K., *Infrared and Raman Spectra of Inorganic and Coordination Compounds*, John Wiley New York, **2009**, 96.

40. Nielsen, G. F.; Silva, L. H. F.; Cruz, N. C., et al., *Surf. Interface Anal.* **2013,** *45*, 1113-1118.

Chapter 3

The Electronic Structures of n-type Doped Indium Oxides as the Transparent Conductors

3.1 Introduction

As reviewed in **Chapter 1**, various dopants, including Sn, Ge, Mo, Nb and Ti, etc.,[1-6] have been used to achieve the n-type doping of indium oxide for transparent conducting films. The carrier concentrations can be significantly enhanced to 10^{21}~10^{22} cm^{-3} after In_2O_3 was degenerately doped with the various n-type dopants and native defects. In addition, a reasonably high carrier mobility (generally μ<100 $cm^2/(V\ s)$) can be obtained after the n-type doping. As a result, the conductivity can be greatly improved compared with undoped In_2O_3.

Among different extrinsic dopants, tin was proven to be the most effective dopant. Sn-doped In_2O_3 (ITO) thin films show the best conductivity at the level of 10^{-4} Ω·cm when the thicknesses of TCO layers are thinned to be below 100 nm. Therefore, currently ITO films are widely used in many electronic devices, especially in high-end displays where extremely low sheet resistance is required (e.g. <10 Ω/sq).

From the electronic structure point of view, the Sn-*5s* states can be strongly hybridized with the O-*2p* anti-bonding orbitals. Thus, the free-electron-like feature of conduction band was well retained after the In_2O_3 host was doped with Sn, implying the effective doping of tin.[7]

In this Chapter, we employ the density functional theory to study the n-type doping of In_2O_3 by the group IVA dopants as well as the fifth-period elements (Sb, Te and I). The variations of geometrical and electronic structures of indium oxide after doping are thoroughly investigated. The band widths, effective masses, electron group velocities and formation energies etc. are systematically compared for these n-doped indium oxide structures. A fundamental understanding of the properties in respect to dopant elements is also discussed.

3.2 Computational Details

The calculations were performed by the density functional theory as implemented in the code Vienna Ab-initio Simulation Package, known as VASP (basic theories are briefly introduced in **Appendix**),[8-9] with the electron-ion interactions described by the projector augmented wave (PAW) method.[10-11] The exchange-correlation potential was incorporated in the generalized gradient approximation (GGA) using the Perdew-Burke-Ernzerhof (PBE) functional.[12] All geometries and unit cells were fully relaxed. The convergence criteria of total energy and total force were 10^{-5} eV and 0.01 eV/Å, respectively. A cutoff energy of 500 eV and a mesh of $9\times9\times9$ Monkhorst-Pack[13] *k*-points were used for the total energy calculation.

The group IVA and fifth-period main group elements, including Sb, Te and I, were used as the external n-type dopants. The *ns* and *np* orbitals of group IVA, and the *5s* and *5p* orbitals of Sb, Te and I were treated as the valence electrons respectively. The experimental crystal structure of the body centered cubic In_2O_3 (space group: $Ia\bar{3}$) was used as the starting structure.[14] The primitive cell of the bixbyite In_2O_3 contains 24 O and 16 In atoms with four

indium occupying the *8b* cationic site and the other indium at the *24d* site. To systemically study the efficiency of different external dopants, the *8b* cationic site was selected as the doping position. The doping concentration was fixed at 6.25 atom% which was achieved by substitutionally replacing one In at the *8b* site with one dopant atom.

3.3 Results and Discussion

3.3.1 The Geometrical Structures of Pristine and n-type Doped In_2O_3

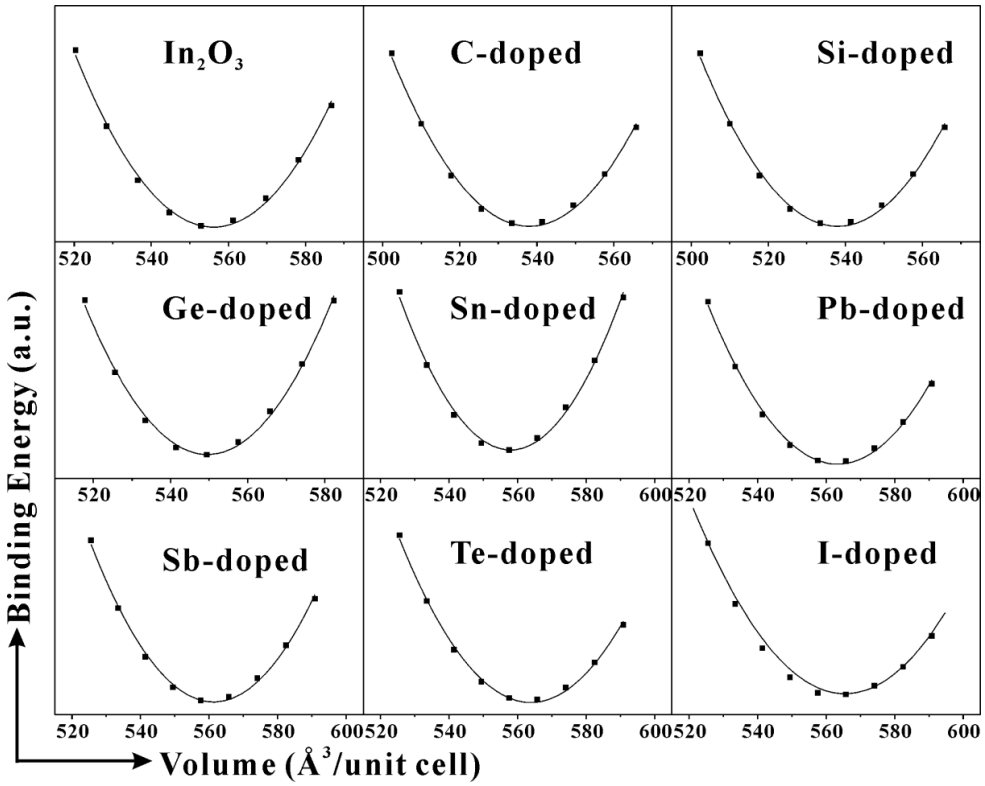

Figure 3-1: The binding energies vs. the volumes of pristine and n-doped In_2O_3. The curves are fitted from the nine points (square) around equilibrium volume.

According to the reference [15], the equilibrium unit cell volume can be extracted by fitting binding energy *versus* volume. Figure 3-1 shows the energy-volume dependencies for the undoped and each doped unit cell. Each curve is fitted by a second-order equation to obtain the lattice constant. According to our results, the In_2O_3 primitive unit cell has an equilibrium

volume around 555 $Å^3$ without any extrinsic impurities. Compared with the pristine In_2O_3 crystal structure, the C-, Si- and Ge-doped unit cells have much smaller equilibrium cell volumes of less than 550 $Å^3$. The tin dopant does not significantly change the cell volume, while Pb and the fifth-period elements (Sb, Te and I) expand the cell volumes to be larger than 560 $Å^3$.

Table 3-1: The relaxed geometrical parameters of pure and n-type doped In_2O_3 structures. M_{8b} refers to the dopant atom at 8b cationic position.

Dopants	**a (Å)**	**Volume ($Å^3$)**	**α,β,γ (°)**	**O-M_{8b} (Å)**	**O-M-O (°)**
	8.96	552.90	109.47	2.22	80.58, 99.42
C	8.84	535.22	109.29	1.83	85.68, 94.32
Si	8.87	539.95	109.32	1.87	85.34, 94.66
Ge	8.91	546.88	109.34	1.99	83.68, 96.32
Sn	8.96	555.16	109.42	2.13	81.96, 98.04
Pb	9.00	560.39	109.49	2.28	80.06, 99.94
Sb	8.99	558.39	109.50	2.21	80.64, 99.37
Te	9.00	560.77	109.47	2.21	80.55, 99.45
I	9.05	560.90	109.91	2.35	75.65, 104.35

Based on the equilibrium volumes, we further optimize the respective crystal structures and geometries. The structural parameters of the most stable In_2O_3 primitive unit cell are tabulated in Table 3-1. The pristine In_2O_3 primitive cell has an equilibrium lattice constant of 8.96 Å, corresponding to a=10.34 Å in the conventional cell, which is larger than the experimental value (10.12 Å) and theoretical value calculated by local density approximation (9.76 Å).[14, 16] As introduced in **Chapter 1**, the *8b* cationic site occupies the

center of trigonally distorted octahedra.[16] The six O-In_{8b} bonds share the equal bond length of 2.22 Å. Compared with pristine indium oxide, the equilibrium cell volume of C-doped In_2O_3 is significantly reduced while the lattice constant and bond length of O-C_{8b} decrease to 8.84 Å and 1.83 Å, respectively. Similar shrinkage is also observed for Si, Ge-doped indium oxide crystal structures. However, Sn-doped In_2O_3 shows the same lattice constant of 8.96 Å and a slightly shorter O-Sn_{8b} bond length (2.13 Å) compared to undoped In_2O_3. The introduction of lead into *8b* position slightly increases the lattice constant, equilibrium cell volume as well as O-Pb_{8b} bond length. Substitutional doping by the fifth period dopant elements (Sb, Te and I) at *8b* site of In_2O_3 crystal slightly increases the equilibrium lattice constants (<1%) and volumes (<1.5%), except that iodine causes a much longer O-M_{8b} bond length. This might be due to their large ionic radii when their valence electrons are not fully taken by the surrounding oxygen atoms in the In_2O_3 matrix (e.g. $r_{Sb^{3+}} = 90\,pm$, $r_{Te^{3+}} = 111\,pm$, $r_{I^{4+}} = 109\,pm > r_{In^{3+}} = 83\,pm$).

3.3.2 The Electronic Structures of Pristine and n-type Doped In_2O_3

The electronic band structure and density of states for pure In_2O_3 have been calculated. As indicated by the band structure in Figure 3-2, indium oxide is a direct band gap semiconductor with the valence band maximum (VBM) and conduction band minimum (CBM) both at Γ point of the Brillouin zone. The band gap is calculated to be 0.9 eV which is much smaller than the experimental value (<2.9 eV).[17-18] This is due to the well-known band-gap underestimation by the density functional theory.[19-20]

The conduction band bottom has shown the parabolic feature of free-electron-like band which is mainly from the *5s* states of indium. The partial

density of states (Figure 3-2) has suggested that the valence band of pure In_2O_3 below Fermi level is primarily contributed by O-*2p* states and partially by In-*5p* states. The empty states of In-*5s* and anti-bonding states of O-*2p* make similar contributions to the conduction band above CBM. The empty In-*5p* states form the band at higher energy. The strong hybridization between the In-*5s* and O-*2p* states gives rise to a three-dimensional transport path for free carriers.[7]

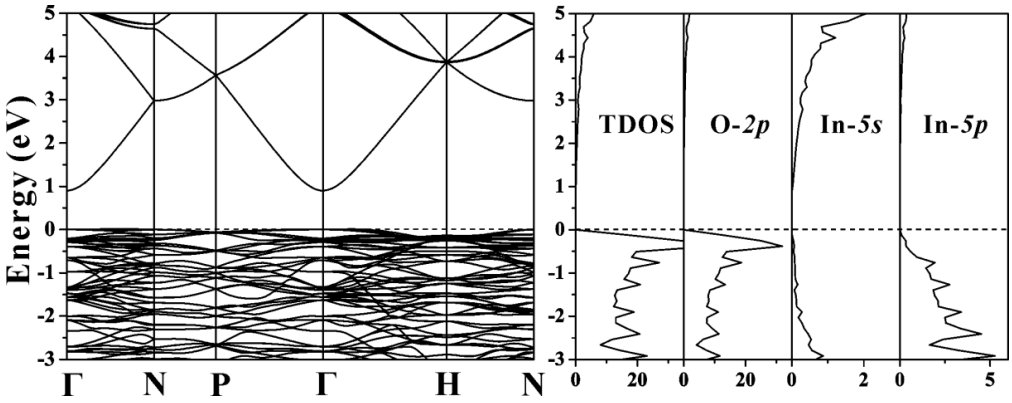

Figure 3-2: The band structure (left) and projected density of states (right) of In_2O_3. E_F is set at 0 eV.

From the band structure of pure In_2O_3, we could see that the band widths are larger than 2 eV along the Γ→H, Γ→N and Γ→P directions within the first Brillouin zone. This suggests a high electron delocalization along the three main crystallographic directions: [001], [011] and [111]. In addition, the high energy dispersion results in a large curvature at the conduction band minimum, implying a small effective mass of electron carriers. The effective mass can be derived by fitting the parabolic conduction band minimum by using Equation 3-1:[21]

$$\frac{1}{m^*} = \frac{1}{\hbar^2}\frac{d^2\varepsilon(k)}{dk^2} \qquad (3\text{-}1)$$

where $\varepsilon(k)$, $\hbar$, and k represent the band dispersion relation, reduced Planck constant and wave vector, respectively.

Table 3-2: The electronic properties of pristine and n-type doped In_2O_3.

Dopants		**In**	**Si**	**Ge**	**Sn**	**C**	**Pb**	**Sb**	**Te**	**I**
Band Gap (eV)	Fund[a]	0.90	0.76	0.79	0.79	0.31	0.53	0.54	0.21	1.28
	Opt[b]	0.90	2.51	2.56	2.56	1.92	1.89	2.21	2.77	1.85
Band Width (eV)	[001]	2.96	2.81	2.88	2.81	2.05	1.57	1.62	1.40	0.35
	[011]	2.08	2.03	2.04	2.03	1.71	1.38	1.41	0.80	0.46
	[111]	2.67	2.54	2.58	2.56	1.97	1.53	1.58	1.37	0.49
Effective Mass (m_0)	[001]	0.20	0.20	0.19	0.19	0.19	0.19	0.18	1.12	0.56
	[011]	0.20	0.20	0.19	0.19	0.19	0.19	0.19	1.14	0.72
	[111]	0.20	0.20	0.19	0.19	0.19	0.20	0.19	0.95	0.59
Electron Velocity at E_F (10^5 m/s)	[001]		8.35	8.58	8.59	6.58	3.95	c	5.81	d
	[011]		8.90	8.98	9.02	5.48	1.82		4.30	
	[111]		8.72	9.03	9.10	6.51	3.61		5.91	

a and b: Fund and Opt refer to the fundamental and optical band gap respectively;
c and d: The Fermi levels do not pass through the conduction band, thus the electron velocities for Sb- and I-doped In_2O_3 are not calculated.

According to Equation 3-1, we obtain an effective mass $m^* = 0.20m_0$ for the pristine In_2O_3 structure (rest electron mass: m_0=9.109×10^{-31} kg). The calculated effective mass is comparable with the experimental value as well as theoretical values.[7, 18, 22] In addition, the effective mass remains highly isotropic along the three main crystallographic directions. All these parameters

suggest that indium oxide is a good host material for transparent conductors. The electronic properties of the undoped In_2O_3 are tabulated in Table 3-2.

The band structures and densities of states for the In_2O_3 doped with group IVA elements are presented from Figure 3-3 to Figure 3-7, respectively. It is clearly shown that the introduction of the IVA dopants significantly shifts Fermi levels up into conduction bands. As a result, all band structures exhibit the metallic like features, implying the improvement of electrical conductivity after the n-type doping of group IVA elements.

Compared with the band structure of pure In_2O_3, the incorporation of extrinsic dopants of Si, Ge and Sn does not significantly change the features of conduction bands (Figure 3-3 to Figure 3-5). A slight decrease in the calculated fundamental band gap is observed, as tabulated in Table 3-2, which can be attributed to the many-body effects.[16] In addition, a pronounced Burstein-Moss (BM) shift is also observed because of the filled states at the bottom of conduction band, as indicated in Figure 3-3. The BM shift (ΔBM) compensates for the renormalization of fundamental band gap to keep the onset of optical absorption at a higher energy level. As a result, the high transparency in the visible range could be maintained.

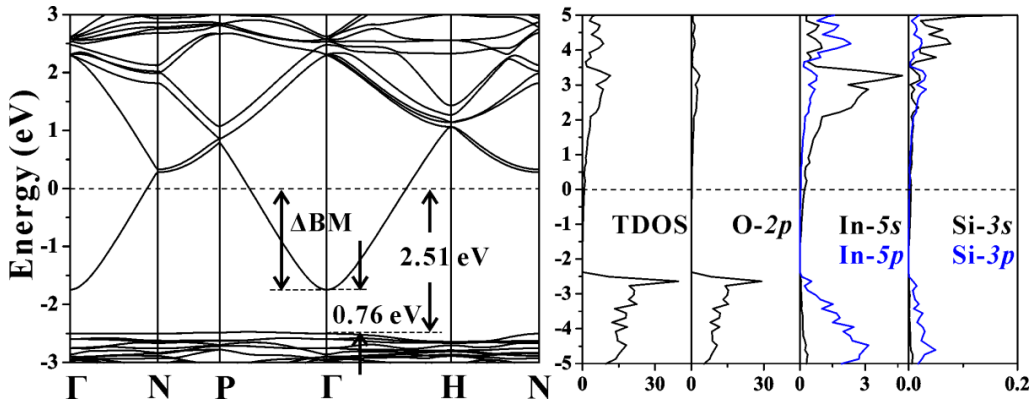

Figure 3-3: The band structure (left) and projected density of states (right) of Si-doped In_2O_3. E_F is set at 0 eV.

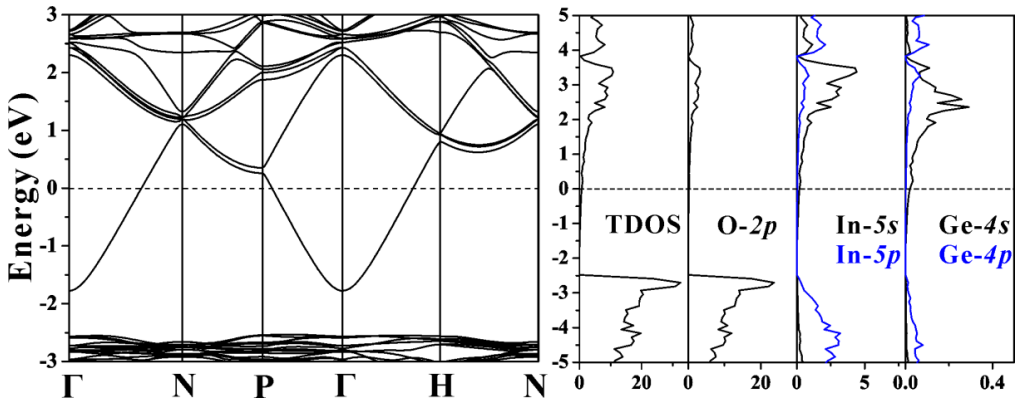

Figure 3-4: The band structure (left) and projected density of states (right) of Ge-doped In_2O_3. E_F is set at 0 eV.

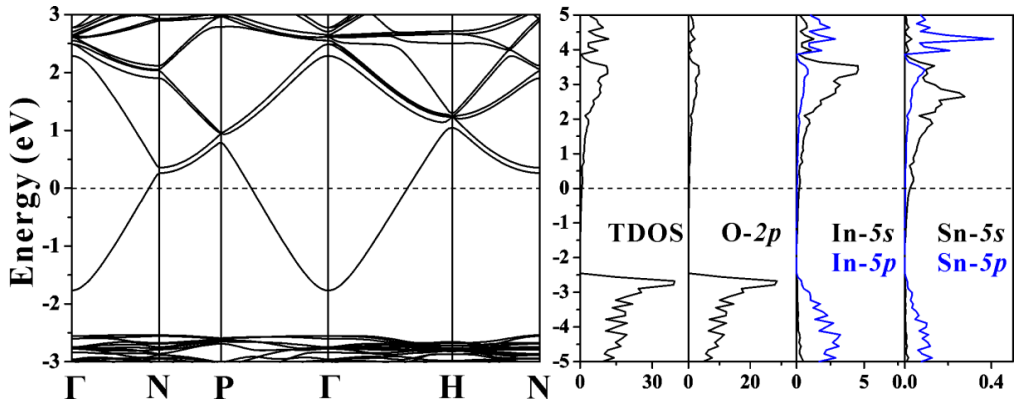

Figure 3-5: The band structure (left) and projected density of states (right) of Sn-doped In_2O_3. E_F is set at 0 eV.

Compared with host In_2O_3, the free-electron-like features of conduction bands are well inherited after the incorporation of three dopants (Si, Ge and Sn). Therefore, a large band width as well as a small effective mass is retained, as listed in Table 3-2. Moreover, the large band width creates a large gradient of the conduction band, which indicates a high electrical conductivity, since conductivity is proportional to the square of electron group velocity at Fermi level.[7] The electron group velocity can be calculated by Equation 3-2:

$$v_k = \frac{1}{\hbar}\frac{d\varepsilon(k)}{dk} \tag{3-2}$$

where $\varepsilon(k)$, $\hbar$, and k represent the band dispersion relation, reduced Planck

constant and wave vector, respectively.[23] Therefore, the electron velocities at Fermi level are calculated to be more than 8.35×10^5 m/s along the three crystallographic directions. It is noted that the electron group velocities show the order of Sn>Ge>Si. Compared with Si- and Ge-doping, the Sn-doped In_2O_3 shows the highest electron velocities of 8.59×10^5 m/s along [001], 9.02×10^5 m/s along [011] and 9.10×10^5 m/s along [111] direction. Therefore, according to the results, we can conclude that Sn is the best of these three dopants. Toshiru et al. prepared the silicon-, germanium- and tin-doped In_2O_3 thin films by radio-frequency magnetron sputtering technique.[2] They found that carrier concentrations showed the sequence of $n_{Si}<n_{Ge}<n_{Sn}$ when dopant concentration was around 6 atom%, while Hall mobility exhibited the inversed sequence due to increased scattering from the ionized impurities. Considering the experimental variations and thin film structures, the electrical conductivities showed good agreement with our computational results.[2]

As shown in Figure 3-3 to Figure 3-5, the densities of states for Si-, Ge- and Sn-doped In_2O_3 display similar features to that of pure indium oxide. According to partial density of states, the valence states are mainly contributed by the O-*2p* and In-*5p* states. The conduction band minima are formed by the anti-bonding O-*2p*, In-*5s* as well as the *s* states from other group IVA dopants. Furthermore, we can observe the good hybridizations of dopant's *s* states with anion's orbitals, as there is no appreciable localization of the states from extrinsic impurities near CBM and Fermi level. The good hybridization between the dopant's *s* states and anti-bonding O-*2p* states implies a high overlapping of cation's *s* orbitals and anion's *2p* orbitals, which provides a good carrier transport network.[7] The densities of states show a good agreeme-

nt with the features of corresponding band structures.

The band structures and densities of states for carbon- and lead-doped In_2O_3 are presented in Figure 3-6 and 3-7, respectively. Obviously, the band structures also show metallic features after the doping by carbon and lead as Fermi levels cross conduction bands. In addition, conduction band minima exhibit the free-electron-like parabolic features.

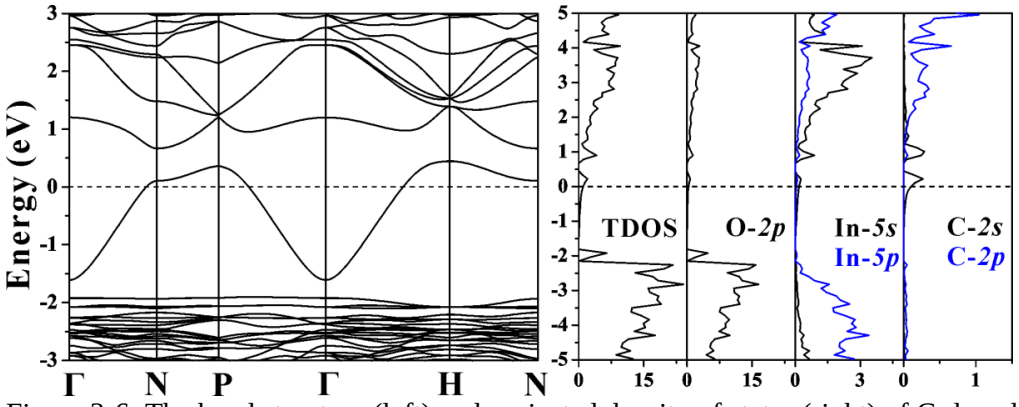

Figure 3-6: The band structure (left) and projected density of states (right) of C-doped In_2O_3. E_F is set at 0 eV.

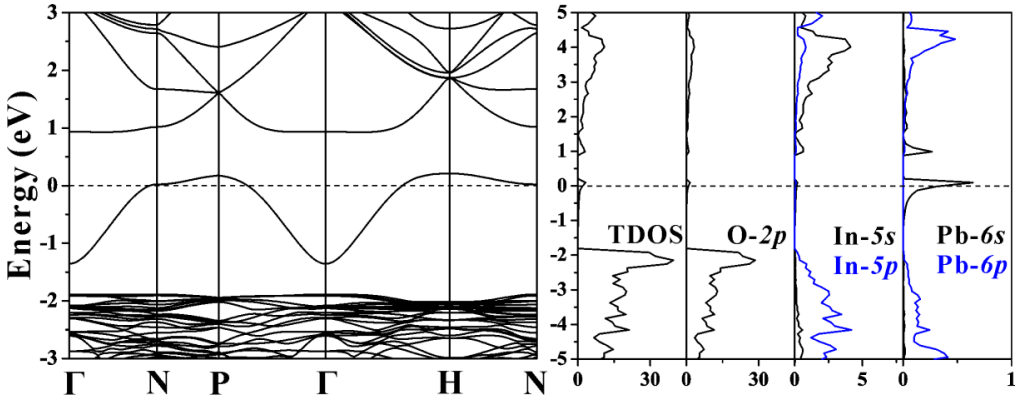

Figure 3-7: The band structure (left) and projected density of states (right) of Pb-doped In_2O_3. E_F is set at 0 eV.

Compared to previous three doping cases, the fundamental band gaps of C- and Pb-doped In_2O_3 are remarkably reduced and the Burstein Moss shifts are less pronounced, as listed in Table 3-2. Although effective masses remain unchanged, the significant decrease of conduction band widths dramatically

lowers the electron group velocities near Fermi level (Table 3-2). Most importantly, a second band gap above Fermi level can be observed. This is due to the weak hybridization of the states from C-*2s* and Pb-*6s* with the O-*2p* anti-bonding states, as indicated by the densities of states. The weak overlapping between dopants' *s* orbitals and oxygen *2p* orbitals gives rise to the relatively localized states near Fermi level, which flatten conduction bands and cause poor electronic properties.[7]

The electronic structures of Sb-, Te- and I-doped In_2O_3 have also been studied. The corresponding band structure and density of states are presented in Figure 3-8 to 3-10, respectively. It is obvious that a second band gap appear

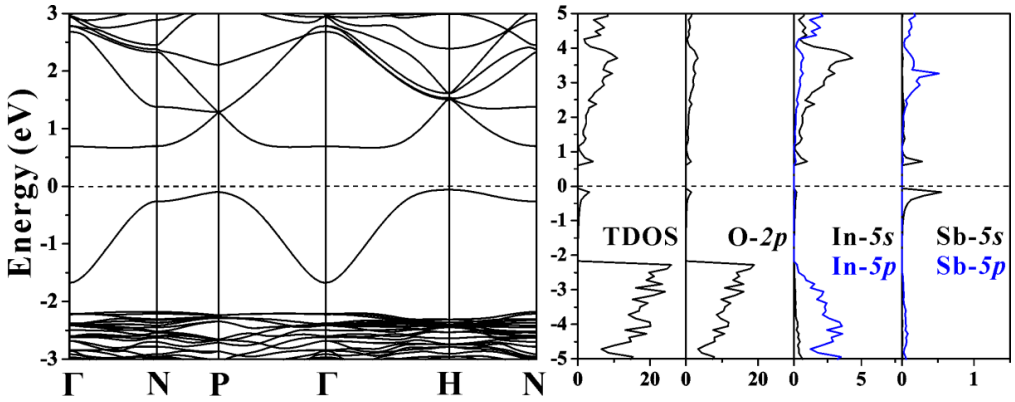

Figure 3-8: The band structure (left) and projected density of states (right) of Sb-doped In_2O_3. E_F is set at 0 eV.

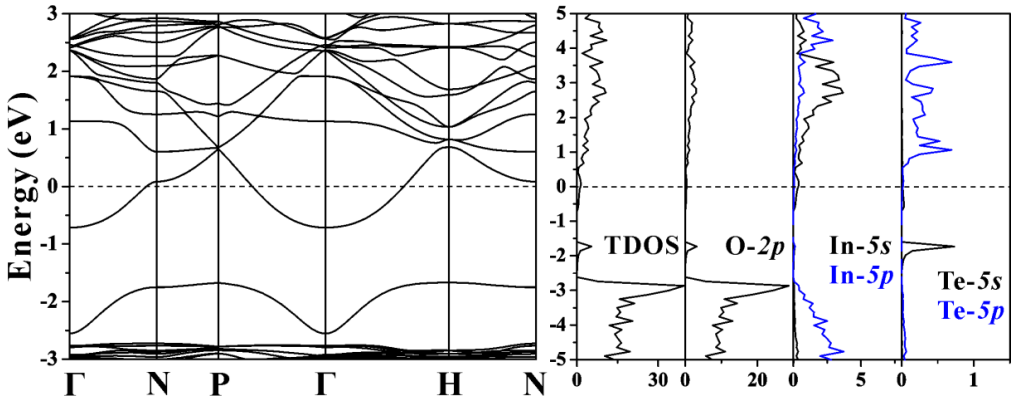

Figure 3-9: The band structure (left) and projected density of states (right) of Te-doped In_2O_3. E_F is set at 0 eV.

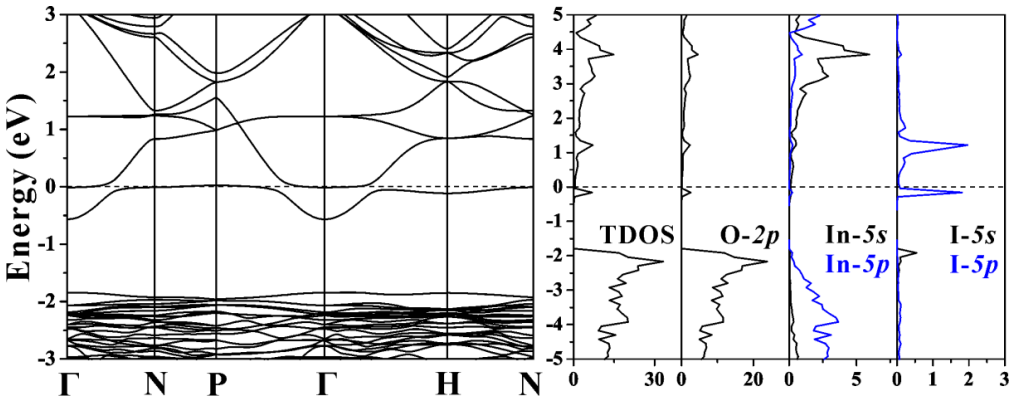

Figure 3-10: The band structure (left) and projected density of states (right) of I-doped In_2O_3. E_F is set at 0 eV.

above fundamental band gap after the substitutional doping of antimony, tellurium and iodine. The conduction bands are remarkably changed compared with that of In_2O_3 host. According to their partial densities of states (Figure 3-8 to 3-10), the variations are resulted from the weak overlapping between dopants' orbitals and anion's orbitals. The weak hybridization leads to the relatively localized states near Fermi levels. As a result, after incorporation of the three fifth period dopants, the conduction band widths are remarkably narrowed. The effective masses, especially for Te- and I-doped In_2O_3, are dramatically increased.

3.3.3 Atomic Orbitals, Bader Charge Analysis and Charge Density Differences

In the previous section, we have investigated the electronic structures of pure and n-type doped In_2O_3. The electronic properties indicate that Si, Ge and Sn are three effective n-type dopants, with Sn as the best. In contrast, other extrinsic dopants, including C, Pb, Sb, Te and I, are ineffective as they create localized states near Fermi levels, which deteriorate the effective mass and electron velocity.

To further understand the reason behind the difference, we have calculated

the neutral atomic orbital energy levels. The atomic orbital energies have been calculated by the full electrons method, using DMol^3 package[24-25] with the exchange-correlation potential incorporated in the generalized gradient approximation (GGA) using the Perdew-Burke-Ernzerhof functional (PBE).[12]

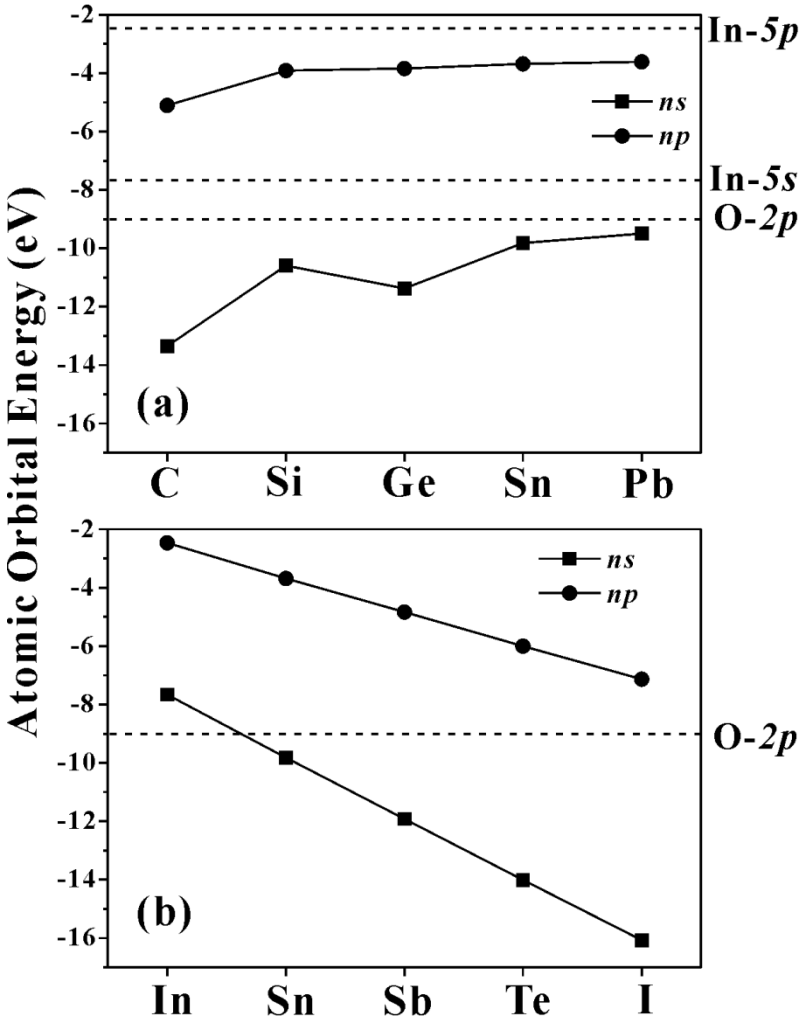

Figure 3-11: The calculated atomic orbital energies for the valence electrons of the dopant and host atoms.

The calculated atomic orbital energy levels are shown in Figure 3-11. As can be seen in Figure 3-11a, group IVA elements have *np* valence electrons at the energy levels close to that of In-*5p* electrons, except a slightly lower C-*2p* orbitals. Their *ns* valence orbitals have the energy levels close to those of O-*2p* and In-*5s* electrons, except remarkably low-lying C-*2s* orbitals. The close

orbital energy levels may suggest a good overlapping between O-*2p* orbitals and In-*5s* orbitals which mainly contribute to the conduction band minimum of host In_2O_3, as discussed in the previous section. A good orbital overlapping of O-*2p* orbitals with group IVA-*ns* valence orbitals is expected as well, except C-*2s*. As discussed in the previous section, the electronic structures have indeed shown a weak hybridization in C-doped In_2O_3 and strong hybridizations for Si-, Ge- and Sn-doped In_2O_3. However, lead is an exception, as suggested by the electronic structures of Pb-doped In_2O_3 (Figure 3-7), although its *6s* orbital energy is close to that of O-*2p* orbital.

The valence orbital energies of the fifth period element (Sn, Sb, Te and I) are shown in Figure 3-11b. As can be seen, the energy difference between O-*2p* orbitals and Sn-*5s* orbitals is about 0.8 eV, while the difference is larger than 2.9 eV for the *5s* orbital of Sb, Te and I. Therefore, a weak orbital overlapping might be expected between the O-*2p* orbital and the *5s* orbitals of Sb, Te and I. This is consistent with the electronic structures of Sb-, Te- and I-doped In_2O_3 (Figure 3-8 to 3-10).

Table 3-3: The Bader charges of the dopants and six nearest oxygen atoms. M_{8b} refers to the dopant atom at 8b cationic position.

Dopants	**In**	**C**	**Si**	**Ge**	**Sn**	**Pb**	**Sb**	**Te**	**I**
M_{8b}	+1.62	+0.94	+2.98	+2.11	+2.17	+1.59	+2.06	+2.15	+1.43
O	-1.08	-0.90	-1.24	-1.10	-1.11	-1.04	-1.10	-1.10	-1.03

We have calculated the Bader charges[26-28] for further analysis and the results are listed in Table 3-3. For In_2O_3 host, the In atom at *8b* site (In_{8b}) loses 1.62 electrons/atom. The In atoms at *24d* position show the similar Bader

charge to In_{8b} (data not shown). The six oxygen atoms nearest to In_{8b}, as well as the other oxygen atoms gain 1.08 electrons/atom. This suggests a good orbital overlapping between cations and anions, which facilitates a uniform charge distribution.

After the doping of group IVA elements, the net charges of O and M_{8b} vary significantly. As shown in Table 3-3, the carbon dopant only loses 0.94 valence electrons. Correspondingly, the six oxygen atoms near carbon gain less charges than oxygens in host In_2O_3 (0.9 vs. 1.08 electrons/atom). This indicates that the charge is highly localized around carbon dopant atom. The result is in good consistent with the electronic structures of C-doped In_2O_3.

In contrast, Si, Ge and Sn atoms lose much more valence electrons than that of In_{8b}. Hence, electrons gained by the six nearest oxygen atoms in these three doping structures are more than that in pure In_2O_3. These results indicate a better overlapping of dopants' orbitals with neighboring anion's orbitals.[7] Hence the charges are more uniformly distributed for Si-, Ge- and Sn-doped In_2O_3, implying the high effectiveness of n-type doping from these three extrinsic dopants.

Pb has four valence electrons, but it only loses 1.59 electrons/atom. Therefore, the electrons are highly localized near Pb atom. Although the six oxygen atoms near the dopant gain slightly more/less electrons, the localization of charges around dopants is even more remarkable for Sb-, Te- and especially I-doped In_2O_3. Therefore, it is implied that Pb, Sb, Te and I might be not effective n-type dopants for In_2O_3 as transparent conductors.

The charge density differences have been calculated to understand the interaction between dopant atoms and host material. It is calculated by

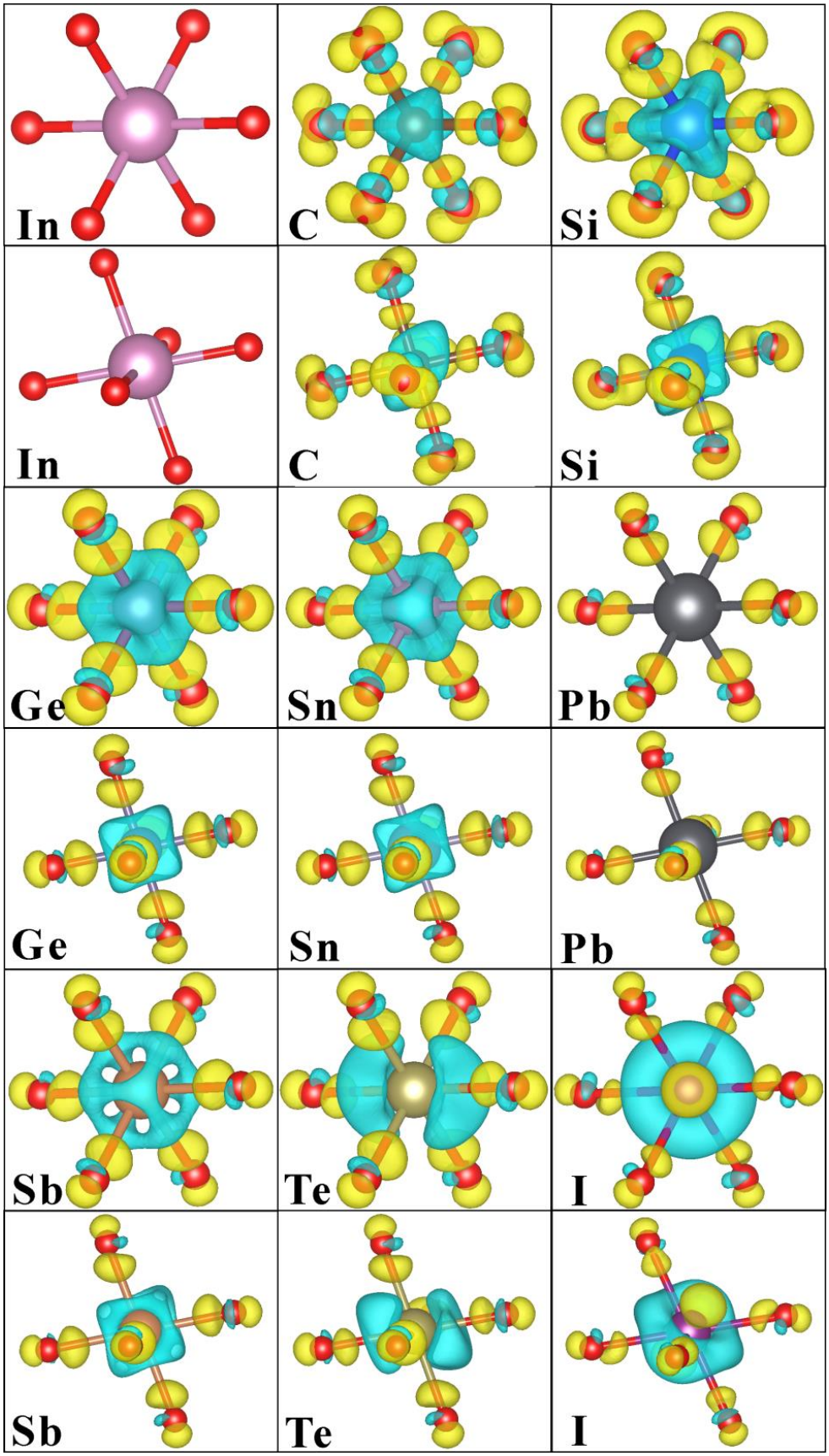

Figure 3-12: The charge density differences for n-type doped In_2O_3. Yellow and blue regions indicate gain and loss of charges (isosurface: ±0.01 e/Å3). Only atoms near the dopant are shown.

Equation 3-3:[29]

$$\Delta\rho = \rho(\text{Total}) - \rho(M_{8b}) - \rho(\text{Host}_{vac}) \quad (3\text{-}3)$$

where ρ(Total), $\rho(M_{8b})$ and $\rho(\text{Host}_{vac})$ refer to the total charge density of doped In_2O_3, charge density of the dopants, and charge density of host In_2O_3 with *8b* vacancy which is formed by removing the dopant from the doped structure.

The charge density differences of the doped In_2O_3 are shown in Figure 3-12 with each structure viewed along two different directions. The electrons are found to be localized around the dopant atoms of Pb, Sb, and especially highly localized around C, Te and I, whereas the charges are uniformly distributed for Si-, Ge- and Sn-doped In_2O_3. The general trend is consistent with the Bader charge analysis.

3.3.4 Formation Energies and Transition Levels

Under thermodynamic equilibrium conditions, the concentration of substitutional defects in a lattice is proportional to $e^{-\Delta E/kT}$, where ΔE, *k* and T refer to the formation energy of defect, Boltzmann constant and temperature, respectively.[30] The formation energies of extrinsic impurities imply their existence in host materials. Therefore, it is important to investigate the formation energies of various extrinsic dopants. The formation energy, $\Delta E(M_{In}^q)$, is calculated by Equation 3-4:[31-32]

$$\Delta E(M_{In}^q) = E_{tot}(M_{In}^q) - E_{tot}(In_2O_3) - \mu(M)_{solid} + \mu(In)_{solid} - \mu(M) + \mu(In) + q(E_F + VBM) \quad (3\text{-}4)$$

Here $E_{tot}(M_{In}^q)$ and $E_{tot}(In_2O_3)$ correspond to the total energy of In_2O_3 unit cell substitutionally doped with M with charge q and the total energy of pure In_2O_3 unit cell, respectively. $\mu(M)_{solid}$ and $\mu(In)_{solid}$ are the chemical potentials of dopant and host element in the solid form. μ(M) and μ(In) refer to the chemical potentials of M and In in reference to $\mu(M)_{solid}$ and $\mu(In)_{solid}$,

respectively. E_F and VBM are the energies of Fermi level and valence band maximum, respectively. The chemical potentials of pure elements are obtained from their corresponding solid crystals. μ(O) is half the total energy of an isolated O_2 molecule in a large cubic unit cell (a= 15 Å).

Under equilibrium conditions, the chemical potentials of host atoms, In and O, must meet the requirement: $2\mu(In)+3\mu(O)=\Delta H_f(In_2O_3)$. The formation enthalpy of bixbyite In_2O_3 is obtained by: $\Delta H_f(In_2O_3)=E_{tot}(In_2O_3)-\mu(In)_{solid}-\mu(O_2)_{gas}/2$. The chemical potentials of indium and oxygen are related to the experimental conditions. Under the extreme oxygen-rich condition, μ(O) equals to zero. At the other extreme condition, μ(In) is zero. Therefore, in real experimental condition, μ(O) and μ(In) can only vary in the ranges: $\Delta H_f(In_2O_3)/2 \leq \mu(In) \leq 0$ and $\Delta H_f(In_2O_3)/3 \leq \mu(O) \leq 0$.

As indicated by Equation 3-4, the formation energy for charged defects relies on the energy of Fermi level. The transition level, ε(+1/0), is defined as the energy of E_F for which the dopant at two charged states (q=+1 and q=0) has the same formation energy. Therefore, transition levels reflect the energy levels of a defect (e.g., shallow or deep) with respect to the conduction band minimum or valence band maximum.

In order to prevent possible oxide impurities formed between dopant and oxygen under real experimental conditions, the chemical potentials, μ(M) and μ(O), should be correlated by: $m\mu(M) + n\mu(O) \leq \Delta H_f(M_mO_n)$, where $\Delta H_f(M_mO_n)$ is the formation enthalpy of possible oxide impurities. The calculated formation enthalpies of host In_2O_3 structure and possible impurities are tabulated in Table 3-4. Given that the temperature dependence has not been included, the formation enthalpies are in good consistence with

experimental values.

The formation energy of carbon defect is extremely high (>7.5 eV) at both O-rich and In-rich conditions, which implies less possibility of the neutral as well as the +1 charged state carbon occupying indium *8b* site. In contrast, the substitutional doping of carbon at the oxygen site is possible.[41]

Table 3-4: The formation enthalpy of host material and possible secondary phases.

Phases	**Formation Enthalpy ΔH_f (eV)**	
	Calculated	**Experimental[33]**
In_2O_3 (cubic)[15]	-9.52	-9.60
CO_2 (gas)	-4.78	-4.08
α-SiO_2 (trigonal)[34]	-9.34	-9.44
GeO_2 (trigonal)[35]	-5.57	-6.01
SnO_2 (tetragonal)[36]	-6.03	-5.99
β-PbO_2 (tetragonal)[37]	-3.55	-2.88
Sb_2O_5 (monoclinic)[38]	-11.18	-10.07
TeO_2 (tetragonal)[39]	-4.01	-3.34
I_2O_5 (monoclinic)[40]	-4.91	

The calculated formation energies of other substitutional defects under two extreme conditions, the oxygen rich or indium rich, are shown in Figure 3-13. The Fermi level ranges from the valence band minimum at 0 eV to conduction band minimum at 2.7 eV which is the experimental band gap of bulk In_2O_3.[18] Under oxygen-rich condition, the formation energies of neutral substitutional

defects of Sb, Te, I and Si are moderately high (>1.75 eV), whereas the formations of substitutional Ge, Sn and Pb should be more feasible.

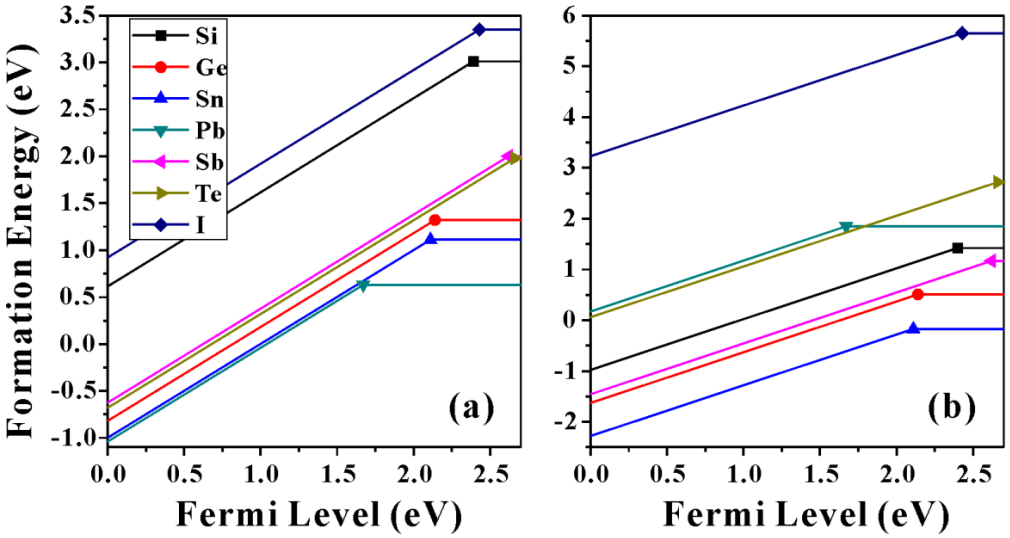

Figure 3-13: The formation energies of the substitutional defects at different conditions: (a) O-rich and (b) In-rich. The transition levels are marked in solid symbols.

At indium-rich conditions, the formation energies of neutral defects are generally enhanced compared with those under oxygen-rich circumstances. For example, the formation energy of neutral iodine is significantly increased by almost 70% to 5.65 eV. A significant increase of formation energies for the neutral Pb and Te is also observed. In contrast, the formation energies for neutral dopants of Si, Ge, Sn and Sb are reduced, suggesting that the existence of these neutral dopants is more possible under In-rich condition. It should be noted that under either O-rich or In-rich condition the formation energies of neutral Ge and Sn are both fairly low (<1.1 eV). This indicates that the two elements are relatively easy to be doped into the *8b* position of In_2O_3 lattice.[32] Especially for Sn dopant, the formation of both the neutral and +1 charged state defects is spontaneous under In-rich condition. Given the oxygen-poor environment during the deposition or post annealing of TCO films in the real

experimental condition, Sn might be the most easily doped element for indium oxide.

The transition levels of different dopant elements are presented in Figure 3-14. It is clear that all the dopants are donors since their transition levels of ε(+1/0) are close to the conduction band minimum. Si, Sb, Te and I are especially shallow donors for which the ionization energies are less than 0.6 eV. C, Ge and Sn are slightly deeper donors while lead is a deep donor with the ionization energy more than 1 eV.

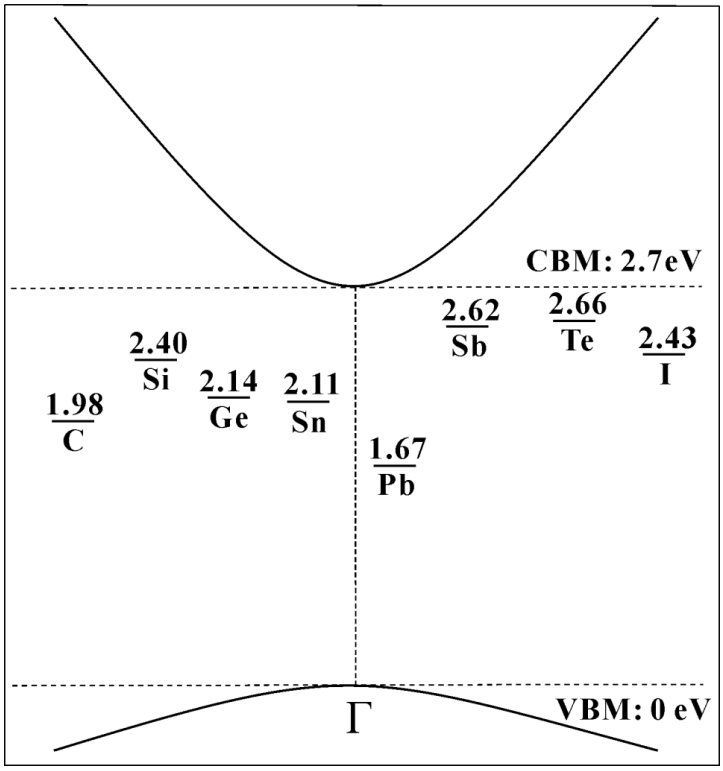

Figure 3-14: The calculated transition levels, ε(+1/0), for different substitutional dopants. The energies are given with respect to VBM.

According to the formation energies and transition levels discussed above, we could see that Si, Ge and Sn are three effective dopants with not only fairly low formation energies but also reasonably shallow defect levels. The other dopants have either high ionization energies or less abundance due to the large formation energies.[42] The results well explain the conclusion drawn from the

electronic band structures and densities of states that Si-, Ge- and Sn-doped In_2O_3 show good electronic and transport properties.

3.4 Conclusion

In summary, we have simulated the geometrical and electronic structures of n-type In_2O_3 doped with the group IVA and fifth period elements (Sb, Te and I). The conclusion has been drawn as follows:

(1) The optimized geometries indicate that the substitutional incorporation of smaller dopants causes a shrink of crystal volumes and a shortening of the M-O bonds, while the substitutional replacement of In_{8b} by the larger-size dopant expands the unit cell.

(2) The electronic structures reveal that the *n*s states of Si, Ge and Sn, are strongly hybridized with the O-*2p* states. Compared with other dopant elements, the three dopants do not alter the conduction band features of the host In_2O_3. Therefore, a low effective mass ($0.2m_0$) and a high electron group velocity ($>8.3\times10^5$ m/s) near the Fermi level can be achieved.

(3) The atomic valence orbitals of Si, Ge and Sn have energies close to that of O-*2p* orbital. The Bader charge analysis and electron density differences show that the electrons can be more effectively delocalized in Si-, Ge- and Sn-doped In_2O_3 lattice.

(4) The low formation energies imply the larger abundance of both the neutral and +1 charged state Ge and Sn dopant atoms under both oxygen-rich and indium-rich conditions. Si and Sb only more possibly exist under the indium-rich condition. Given the real oxygen-poor condition, Sn might be the most preferred dopant. Considering the superior electronic and

transport properties, it is understandable that Sn-doped indium oxide is the most widely used In_2O_3-based TCO film.

References

1. Gassenbauer, Y.; Schafranek, R.; Klein, A., et al., *Phys. Rev. B* **2006,** *73*, 245312.
2. Maruyama, T.; Tago, T., *Appl. Phys. Lett.* **1994,** *64*, 1395-1397.
3. Gordon, R. G., *MRS Bull.* **2000,** *25*, 52-57.
4. Minami, T., *Thin Solid Films* **2008,** *516*, 5822-5828.
5. Pasquarelli, R. M.; Ginley, D. S.; O'Hayre, R., *Chem. Soc. Rev.* **2011,** *40*, 5406-5441.
6. Liu, H.; Avrutin, V.; Izyumskaya, N., et al., *Superlattice Microst.* **2010,** *48*, 458-484.
7. Medvedeva, J. E.; Hettiarachchi, C. L., *Phys. Rev. B* **2010,** *81*, 125116.
8. Kresse, G.; Furthmuller, J., *Comput. Mater. Sci.* **1996,** *6*, 15-50.
9. Kresse, G.; Furthmuller, J., *Phys. Rev. B* **1996,** *54*, 11169-11186.
10. Blochl, P. E., *Phys. Rev. B* **1994,** *50*, 17953-17979.
11. Kresse, G.; Joubert, D., *Phys. Rev. B* **1999,** *59*, 1758-1775.
12. Perdew, J. P.; Burke, K.; Ernzerhof, M., *Phys. Rev. Lett.* **1996,** *77*, 3865-3868.
13. Monkhorst, H. J.; Pack, J. D., *Phys. Rev. B* **1976,** *13*, 5188-5192.
14. Nadaud, N.; Lequeux, N.; Nanot, M., et al., *J. Solid State Chem.* **1998,** *135*, 140-148.
15. Fuchs, F.; Bechstedt, F., *Phys. Rev. B* **2008,** *77*, 155107.
16. Mryasov, O. N.; Freeman, A. J., *Phys. Rev. B* **2001,** *64*, 233111.

17. Weiher, R. L.; Ley, R. P., *J. Appl. Phys.* **1966,** *37*, 299-302.

18. Scherer, V.; Janowitz, C.; Krapf, A., et al., *Appl. Phys. Lett.* **2012,** *100*, 212108.

19. Seidl, A.; Gorling, A.; Vogl, P., et al., *Phys. Rev. B,* **1996,** *53*, 3764-3774.

20. Machado-Charry, E.; Canadell, E.; Segura, A., *Phys. Rev. B* **2007,** *75*, 045206.

21. Lange, B.; Freysoldt, C.; Neugebauer, J., *Phys. Rev. B* **2010,** *81*, 224109.

22. Preissler, N.; Bierwagen, O.; Ramu, A. T., et al., *Phys. Rev. B* **2013,** *88*, 085305.

23. Grundmann, M., *The Physics of Semiconductors*, Springer Berlin Heidelberg, **2010**, 139-183.

24. Delley, B., *J. Chem. Phys.* **1990,** *92*, 508-517.

25. Delley, B., *J. Chem. Phys.* **2000,** *113*, 7756-7764.

26. Tang, W.; Sanville, E.; Henkelman, G., *J. Physics-Condens. Mat.* **2009,** *21*, 084204.

27. Sanville, E.; Kenny, S. D.; Smith, R., et al., *J. Comput. Chem.* **2007,** *28*, 899-908.

28. Henkelman, G.; Arnaldsson, A.; Jónsson, H., *Comput. Mater. Sci.* **2006,** *36*, 354-360.

29. Ma, D.; Yang, Z., *New J. Phys.* **2011,** *13*, 123018.

30. Van de Walle, C. G., *J. Appl. Phys.* **2004,** *95*, 3851-3879.

31. Zhang, S.; Northrup, J., *Phys. Rev. Lett.* **1991,** *67*, 2339-2342.

32. Han, D.; West, D.; Li, X.-B., et al., *Phys. Rev. B* **2010,** *82*, 155132.

33. Lide, D. R., *Handbook of Chemistry and Physics*, **2009**, 5-4 – 5-32.

34. Wright, A. F.; Lehmann, M. S., *J. Solid State Chem.* **1981,** *36*, 371-380.

35. Yamanaka, T.; Ogata, K., *J. Appl. Crystallogr.* **1991,** *24*, 111-118.

36. Bolzan, A. A.; Fong, C.; Kennedy, B. J., et al., *Acta Crystallogr. Sect. B* **1997,** *53*, 373-380.

37. Dantonio, P.; Santoro, A., *Acta Crystallogr. Sect. B* **1980,** *36*, 2394-2397.

38. Jansen, M., *Acta Crystallogr. B* **1979,** *35*, 539-542.

39. Worlton, T. G.; Beyerlein, R. A., *Phys. Rev. B* **1975,** *12*, 1899-1907.

40. Wu, Z. Q.; Kalia, R. K.; Nakano, A., et al., *J. Chem. Phys.* **2011,** *134*, 204501.

41. Green, R. J.; Boukhvalov, D. W.; Kurmaev, E. Z., et al., *Phys. Rev. B* **2012,** *86*, 115212.

Chapter 4

Geometrical Structures, Electronic and Transport Properties of a Novel Two-Dimensional GaS Transparent Conductor

4.1 Introduction

In **Chapter 1**, we have briefly reviewed one non-oxide based transparent conducting material—graphene. It has shown good properties as a transparent conductor (e.g. R_s~100 Ω, T~90%).[1-3] Considering the high bendability, it is very promising for flexible electronics, for example, touch screens and curved OLED displays, especially when a large-scale (~600 $inch^2$) deposition and roll-to-roll processing became possible.[4]

Recently, graphene analogs, such as MoS_2, WSe_2, WS_2, GaS, TiS_2 etc., have attracted great attentions.[5-7] Hexagonal GaS, as one of graphene analogs, is an important III-VI semiconductor, showing promising applications in the near-blue light-emitting device,[8] field emission device,[9] and photodetector.[10] It exists in several phases, including β-GaS, GaS-II and the metastable cubic phases (zinc blend, rock-salt) initially reported by McInnes et al.[11] Hexagonal β-GaS is the most stable phase under ambient conditions, with a direct band gap of 3.05 eV and indirect band gap of 2.5 eV.[12]

As shown in Figure 4-1, its single unit cell consists of four gallium and four sulfur atoms, forming two layers of [S-Ga-Ga-S] units. Within the layer, the interaction is predominantly strong covalent bonding from Ga-S and Ga-Ga.

The two layers stack together along c-axis via a weak Van der Waals force between S atoms. This anisotropic feature facilitates the exfoliation of bulk GaS into ultrathin two-dimensional (2-D) nanosheets, insertion of lithium and other ions into the layers and formation of GaS nanotube.[13]

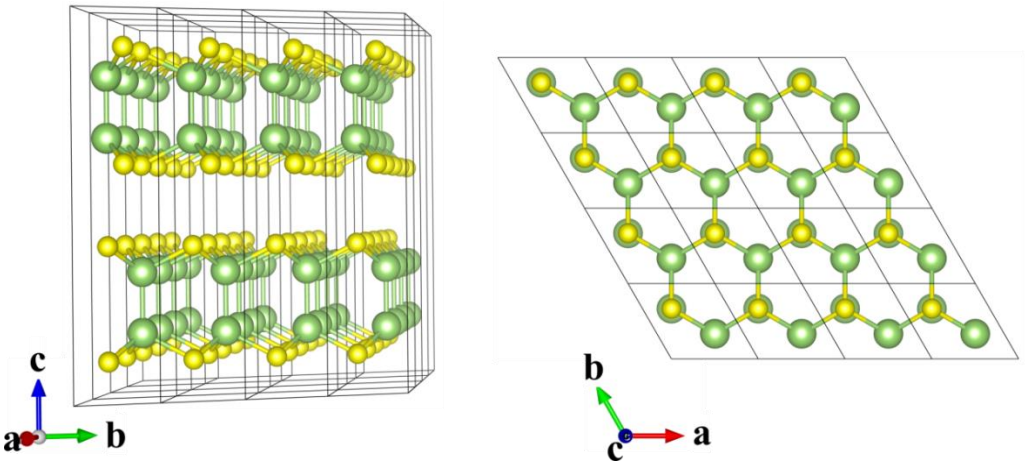

Figure 4-1: The optimized structure of bulk β-GaS unit cell viewed along a-axis (left) and c-axis (right).

Up to date, no experimental or theoretical works have been contributed to explore 2-D β-GaS as the transparent conductor. In this Chapter, we use the density-functional theory to investigate the geometrical and electronic structures of 2-D GaS sheet with a simple doping from the hydrogenation of sulfur atoms. The H-doping significantly shifts the Fermi level of GaS into the conduction band. The electronic and transport properties imply a promising application of the H-doped 2-D GaS as a transparent conductor.

4.2 Computational Details

The calculations were performed with density functional theory (DFT)[14-15] as implemented in the code VASP[16-17] with the electron-ion interactions described by the projector augmented wave (PAW) method.[18-19] The exchange-correlation potential was incorporated in the generalized gradient approximation (GGA) using the Perdew-Burke-Ernzerhof functional (PBE).[20]

A cutoff energy of 500 eV was sufficient to converge the total energy. The Brillouin zones were sampled within a 39×39×1 Monkhorst-Pack[21] *k*-point mesh for 2-D GaS sheet and 39×39×9 for the bulk. All the geometrical structures were fully relaxed until the total energies were converged to 10^{-5} eV and the total forces less than 0.01 eV/Å on each atom.

The optimization of bulk GaS was started from an experimentally reported hexagonal structure (a=3.58 Å, c=15.53 Å, space group: $P6_3/mmc$), considering the Van der Waals interactions by the DFT-D2 approach.[22] For the 2-D sheet simulation, one layer of [S-Ga-Ga-S] was removed from the bulk before significantly increasing the length of c to prevent artificial interactions between slabs (c=25 Å results in an empty space about 20 Å along z-axis).

For the simulation of different layers GaS, an empty space of at least 12 Å was applied. The doping of 2-D GaS sheet was achieved by attaching the topmost sulfur with one hydrogen atom. (1×1×1), (2×2×1), (3×3×1) and (4×4×1) supercells of 2-D GaS structure were used to simulate the different doping concentrations. The carrier transport properties were performed by using the code BoltzTrap which has been widely used to predict the transport property of various materials.[7, 23]

4.3 Results and Discussion

4.3.1 The Geometrical Structures of Bulk, Pure and H-doped 2-D GaS

The bulk β-GaS shows a hexagonal crystal structure with a space group of $P6_3/mmc$. For the bulk model, both atomic positions and parameters of the unit cell were optimized. After optimization, the cell parameters (a=3.58 Å, c=15.55 Å, $\alpha=\beta=90^o$, $\gamma=120^o$) remain close to the experimental values.[24] The

calculated bond lengths of Ga-Ga and Ga-S maintain the experimental values as well (2.44 Å and 2.35 Å, respectively). The bond lengths are slightly larger than those calculated by local density approximation (LDA) method due to the well-known over-binding of LDA.[5, 25] The bond lengths and bond angles remain almost intact compared to the starting parameters. The optimized structural parameters are listed in Table 4-1. For the clarity of elucidation, one repeating unit of [S-Ga-Ga-S] is also shown with the labeling of the four atoms. In the bulk unit cell, two [S-Ga-Ga-S] repeating units stack along z-axis by a weak interaction of Van der Waal force. Here the two units are found to share same geometrical parameters after fully structural optimization.

Table 4-1: The optimized geometrical parameters of different structures.

	H-S_1 (Å)	Ga_1-S_1 (Å)	Ga_2-S_2 (Å)	Ga_1-Ga_2 (Å)	Bond Angle (°) S_1-Ga_1-Ga_2	Bond Angle (°) Ga_1-Ga_2-S_2
Bulk		2.35	2.35	2.44	118.14	118.14
2-D		2.35	2.35	2.48	118.40	118.40
111-H	1.41	2.50	2.35	2.45	124.23	118.30
221-H	1.36	2.54	2.36	2.45	103.15	126.27
331-H	1.41	2.49	2.36	2.47	118.51	118.36
441-H	1.42	2.49	2.36	2.47	119.64	118.03

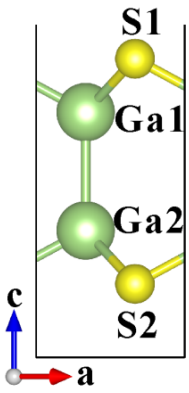

The 2-D model is built from the bulk by removing one repeating unit of [S-Ga-Ga-S] and increasing the lattice parameter of c to a sufficiently large value of 25 Å to prevent the artificial interaction between slabs. As shown in Table 4-1, the optimized lengths of two Ga-S bonds remain same as the bulk structure. However, the bond length of Ga_1-Ga_2 increases by 1.6% to 2.48 Å compared to the bulk value, while the two bond angles expand slightly.

Figure 4.2 shows the optimized pure 2-D GaS structure viewed along a-axis and c-axis respectively. Compared with the bulk, the symmetry of 2-D structure is reduced to D_{3h}. The distance between S_1 and S_2 is slightly more than 4.71 Å. Given the atomic size of sulfur (~100 pm), the calculated thickness of 2-D single-layer β-GaS is about 0.67 nm, in reasonable consistence with the thickness (0.75 nm) obtained by atomic force microscopy.[10]

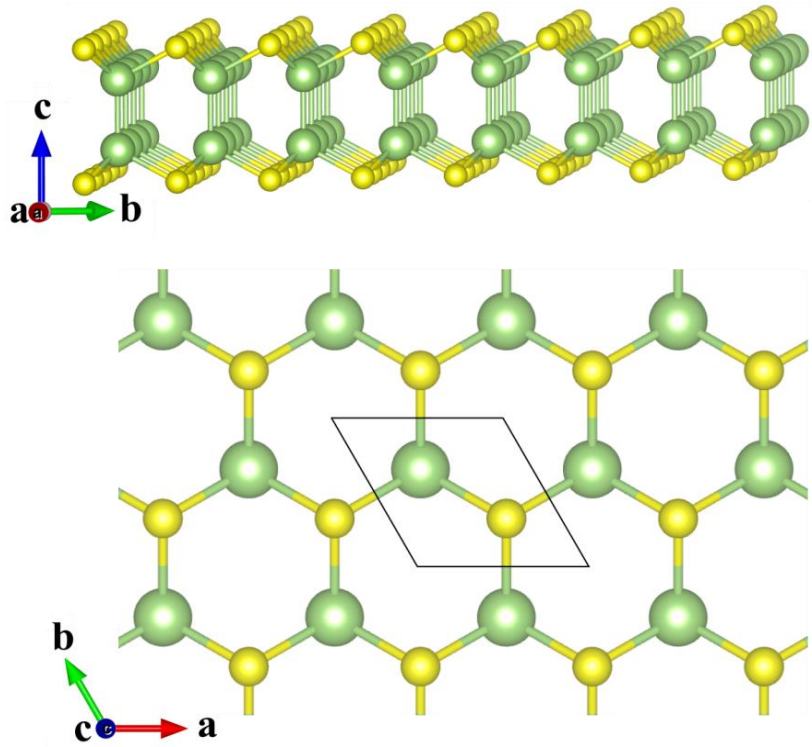

Figure 4-2: The optimized 2-D GaS structure. Black lines outline a single unit cell.

The effective doping of 2-D GaS was achieved by hydrogenation of the topmost sulfur atom (S_1). Four different supercells ((1×1×1), (2×2×1), (3×3×1) and (4×4×1)), each doped with one H atom, were used to simulate the different doping concentrations, which result in a theoretical carrier concentration of 8.98×10^{14} cm^{-2}, 2.25×10^{14} cm^{-2}, 9.98×10^{13} cm^{-2} and 5.62×10^{13} cm^{-2}, respectively.

The relaxed structure of H-doped (1×1×1) supercell is presented in Figure 4-3. After geometrical optimization, the S-H bond length is found to be 1.41 Å, indicating a chemical bonding. Due to the introduction of hydrogen, the bond length of Ga_1-S_1 increases significantly from 2.35 Å to 2.50 Å, while the lengths of Ga_2-S_2 (2.36 Å) and Ga_1-Ga_2 (2.45 Å) remain close to these of the single-layer structure. The increase of the S_1-Ga_1-Ga_2 bond angle expands the S_1-S_2 distance by 5.5%. After full relaxation, the point group is found to be C_{3v} since the horizontal reflection plane is broken due to the addition of hydrogen to the top sulfur atom.

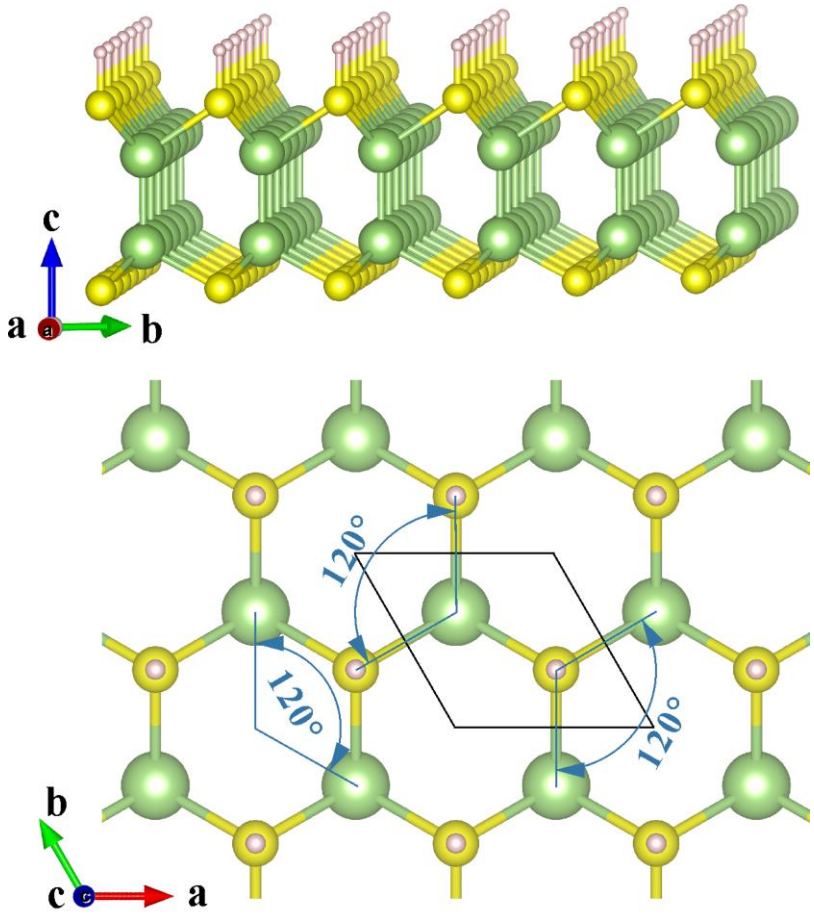

Figure 4-3: The optimized structure of H-doped (1×1×1) GaS supercell. Black lines outline a single unit cell.

The (2×2×1), (3×3×1) and (4×4×1) supercells were built from the pure 2-D

GaS, with each supercell containing one hydrogen. The relaxed structures are shown in Figure 4-4, 4-5 and 4-6, respectively and the geometrical parameters are listed in Table 4-1. The optimized S-H bond lengths are all around 1.41 Å, close to the S-H length in the (1×1×1) cell, except a much shorter S-H length of 1.36 Å in the (2×2×1) cell. The Ga_2-S_2 bonds for (2×2×1), (3×3×1) and (4×4×1) supercells show the same length of 2.36 Å, similar to that in the H-doped (1×1×1) cell. Similar trend is also observed for the bond lengths of Ga_1-S_1 in large supercells except that (2×2×1) cell has a much longer bond length of Ga_1-S_1.

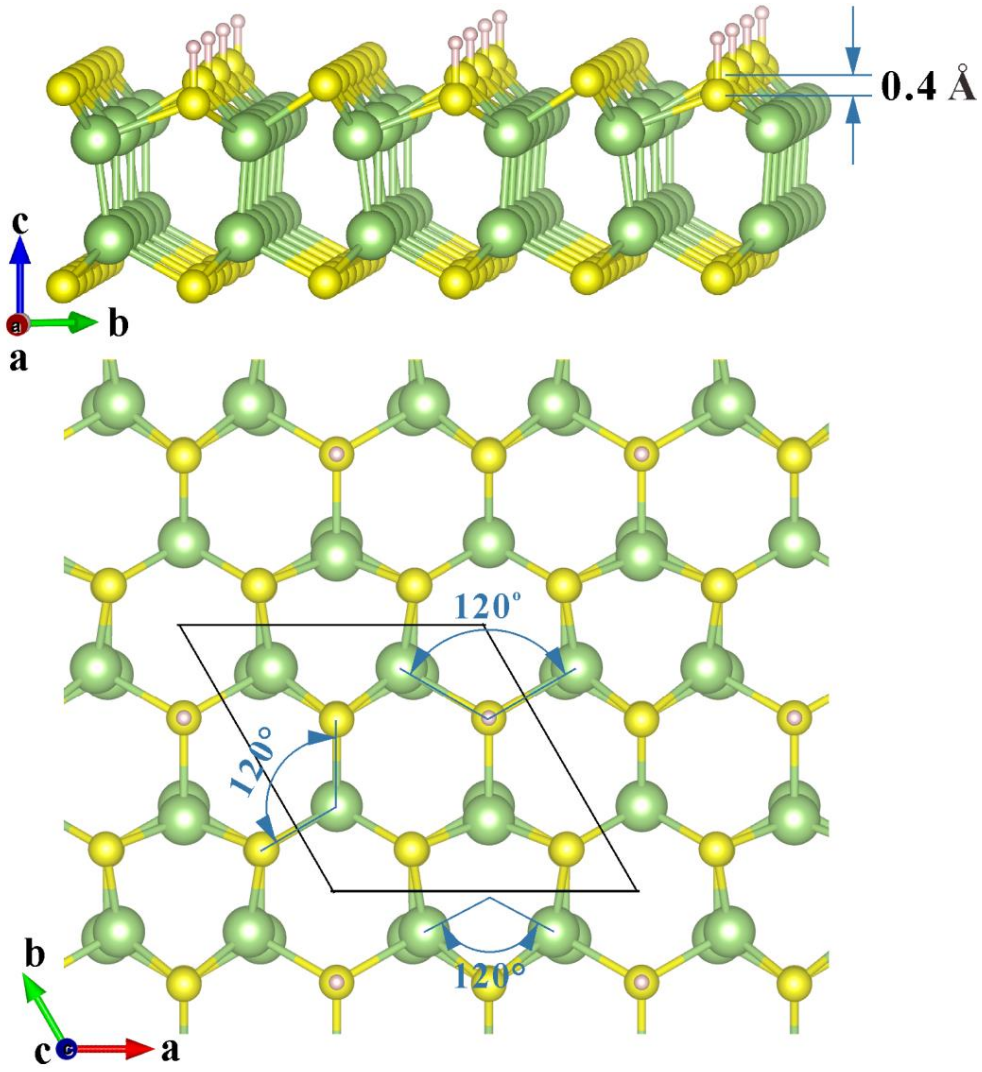

Figure 4-4: The optimized structure of H-doped (2×2×1) GaS supercell. Black lines outline a single unit cell.

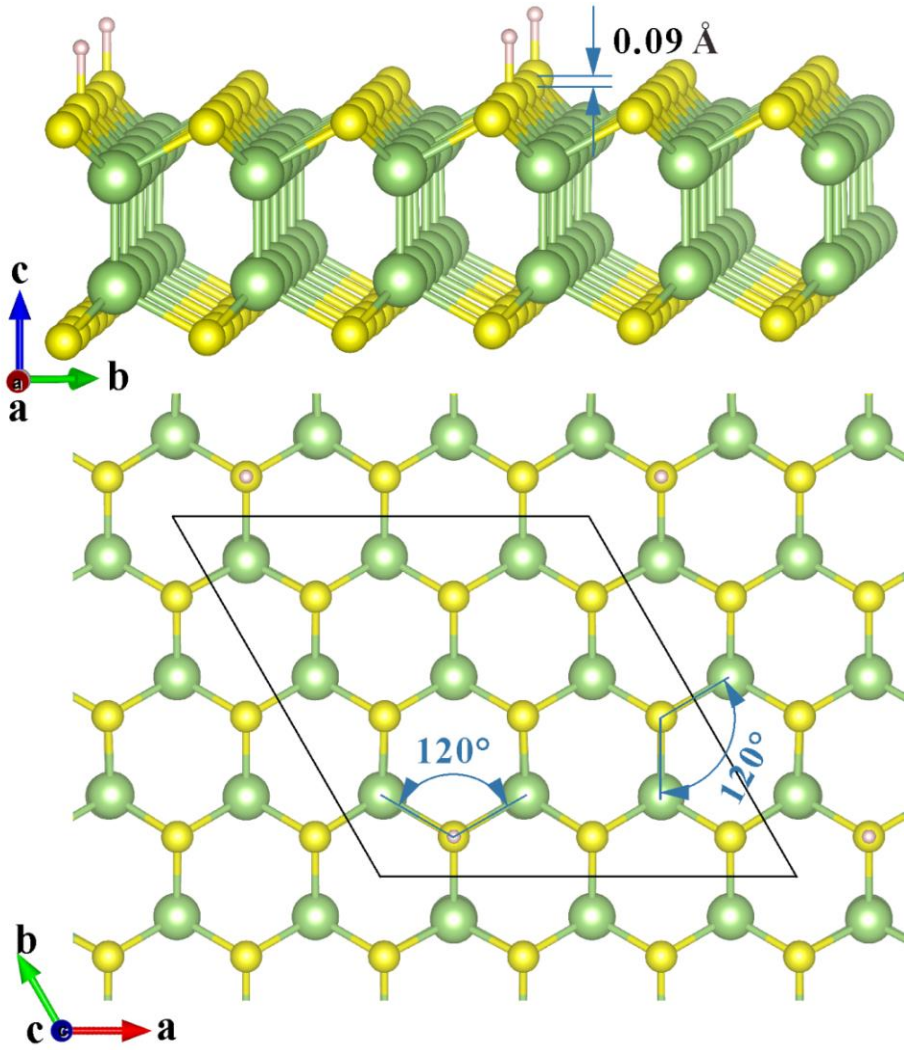

Figure 4-5: The relaxed structure of H-doped (3×3×1) GaS supercell. Black lines outline a single unit cell.

The optimized (2×2×1) cell also shows a significantly different feature of bond angles. The bond angle of Ga_1-Ga_2-S_2 (~126^o) is significantly larger than those of other supercells (~118^o), while the angle of S_1-Ga_1-Ga_2 (~103^o) is considerably smaller than others. These features cause a large shift in the position of Ga_1, as shown in Figure 4-4, nevertheless the influence on Ga_2 is negligible. The three Ga atoms nearest to hydrogen are equally pushed outwards along the S-Ga bond. As a result, the sulfur atom nearest to hydrogen is pushed down along z-axis while the six second-nearest S atoms

are pushed up. The difference in the heights of these two types of S atoms is about 0.4 Å along z-axis. Compared with the H-doped (1×1×1) supercell, the optimized (2×2×1) supercell also has a point group of C_{3v}, as shown in Figure 4-4.

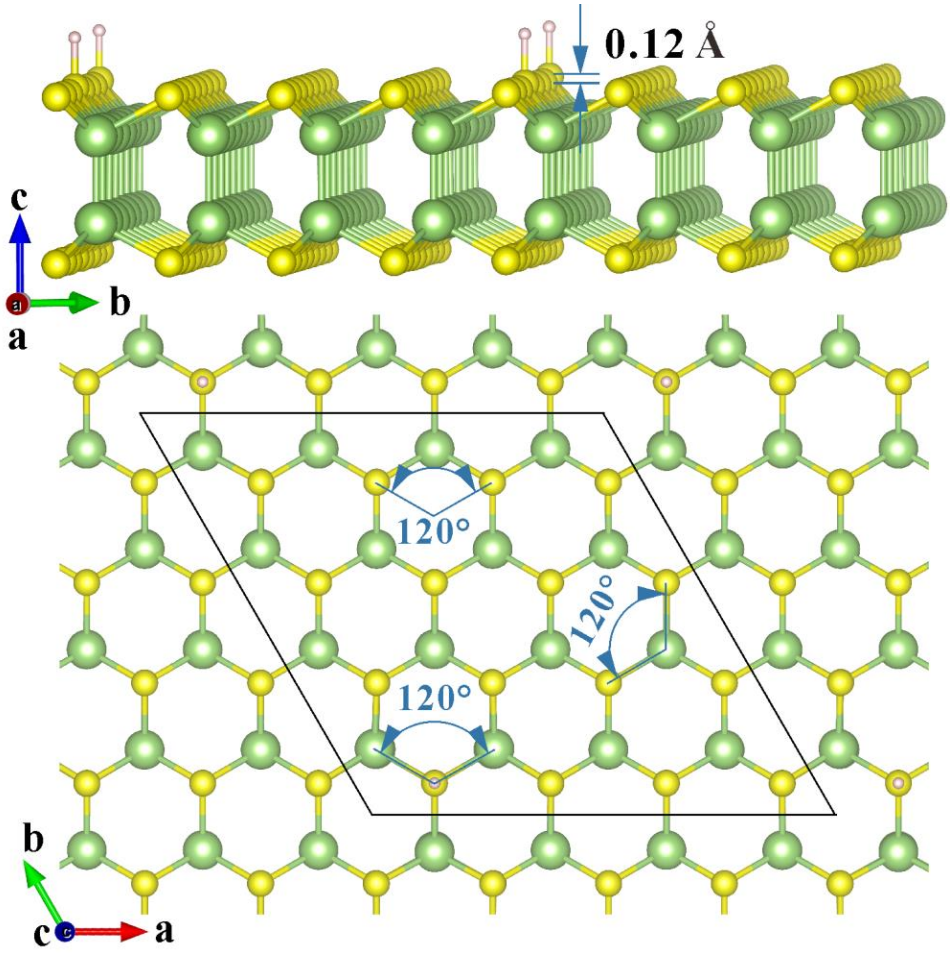

Figure 4-6: The optimized structure of H-doped (4×4×1) supercell. Black lines outline a single unit cell.

As presented in Figure 4-5 and 4-6, the (3×3×1) and (4×4×1) supercells with hydrogen doping also show the 3-fold symmetry of C_{3v}, while the structures exhibt very minor changes compared with the (2×2×1) supercell. The differences in the height of two sulfur atoms (nearest and second-nearest to H) are around 0.09 Å and 0.12 Å for (3×3×1) and (4×4×1) supercells, respectively. The variations are much smaller than 0.4 Å in the (2×2×1) case.

After comparison, we can see that the hydrogen atom causes structural changes to the top Ga and S atoms which accommodate the structural variation to keep the bottom atoms less affected.

4.3.2 The Electronic Structures of Bulk, Pure and H-doped 2-D GaS

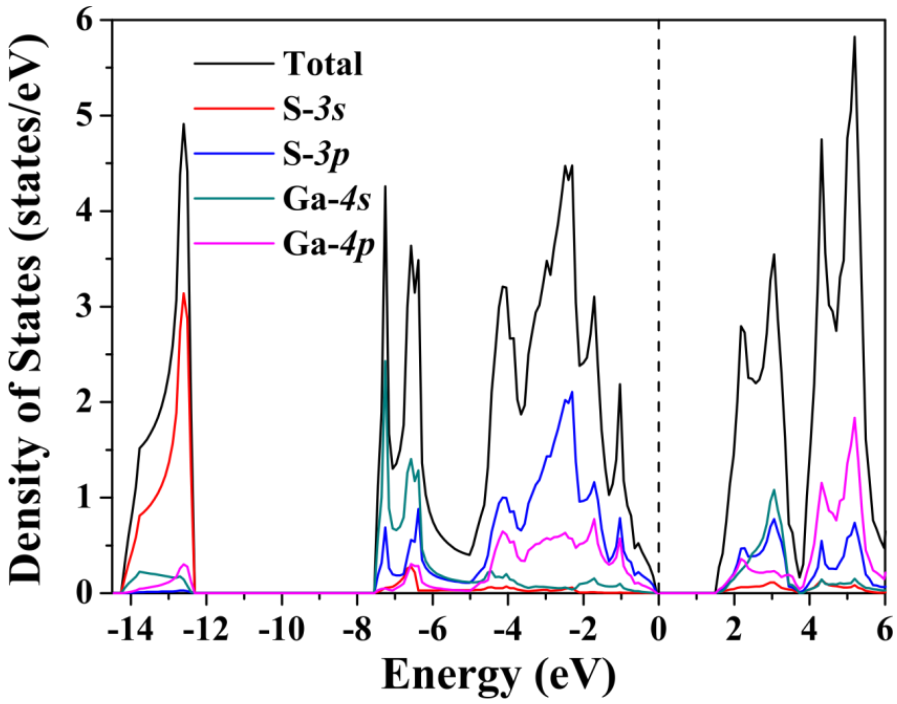

Figure 4-7: The total and partial density of states of bulk β-GaS. E_F is set at 0 eV.

After structural optimizations, the electronic structures of the above-mentioned models were also investigated. The calculated total and partial density of states (DOS) for the bulk β-GaS is shown in Figure 4-7. The density of states shows three well-defined regions below the Fermi level (E_F). The low-lying states with energy from -14 eV to -12 eV are mainly from S-*3s* states. A large gap of more than 4 eV separates the low-lying states from higher-energy states (from -7 eV to E_F). Within this energy range, the valence orbitals of Ga strongly hybridize with the S-*3p* states. The valence states can be further divided into two regions: -7 eV to -5 eV and -5 eV to 0 eV. Thefirst is mainly contributed by the Ga-*4s* states and partially by the S-*3p* states.

However, in the second region, the S-*3p* and Ga-*4p* states make major contributions and the former contributes more than the latter. The valence states of the bulk β-GaS exhibit the features similar to other metal oxides and sulfides.[5, 26] Similar to the electronic structure of Ga_2O_3, the empty states are formed by Ga-4s orbitals and anion's anti-bonding *p* orbital interactions. Ga-*4s* and S-*3p* empty states make similar contributions to the lower energy states from 1.5 eV to 4 eV, while the empty Ga-*4p* states primarily contribute to the states at higher energy (4-6 eV). This provides three-dimensional transport networks for charge carriers.

Figure 4-8a presents the total and partial DOS of the pristine 2-D GaS which show similar features to that of the bulk. Compared with the DOS of bulk β-GaS, the energy of S-*3s* occupied states shifts by about 1 eV towards E_F, and the bottom of strongly hybridized S-*3p* states region upshifts by 1 eV as well. Different states make similar contributions to the total DOS. Figure 8b clearly shows the contributions of the occupied states near E_F which are mainly from $3p_z$ and $4p_z$ states of sulfur and gallium. It is noted that the peak near E_F is sharp, implying the highly localized valence states and a large hole effective mass. Compared with that of bulk GaS, an increase of the band gap (2.7 eV) can be observed, which was also discerned in other two-dimensional materials, including MoS_2 and WS_2.[27-28]

As discussed above, the single-layer 2-D GaS as well as the bulk is a typical semiconductor. To improve its electrical conductivity, hydrogen was introduced as the simplest electron donor, which has been proven to effectively increase the conductivity of TiS_2 ultrathin films.[7] The densities of states for different supercells with H doping were calculated using a

sufficiently large Brillouin zone integration *k*-mesh. 39×39×1 *k*-points were used for the (1×1×1) H-doped single-layer GaS supercell. For other supercells, different meshes of 19×19×1, 13×13×1 and 9×9×1 *k*-points were utilized accordingly.

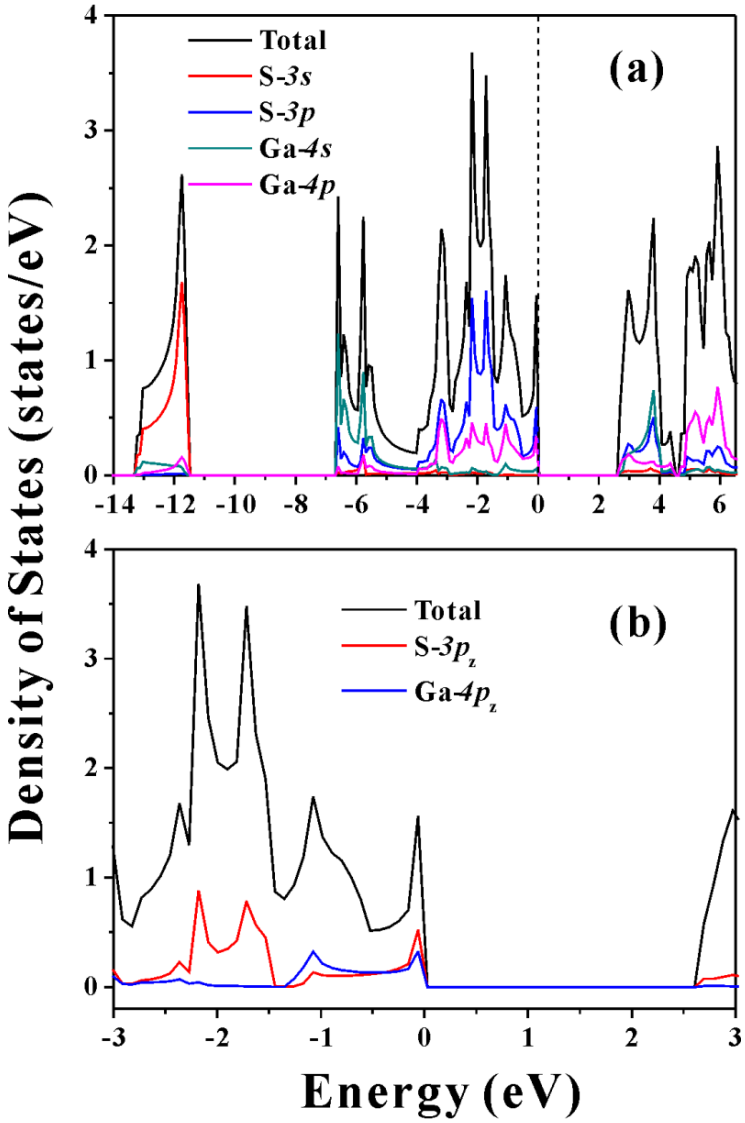

Figure 4-8: The total and partial DOS of the pure 2-D GaS at (a) wide energy region, (b) narrow region near E_F. E_F is set at 0 eV.

Figure 4-9a shows the partial DOS of H-doped 2-D GaS (1×1×1) structure. The low-lying occupied states of S-3*s* are excluded to show the more interesting region near Fermi level. As can be seen, the incorporation of H significantly increases the carrier concentration by filling the bottom of empty

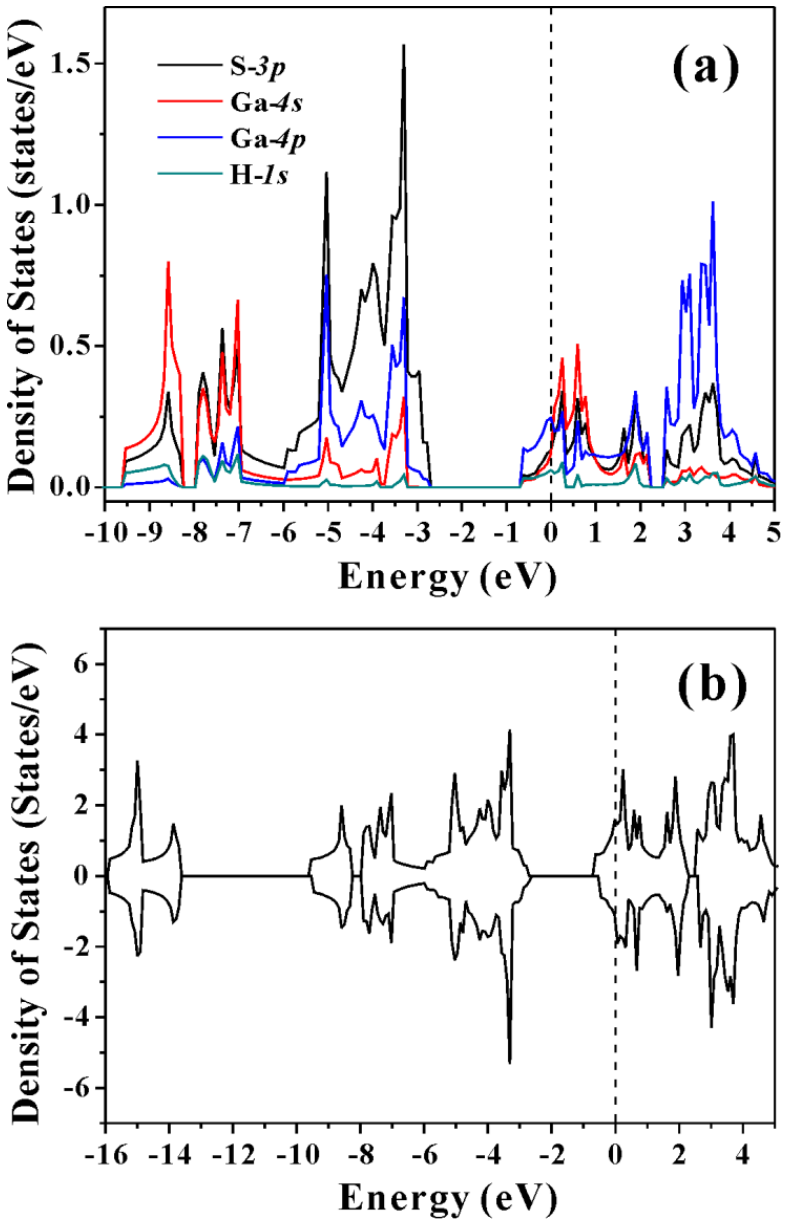

Figure 4-9: (a) partial DOS, (b) total spin-polarized DOS of H-doped (1×1×1) GaS. E_F is set at 0 eV.

states and pushes Fermi level into the conduction band. Therefore, a greatly enhanced electrical conductivity is implied. The single-layer 2-D GaS becomes conductive after hydrogen doping. Here the doping strategy is significantly different from traditional n-type TCOs which adopt substitutional dopants to metal-oxide hosts.[29] Compared with pristine 2-D GaS, the hydrogen doping narrows the fundamental gap by 0.4 eV to about 2.2 eV,

which is due to the many-body effect arising from the increased concentration of free carriers.[29] In contrast, a pronounced Burstein-Moss (BM) shift is also observed because of the filled states at the conduction band bottom, which compensates the narrowing of fundamental gap. As shown in Figure 4-9a, the BM shift raises the optical band gap back to 2.8 eV. Therefore, no significant optical transparency would be lost due to the reduced fundamental band gap.

Considering that the reduced symmetry might cause magnetization in the system whose bulk is nonmagnetic,[5] we have calculated the spin-polarized total DOS of the system. As shown in Figure 4-9b, the spin-up and spin-down total DOS display a symmetrical feature at same energy regions. After integration of the total DOS to E_F, the numbers of electrons for both spin-up and spin-down states are found to be 9.5, implying the nonmagnetic behavior of the (1 ×1 ×1) H-doped 2-D GaS structure.

The densities of states for 2-D GaS with different concentrations of H doping are presented in Figure 4-10. Different from the H-doped (1 ×1 ×1) supercell, all the three large cells show a second energy gap above Fermi level. It was reported that the incorporation of hydrogen in metastable zinc-blend structured GaS opened a gap of 0.9 eV which caused a metal to semiconductor transition. The bonding of Ga-H interactions which weakened the anti-bonding character of Ga-S was believed to be responsible for the gap formation.[25] However, the interaction of Ga-H is absent in our case. Thus, it is more likely a formation of mid-gap states which are contributed by different states in the order of Ga-*4p*>S-*3p*>Ga-*4s*>S-*3s*>H-*1s*.

4.3.3 The Band Structures of Bulk, Pure and H-doped 2-D GaS

The energy bands of the bulk β-GaS are shown in Figure 4-11 with Fermi

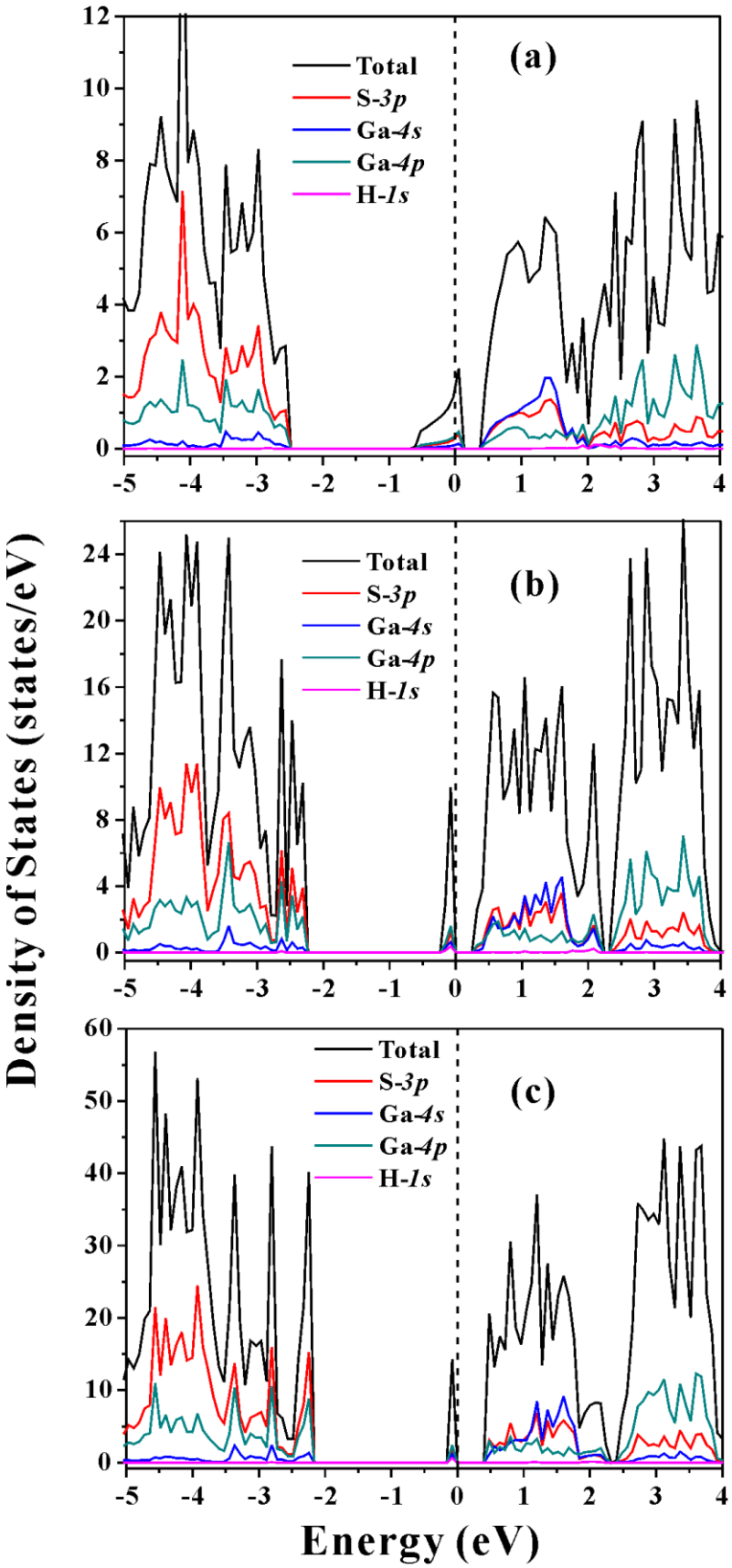

Figure 4-10: The partial and total DOS of the different 2-D GaS supercells: (a) (2×2×1), (b) (3×3×1), and (c) (4×4×1). E_F is set at 0 eV.

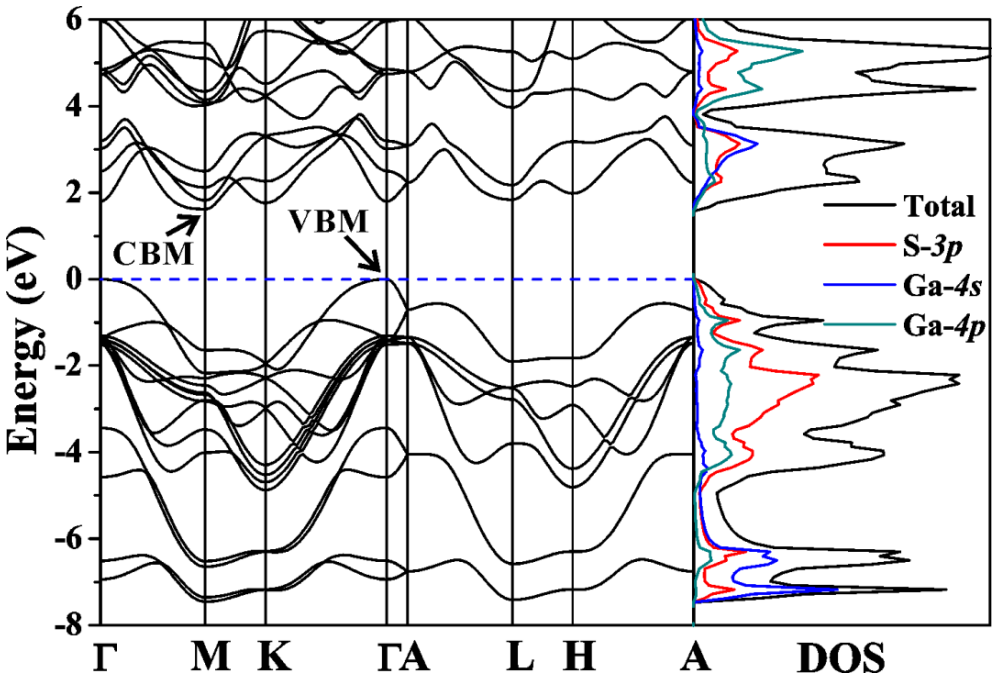

Figure 4-11: The band structure of bulk GaS. E_F is set at 0 eV.

energy set at 0 eV. The low-lying S-*3s* band is not shown for a better clarity. We can see the semiconductor nature of bulk β-GaS with a gap about 1.6 eV appearing between the valence band and conduction band, which is consistent with the gap obtained from density of states. We also notice that the valence band maximum (VBM) is located at Γ point whereas the conduction band minimum (CBM) sits at the M point of first Brillouin zone, implying that bulk GaS is an indirect band-gap semiconductor. The indirect and direct band gaps are calculated to be 1.62 eV and 1.80 eV, respectively. The calculated band gaps are much lower than the reported values (indirect gap: 2.5 eV, direct gap: 3.05 eV) which is due to the band gap underestimation by DFT.[25, 30]

The band structure of pure single-layer 2-D GaS is shown in Figure 4-12. Obviously the semiconductor feature is maintained after thinning the bulk GaS into 2-D layer, while the energy gap increases. The conduction band minimum of 2-D GaS remains situated at the M point of the Brillouin zone, whereas the

VBM shifts dramatically. We can observe two symmetrically split valence band maxima at the both sides of Γ point with a slightly energy difference (-6.1 meV). Compared with that of bulk GaS, the indirect band gap of single-layer GaS is greatly enhanced to be about 2.61 eV.

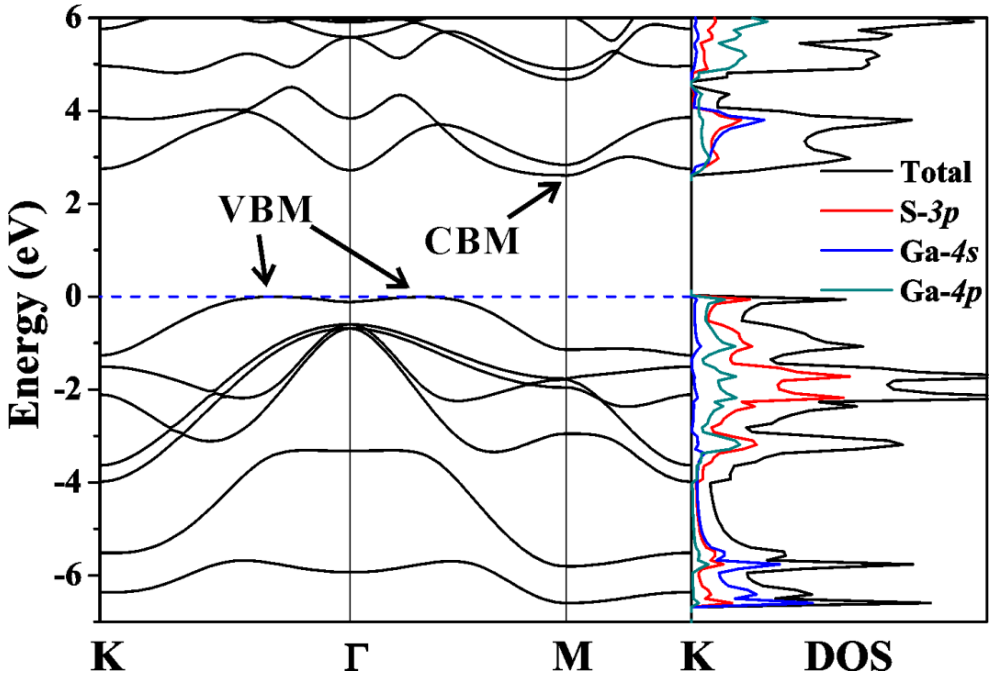

Figure 4-12: The band structure of pure 2-D GaS. E_F is set at 0 eV.

To evaluate the effect of layer numbers on valence band maximum, we further calculate the band structures of GaS from 2 to 6 layers. An empty space of at least 12 Å along z-axis is used to eliminate artificial interactions between slabs. The evolution of VBM versus layer numbers is presented in Figure 4-13.

Apparently, 1L GaS has the largest splitting of two valence band maxima. Increasing the layer numbers significantly shifts the two VBM towards Γ point. The splitting of VBM is negligible when the thickness reaches five layers. Further increasing the thickness of GaS to 6 layers will lead to the band structure similar to the bulk (data not shown). The variation of VBM positions

with thicknesses was also observed in other layer-structured transition metal sulfides and selenides, including MoS_2, WS2, WSe_2, etc.[27-28] However, none of them exhibited a double VBM when the materials were thinned down to a single layer. The peculiar electronic property might explain the high-response behavior of 2-D GaS photodetector.[10]

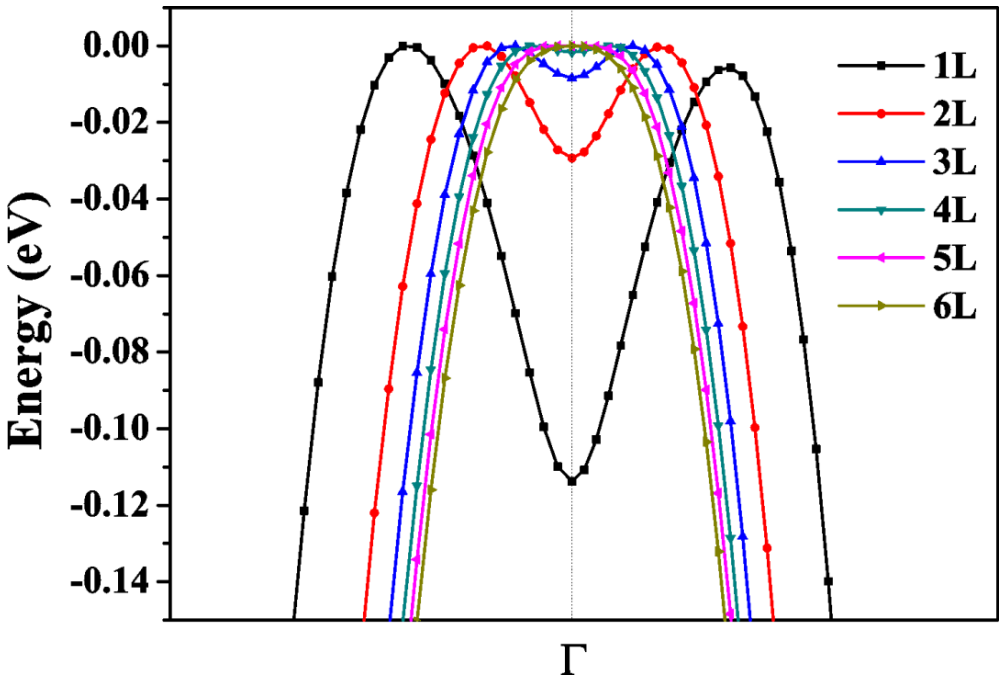

Figure 4-13: The band structures showing VBM of 2-D GaS from 1L to 6L. E_F is set at 0 eV. Dash line indicates the position of Γ.

The band structure of H-doped (1×1×1) GaS is shown in Figure 4-14. From the figure, we can clearly observe that Fermi level is shifted into the conduction band due to the hydrogen doping, which implies a good electrical conductivity. The indirect band gap is reduced by 0.56 eV compared with that of the pure single-layer GaS. A pronounced Burstein-Moss shift (ΔBM) of 0.33 eV is also observed, which can compensate for the band gap renormalization due to many-body effects.[29] The band structures of different supercells are also calculated and the results are shown in Figure 4-15. A second energy gap can be observed for all three supercells. The electronic

band structures show a good consistence with the density of states discussed above.

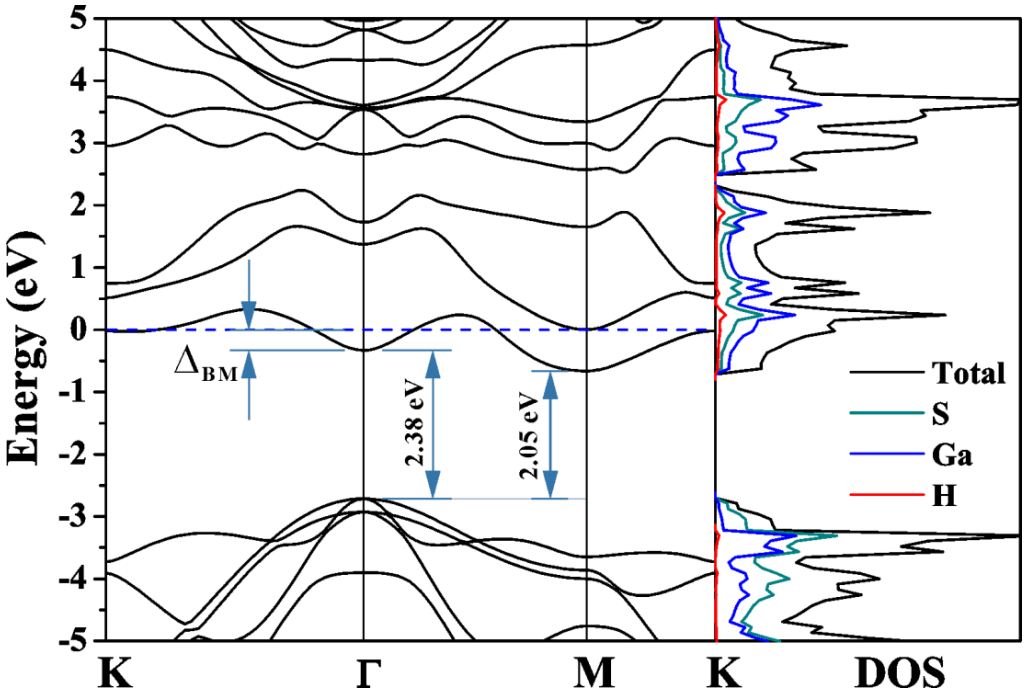

Figure 4-14: The band structure of H-doped (1×1×1) GaS. ΔBM=0.33 eV. E_F is set at 0 eV.

4.3.4 The Transport Properties of H-doped 2-D GaS

In previous sections, we have discussed the electronic structures of various β-GaS structures. The improved electrical conductivities of 2-D GaS after hydrogen doping have been qualitatively observed. In order to develop a suitable transparent conductor, a quantitative study of the carrier transport properties is extremely essential. In this section, a semi-classic calculation of carrier transport properties in H-doped 2-D GaS will be performed. The simulation was conducted by using the code BoltzTrap which was developed based on Boltzmann equation, assuming a constant relaxation time of carriers and a parabolic shape of the conduction band minimum.[23] The structures and eigenvalues obtained from VASP self-consistent calculation were converted by the VASP to BoltzTrap interface before being initiated to calculate trans-

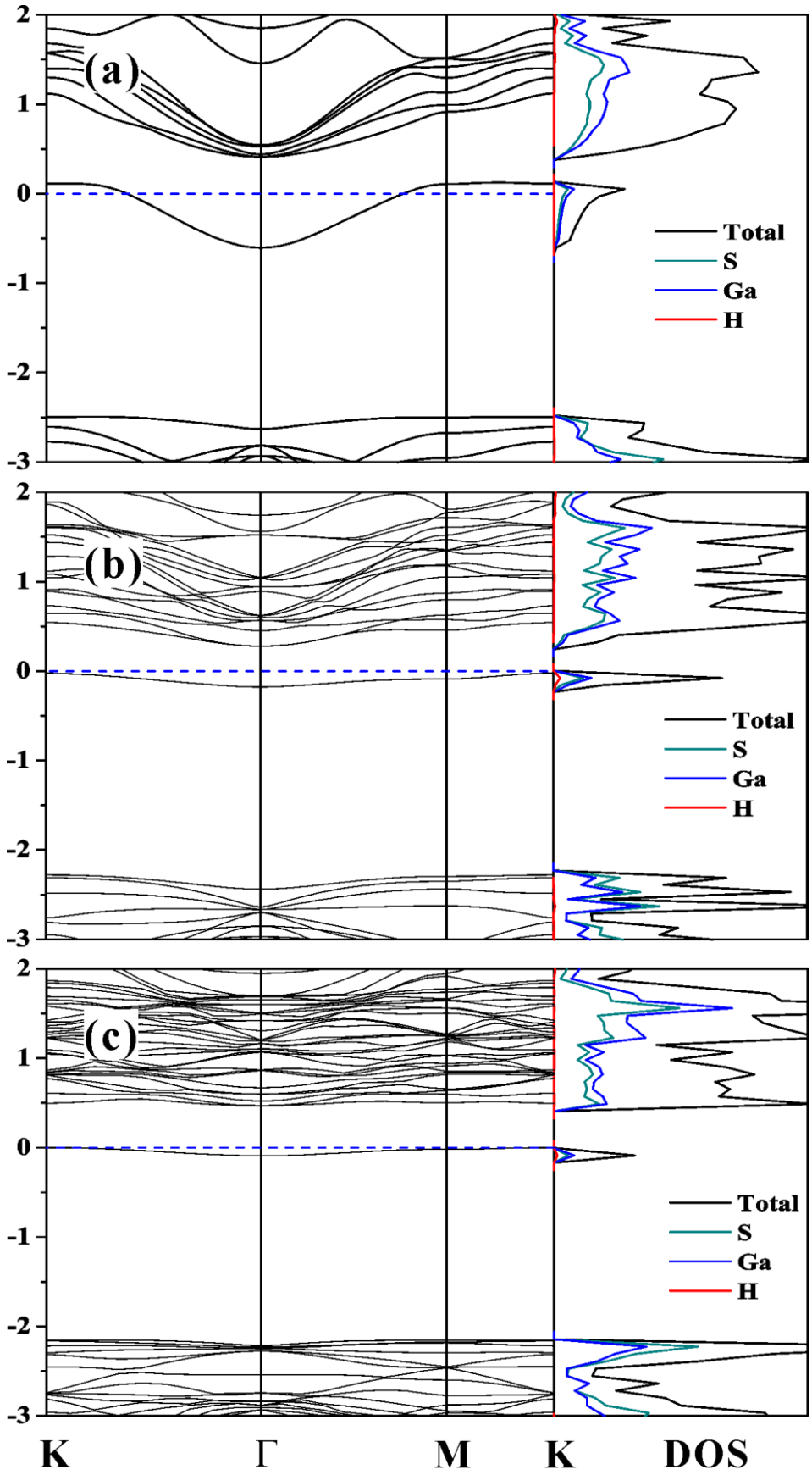

Figure 4-15: The band structures of the H-doped (a) (2×2×1), (b) (3×3×1) and (c) (4×4×1) 2-D GaS. E_F is set at 0 eV.

port properties. To improve the accuracy of transport properties, a sufficiently denser mesh of *k*-points was applied during the self-consistent calculation of energy eigenvalues.

The BoltzTrap code produces conductivity in the form of σ/τ, where σ and τ refer to the electrical conductivity and carrier relaxation time respectively. To present the results in the conventional way of conductivity or resistivity (ρ), the relaxation time of τ is necessary. Due to the rare report about experimental transport properties in 2-D β-GaS, we evaluate the relaxation time approximately according to Equation (1-4): $\mu = e\tau/m^*$. μ, e, τ and m^* denote the carrier mobility, elementary charge, average relaxation time and effective mass, respectively. The effective mass can be obtained by fitting the parabolic conduction band minimum using Equation (3-1) by $\frac{1}{m^*} = \frac{1}{\hbar^2}\frac{d^2\varepsilon(k)}{dk^2}$, where $\varepsilon(k)$, $\hbar$, and k represent the band dispersion relation, reduced Planck constant and wave vector, respectively.[31] Therefore, from the second-derivative of the energy dispersion of 2-D GaS at CBM, we obtain an effective mass $m^* = 0.42m_0$ (rest electron mass: $m_0 = 9.109\times10^{-31}$ kg). The effective mass is slightly larger than those of commonly used transparent conducting oxides (from $0.14m_0$ to $0.35m_0$), including In_2O_3, SnO_2, Ga_2O_3 and ZnO.[26, 29, 32] The larger effective mass might be due to the relatively increased contribution of anions' localized *2p* states versus delocalized cations' *s* states in 2-D GaS, as revealed in Figure 4-12.[29] Given the effective mass and carrier mobility of $\mu \approx 25$ $cm^2/(V\cdot s)$ (Kipperman et al.[33]), we can easily calculate the average relaxation time ($\tau = 5.72\times10^{-15}$ s) as well as the electrical resistivity.

Figure 4-16a shows the calculated resistivity of H-doped 2-D GaS with

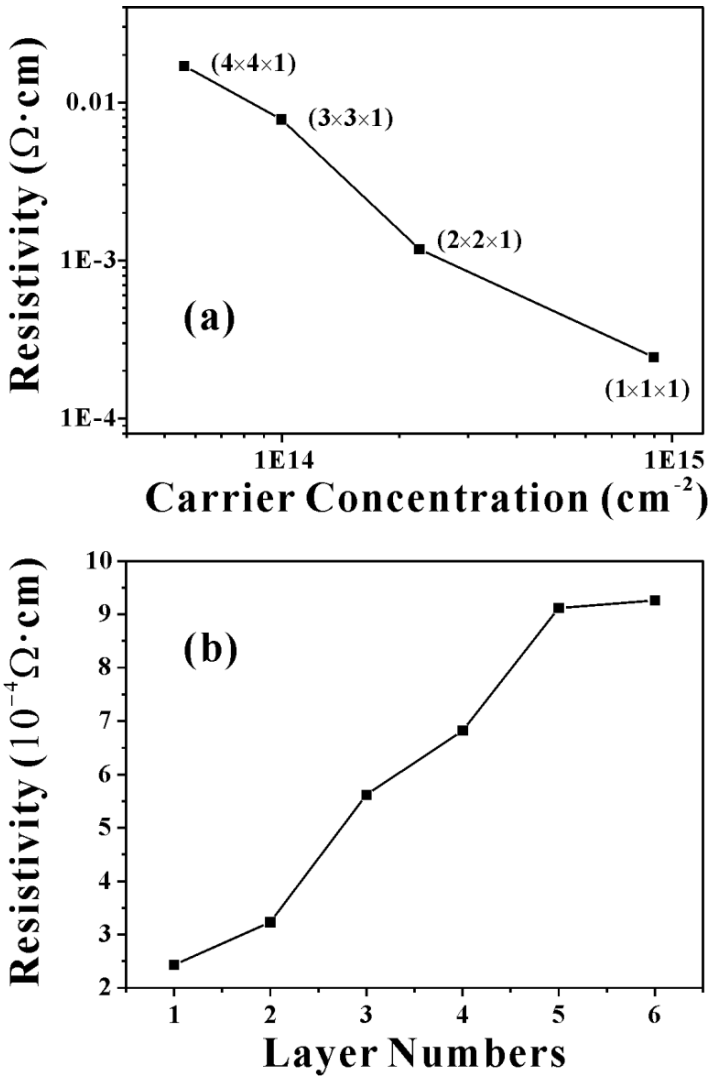

Figure 4-16: The transport properties of the 2-D GaS with (a) different doping concentrations and (b) different layers.

different sizes of supercells. As can be seen, the H-doped (4×4×1) GaS shows the highest resistivity of 3.55×10^{-2} Ω·cm. The carrier concentration is estimated to be 5.62×10^{13} cm^{-2}. The highest carrier concentration is calculated to be 8.98×10^{14} cm^{-2} in H-doped (1×1×1) supercell. The lowest resistivity is calculated to be 2.43×10^{-4} Ω·cm, which is comparable with these of widely used TCO thin films. Figure 4-16b presents the layer-dependent resistivity of H-doped 2-D GaS. All the structures were obtained by using the corresponding numbers of [S-Ga-Ga-S] unit and adding one

hydrogen to the topmost sulfur atom, while keeping at least 12 Å of empty space along z-axis. According to the simulated results, increasing the number of layers moderately increases the electrical resistivity, but still on the order of 10^{-4} Ω·cm.

It should be noted that all conductivities shown here merely represent the averages of the conductivity tensors along x-axis and y-axis. The conductivity tensor along z-axis is not considered due to the broken symmetry along this direction in 2-D structures. However, the thicker the film, the more the conductivity tensor along z-axis contributes to overall conductivity. In view of this point, we may understand the peculiar trend of the conductivity versus the thickness.

4.4 Conclusion

To sum up, the geometrical and electronic structures as well as transport properties of the bulk β-GaS, pure and H-doped 2-D β-GaS have been theoretically investigated in this Chapter. It is found that:

(1) The hydrogen doping causes geometrical changes to the symmetry, bond lengths and bond angles in 2-D structured GaS.

(2) The electronic properties have shown a band gap renormalization and Burstein-Moss shift after the hydrogen doping. The BM shift can compensate the decreasing of fundamental gap to maintain a higher optical band gap. Considering the weakness of DFT in band gap prediction, the band gap of H-doped 2-D GaS would be sufficient to keep the transparency window above 400 nm.

(3) The transport properties of H-doped GaS reveal low resistivities which can meet the required benchmark resistivity ($\rho \sim 10^{-4}$ Ω·cm) of transparent

conducting films. The fundamental studies presented here might be helpful to develop novel two-dimensional GaS transparent conductors.

References

1. Mirri, F.; Ma, A. W. K.; Hsu, T. T., et al., *ACS Nano* **2012,** *6*, 9737-9744.
2. Bult, J. B.; Crisp, R.; Perkins, C. L., et al., *ACS Nano* **2013,** *7*, 7251-7261.
3. Geng, H. Z.; Kim, K. K.; So, K. P., et al., *J. Am. Chem. Soc.* **2007,** *129*, 7758-7759.
4. Bae, S.; Kim, H.; Lee, Y., et al., *Nat. Nanotechnol.* **2010,** *5*, 574-578.
5. Lebègue, S.; Eriksson, O., *Phys. Rev. B* **2009,** *79*, 115409.
6. Xu, M.; Liang, T.; Shi, M., et al., *Chem. Rev.* **2013,** *113*, 3766-98.
7. Lin, C.; Zhu, X.; Feng, J., et al., *J. Am. Chem. Soc.* **2013**, 135, 5144-5151.
8. Aono, T.; Kase, K.; Kinoshita, A., *J. Appl. Phys.* **1993,** *74*, 2818-2820.
9. Sinha, G.; Panda, S. K.; Datta, A., et al., *ACS Appl. Mater. Inter.* **2011,** *3*, 2130-2135.
10. Hu, P.; Wang, L.; Yoon, M., et al., *Nano Lett.* **2013,** *13*, 1649-1654.
11. Macinnes, A. N.; Power, M. B.; Barron, A. R., *Chem. Mater.* **1992,** *4*, 11-14.
12. Wen, B.; Melnik, R.; Yao, S., et al., *Mat. Sci. Semicon. Proc.* **2010,** *13*, 295-297.
13. Gautam, U. K.; Vivekchand, S. R.; Govindaraj, A., et al., *J. Am. Chem. Soc.* **2005,** *127*, 3658-3659.

14. Hohenberg, P.; Kohn, W., *Phys Rev.* **1964,** *136*, B864-B871.

15. Kohn, W.; Sham, L. J., *Phys. Rev.* **1965,** *140*, A1133-A1138.

16. Kresse, G.; Furthmuller, J., *Comput. Mater. Sci.* **1996,** *6*, 15-50.

17. Kresse, G.; Furthmuller, J., *Phys. Rev. B* **1996,** *54*, 11169-11186.

18. Blochl, P. E., *Phys. Rev. B*, **1994,** *50*, 17953-17979.

19. Kresse, G.; Joubert, D., *Phys. Rev. B* **1999,** *59*, 1758-1775.

20. Perdew, J. P.; Burke, K.; Ernzerhof, M., *Phys. Rev. Lett.* **1996,** *77*, 3865-3868.

21. Monkhorst, H. J.; Pack, J. D., *Phys. Rev. B* **1976,** *13*, 5188-5192.

22. Grimme, S., *J. Comput. Chem.* **2006,** *27*, 1787-99.

23. Madsen, G. K. H.; Singh, D. J., *Comput. Phys. Commun.* **2006,** *175*, 67-71.

24. d'Amour, H.; Holzapfel, W. B.; Polian, A., et al., *Solid State Commun.* **1982,** *44*, 853-855.

25. Machado-Charry, E.; Canadell, E.; Segura, A., *Phys. Rev. B* **2007,** *75*, 045206.

26. Medvedeva, J. E.; Hettiarachchi, C. L., *Phys. Rev. B* **2010,** *81*, 125116.

27. Yun, W. S.; Han, S. W.; Hong, S. C., et al., *Phys. Rev. B* **2012,** *85*, 033305.

28. Kuc, A.; Zibouche, N.; Heine, T., *Phys. Rev. B* **2011,** *83*, 245213.

29. Mryasov, O. N.; Freeman, A. J., *Phys. Rev. B* **2001,** *64*, 233111.

30. Seidl, A.; Gorling, A.; Vogl, P., et al., *Phys. Rev. B* **1996,** *53*, 3764-3774.

31. Lange, B.; Freysoldt, C.; Neugebauer, J., *Phys. Rev. B* **2010,** *81*, 224109.

32. Preissler, N.; Bierwagen, O.; Ramu, A. T., et al., *Phys. Rev. B* **2013,** *88*, 085305.

33. Kipperman, A. H. M.; van der Leeden, G. A., *Solid State Commun.* **1968,** *6*, 657-662.

Chapter 5

Adsorption of Trimesic Acid on ITO Nanoparticles

5.1 Introduction

As introduced in **Chapter 1**, carboxylic acids could be facilely attached onto the ITO surface via various interactions, including electrostatic and hydrogen bonding interactions and coordinate-covalent bonding between carboxylate and metal ion sites.[1] These adsorbed carboxylic acids molecules offer ITO surface better wettability to organic layer, enhanced electron transfer rate across interface, which imply their potential applications in optoelectronic devices, such as organic light-emitting diode and organic photovoltaic.[1]

Trimesic acid (Bezene-1,3,5-tricarboxylic acid, TMA) is a planar molecule with a three-fold symmetry. It has shown very interesting assembly patterns on copper, gold as well as other substrates.[2-3] TMA is also an important building block in the supramolecular chemistry for the synthesis of various metal centered organic framework (MOF).[4] The assembly of TMA on transparent conductive films may provide additional opportunity to tune the surface chemistry for their applications in various optoelectronic devices.

In this Chapter, we devote our efforts to study the adsorption of TMA molecules on ITO nanoparticles, considering the easier preparation and characterization compared with the assembly on ITO film. Various spectroscopic techniques have been employed to investigate the adsorption, including Raman spectroscopy, diffuse reflectance infrared Fourier transform

spectroscopy and X-ray photoelectron spectroscopy. Using the density functional theory, we provide a fundamental understanding of the adsorption behavior of TMA molecules on the ITO (111) surface. The TMA-adsorbed ITO nanoparticles have shown greatly enhanced electrocatalytic effect towards the electrochemical probe molecules of ferrocene.

5.2 Experimental and Computational Details

5.2.1 Synthesis of ITO Nanoparticles

ITO nanoparticles were synthesized via a co-precipitation.[5] The synthesis mainly involved three steps: (1) dissolve indium nitrate hydrate (9 mmol) and tin tetrachloride hydrate (1 mmol) in ethanol (100 ml); (2) add 40 mL of ammonia solution containing β-alanine (2 g) into the precursor solution dropwisely under rapid stirring; (3) separate white precipitates followed by drying and further calcination at 300 ^{o}C for 2 h.

5.2.2 Surface Modification by Trimesic Acid

Prior to the surface modification, ITO nanoparticles (0.5 g) were treated with base piranha ($NH_3 \cdot H_2O/H_2O_2/H_2O$=3/3/4 v/v/v) at 80 ^{o}C for 30 min. After being rinsed with DI-water and ethanol several times, the ITO nanoparticles were dispersed into a TMA/ethanol solution (50 mg/ml) under sonication. The mixture was kept at room temperature in shaking incubator operating at 100 rpm, for 24 h. The ITO nanoparticles were collected by centrifugation and repeated washing with acetonitrile. The samples were finally dried at room temperature under vacuum.

5.2.3 Characterization

X-ray diffraction (XRD) patterns were collected on a Siemens D5005 X-ray diffractometer with Cu Kα source (λ=1.5406 Å), operated at 40 kV and 40

mA. Images of field-emission scanning electron microscopy (FESEM) and high-resolution transmission electron microscopy (HRTEM) were taken from a JOEL JSM-6701F FESEM and JEOL JEM 3010 HRTEM, respectively. Raman spectra were recorded by a Raman spectroscopy (JY Horiba LabRAM HR, Laser: Ar^+ 514 nm, power: 2 mW, integration time: 20 s, coaddition: 20). Diffuse reflectance infrared Fourier transform spectra (DRIFTS) were obtained using a Harrick praying mantis accessory incorporated into a Varian Excalibur FTS-3000 FTIR spectrometer with pure KBr as the background. The samples were placed in the closed sample chamber and purged with Ar for 20 min before data collection. The DRIFT spectra were collected with a coaddition of 1000, resolution of 4 cm^{-1} and sensitivity of 16. The Fourier transform infrared (FTIR) spectra were collected on a Varian 3100 FTIR spectrometer (resolution 2 cm^{-1}, 256 scans). X-ray photoelectron spectroscopy (XPS) was recorded on a Kratos AXIS Ultra HAS spectrometer equipped with a monochromatic Al Kα X-ray source (hν=1486 eV), operated at 15 kV and 5 mA. Peak fitting was performed with the software XPSPEAK 4.1 and a Shirley background subtraction.

5.2.4 Electrochemical Measurement

Cyclic voltammetry of TMA-adsorbed ITO nanoparticles towards the probe molecules of ferrocene was collected by a standard three-port electrochemical cell and a CHI900B electrochemical workstation. The measurement was performed with a Ag/AgCl reference electrode, a platinum counter electrode and a gold working electrode covered by TMA-adsorbed ITO nanoparticles. During the measurement, $LiClO_4$ (0.25 M) and ferrocence (1 mM) in distilled acetonitrile served as the supporting electrolyte and electrochemically active

probe material respectively. All data were collected after several scans to achieve good reproducibility.

5.2.5 Computational Details

The calculations were performed by density functional theory as implemented in the code VASP,[6-7] with the electron-ion interactions described by the projector augmented wave (PAW) method.[8-9] The exchange-correlation potential was incorporated in the generalized gradient approximation (GGA) using the Perdew-Burke-Ernzerhof functional (PBE).[10] The *2s* and *2p* orbitals of oxygen, *5s* and *5p* orbitals of indium and tin were treated as the valence electrons. All geometrical structures were fully relaxed until total energy was converged to be less than 10^{-5} eV and total force less than 0.01 eV/Å on each atom.

The primitive cell of bcc In_2O_3 contains 24 O and 16 In atoms with four indium occupying the *8b* cationic site and the other indium staying at the *24d* position. Considering the computational cost, 6.25 at%, instead of 10%, was chosen as the dopant concentration by substitutionally replacing one In with one Sn atom. Previous work has shown that Sn at *8b* site is more preferred since it has a lower total energy compared with the doping at *24d* site.[11] We compared the two different doping sites and consolidated that the *8b* site is more favorable in terms of total energy ($\Delta E \approx 0.07$ eV/unit cell).The geometry and unit cell of ITO were fully optimized with a $3\times3\times3$ Monkhorst-Pack[12] *k*-point mesh and a cutoff energy of 500 eV.

The ITO (111) surface was cleaved from the optimized ITO bulk by using six layers (two ionic layers), totally containing 30 In, 48 O and 2 Sn atoms. During the structural optimization, the bottom three layers were fixed. A

vacuum of 25 Å was inserted to prevent interactions between slabs. A mesh of 9×9×1 *k*-points was used for the total energy calculation while the cutoff energy and criteria of total energy and force were kept same as that in bulk case.

5.3 Results and Discussion

5.3.1 Characterization of ITO Nanoparticles

The phase and morphology of ITO nanoparticles were investigated by XRD, FESEM and TEM. A typical XRD pattern is shown in Figure 5-1 with all diffraction peaks properly labeled. As can be seen, all the peaks could be indexed to the body-centered cubic (bcc) In_2O_3 structure. The standard pattern is also shown as the reference (vertical lines, ICDD Card No.: 06-0416). No discernible diffraction peaks from SnO or SnO_2 could be detected, indicating a substitutional incorporation of Sn into the indium site. The average primary particle size is estimated to be about 10 nm according to the Scherrer equation.

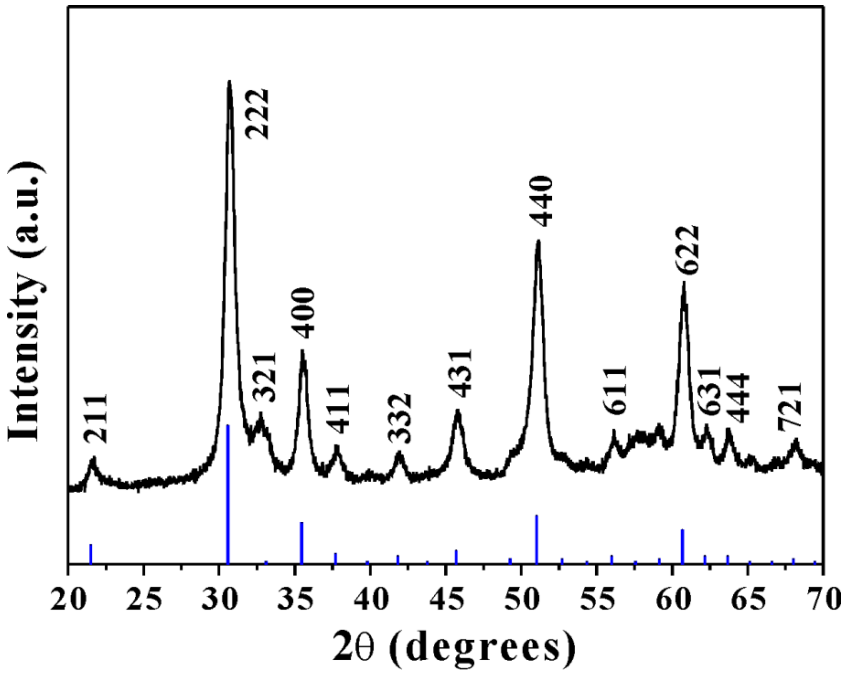

Figure 5-1: The XRD pattern of ITO nanoparticles.

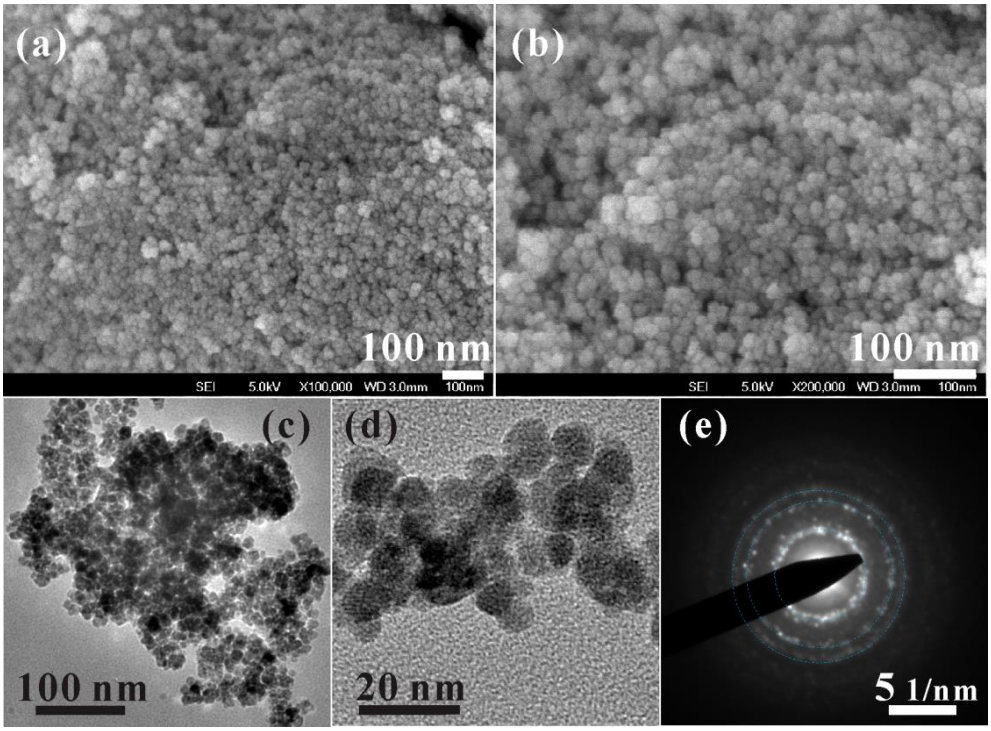

Figure 5-2: (a-b) FESEM images, (c-d) TEM image and (d) SAED pattern of ITO nanoparticles.

Although ITO nanoparticles form large secondary aggregates (SEM images not shown here), the primary ITO nanoparticles are in spherical shape with uniform and small sizes, as shown in Figure 5-2a and 2b. TEM images (Figure 5-2c and 2d) further confirm the spherical shape of ITO nanoparticles with sizes ranging from 8 to 15 nm. A selected area electron diffraction (SAED) pattern of ITO nanoparticles is presented in Figure 5-2e. The SAED pattern exhibits the polycrystalline nature of ITO nanoparticles, as indicated by the diffraction rings. The three diffraction rings can be indexed to the (222), (440) and (622) Miller planes of bcc In_2O_3 structure, respectively, which correspond to the three main peaks in the XRD pattern.

5.3.2 Adsorption of Trimesic Acid on ITO Nanoparticles

Raman Spectroscopy

Raman spectroscopy has been employed to investigate the adsorption of

TMA on ITO nanoparticles. Figure 5-3 shows the Raman spectra of the bare and TMA-adsorbed ITO nanoparticles as well as pure TMA solids. Comparing Figure 5-3a with 3b, one can clearly observe the new Raman bands at 806, 1002, 1452, 1603, 1705 and 3081 cm^{-1} for the ITO nanoparticles modified by TMA molecules. The band at 3081 cm^{-1} corresponds to the sp^2-C-H stretching mode due to TMA molecules. The strong bands at 1603 and 1002 cm^{-1} are assigned to the typical C=C stretching (ν_{8a}) and symmetric ring breathing (ν_1) modes of the 1, 3, 5-trisubstituted benzene ring, respectively.[13-14] Compared with the Raman spectrum of solid TMA (Figure 5-3c), no obvious shifts of the three bands positions can be observed after TMA was adsorbed onto ITO nanoparticles.

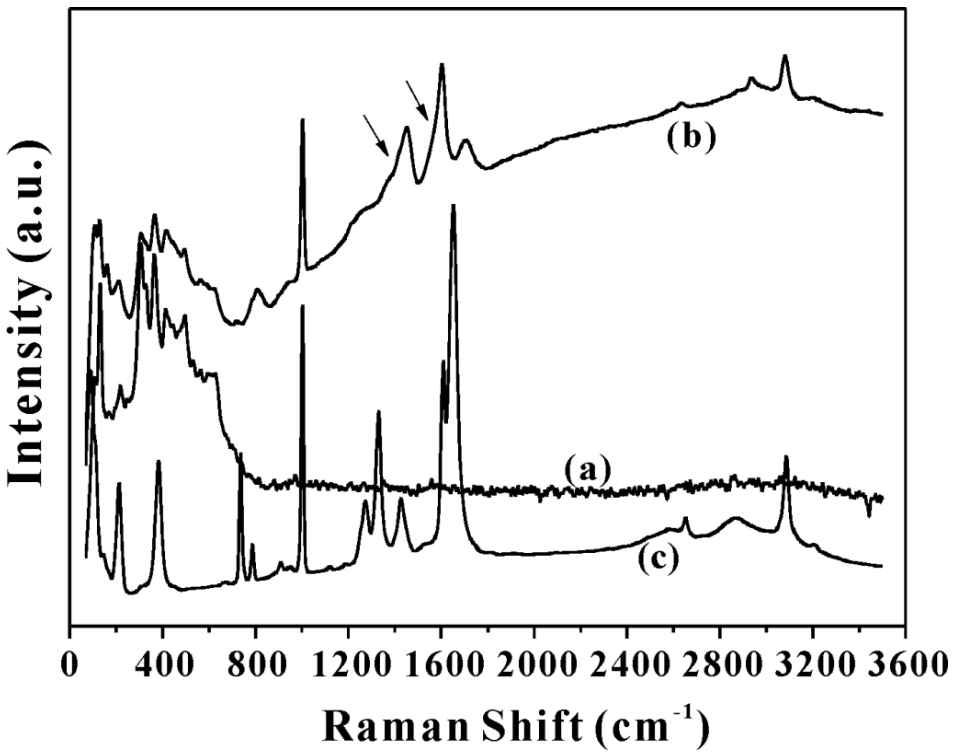

Figure 5-3: The Raman spectra of (a) the bare ITO; (b) TMA-adsorbed ITO nanoparticles and (c) solid TMA. Arrows show possible peak overlappings.

In contrast, the band of C=O stretching in carboxyl group is shifted from 1652 cm^{-1} of solid TMA to 1705 cm^{-1} of the adsorbed TMA. The lower

frequency of C=O stretching in solid TMA was attributed to the in-phase mode of dimeric carboxylic acids formed by strong intermolecular hydrogen bonding.[13-14] The band situated at 1452 cm^{-1} is resulted from the ν_{19b} benzene ring mode.[14] The corresponding possible assignments are listed in Table 5-1, based on the previous reports.[14-16] The Raman spectra suggest that TMA molecules have been successfully attached to ITO nanoparticles.

Table 5-1: The Raman bands for solid and adsorbed TMA and the possible assignments.

Frequency (cm^{-1})		**Assignment**
Solid TMA	**Adsorbed TMA**	
3084 m	3081 m	ν(CH)
1652 s		ν(C=O)
	1705 w	ν(C=O)
1608 s	1603 s	8a, ν(CC)
	1452 m	19b, ν(CC)
1425 m		
1330 s		14
1271 m		3
1001 s	1002 s	1, ν(CC)
	806 w	
786 w		11
735 s		4

Abbreviations: s, strong; m, medium; w, weak.

One should be noted that there are broad tails associated with the bands situated at 1603 and 1452 cm^{-1}, as indicated by the arrows in Figure 5-3b. The broad tail below 1603 cm^{-1} is presumably due to the overlapping between ν_{8a} ring mode and $\nu_{as}(COO^-)$ asymmetric stretching.[15] The other tail might be attributed to the overlapping between ν_{19b} band and $\nu_s(COO^-)$ symmetric stretching mode.[15-16] This might indicate the formation of carboxylate between ITO nanoparticles and TMA molecules.

Diffuse Reflectance Infrared Fourier Transform Spectroscopy

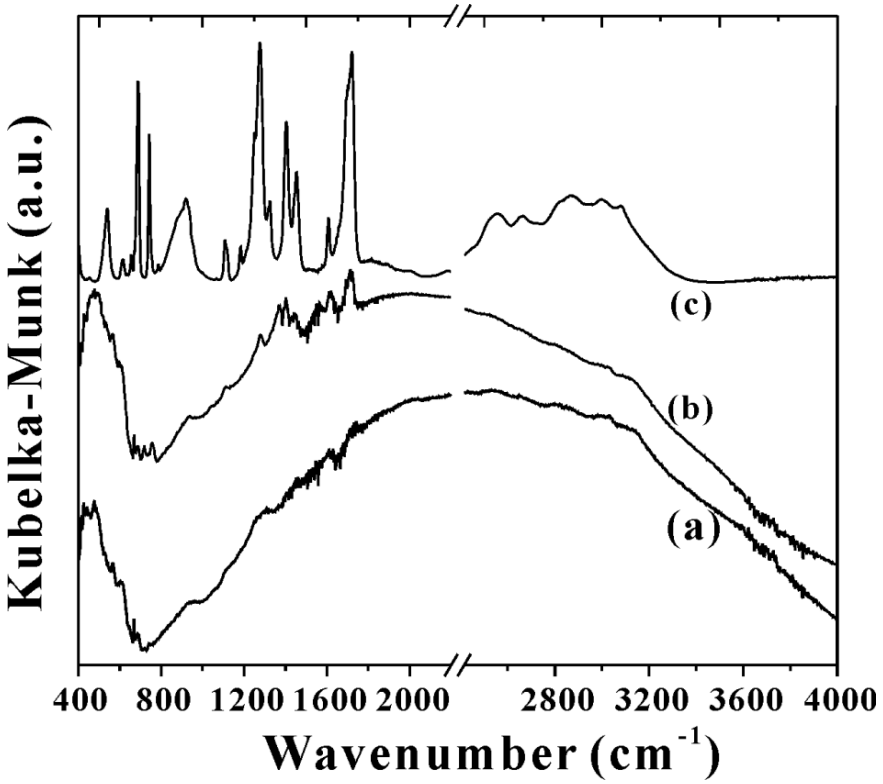

Figure 5-4: The DRIFT spectra of (a) the bare ITO; (b) TMA-adsorbed ITO nanoparticles and (c) solid TMA.

In order to learn the adsorption behaviors, DRIFTS was carried out to study the adsorption of TMA molecules on ITO nanoparticles. As shown in Figure 5-4a and 4b, several new absorption bands located at 1714, 1616, 1567, 1450, 1370 and 1280 cm^{-1} etc., could be readily observed for the ITO nanoparticles

modified by TMA molecules. The appropriate assignments have been tabulated in Table 5-2, according to the reported works.[2-3, 14-17] By comparing the three spectra, we can easily discern the two new bands sitting at 1370 cm^{-1} and 1567 cm^{-1}, respectively. The two new bands are ascribed to the typical symmetric (ν_s) and asymmetric (ν_{as}) stretching modes of COO^-. This may support the Raman results that TMA molecules are attached onto ITO nanoparticles to form carboxylates.

Table 5-2: The DRIFTS and FTIR absorption bands of TMA.

Solid TMA (DRIFTS & FTIR)	**Adsorbed TMA**		**Assignment**
	DRIFTS	**FTIR**	
1716 s	1714 s	1715 w	ν(C=O)
1606 m	1616 s	1619 s	8a, ν(CC)
	1567 w	1567 w	$\nu_{as}(COO^-)$
1452 s	1450 w	1439 s	19b, ν(CC)
1403 s	1403 s		
	1370 s	1370 s	$\nu_s(COO^-)$
1323 m			14
1275 s	1280 s		3
1252 m			ν(C-O)
1182 w			
1110 m	1113 w		18b
918 b	938 w		
743 s	756 s	756 s	γ(CH)

	718 s	720 w	
686 s	689 w		

Abbreviations: s, strong; m, medium; w, weak; b, broad.

Transmission Fourier Transform Infrared Spectroscopy

As shown in DRIFT spectra, the vibrational features of adsorbed TMA molecules are located in the region from 1200 cm^{-1} to 1800 cm^{-1}. Due to the strong absorption of water vapor within this range, the signal to noise ratio is not very high. Therefore, transmission FTIR was used to further examine the adsorption of TMA molecules on ITO nanoparticles. Figure 5-5 shows the FTIR spectra of the bear ITO nanoparticles, TMA-adsorbed ITO nanoparticles and pure solid TMA.

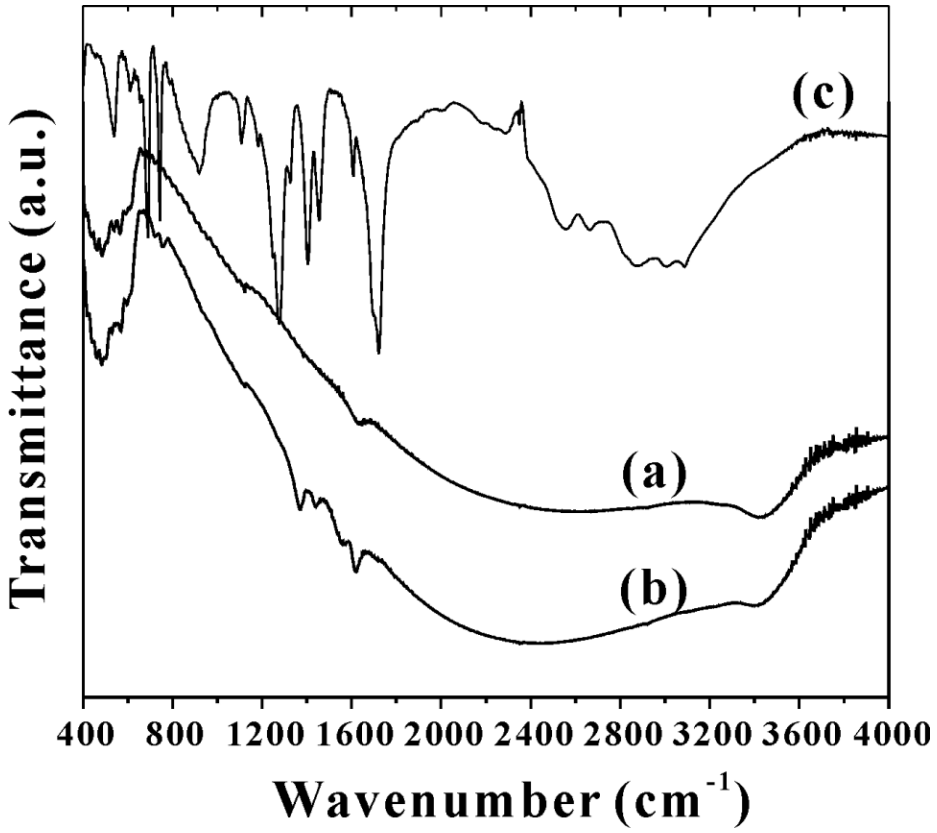

Figure 5-5: The FTIR spectra of (a) the bare ITO; (b) TMA-adsorbed ITO nanoparticles and (c) solid TMA.

As presented in Figure 5-5b, ITO nanoparticles with adsorbed TMA molecules show several new absorption bands at 1567, 1439 and 1370 cm^{-1}, etc., compared with the bare ITO nanoparticles. The corresponding assignments are also proposed in Table 5-2. Obviously, the two new absorption bands at 1370 and 1567 cm^{-1} are in good agreement with the DRIFTS result, suggesting the formation of carboxylates upon adsorption of TMA molecules onto ITO nanoparticles. The band at 1628 cm^{-1} for ITO nanoparticles prior to the adsorption of TMA is probably due to the scissoring mode of chemisorbed water molecules.[18]

X-ray Photoelectron Spectroscopy

The adsorption of trimesic acid on ITO nanoparticles has been further characterized by X-ray photoelectron spectroscopy. The XPS survey scans (Figure 5-6a and 6b) suggest that except In, Sn, O and C, no discernible elements exist on ITO nanoparticles before and after the adsorption of TMA. According to the In3d and Sn3d core-level XPS spectra (Figure 5-6c to 5-6f), no significantly different features can be detected, such as the peak positions and shapes, between the ITO nanoparticles before and after the adsorption of TMA.

However, the O1s and C1s XPS spectra have displayed remarkably different features for ITO nanoparticles with and without the adsorption of TMA. Figure 5-7a shows the O1s XPS spectrum of ITO nanoparticles with the adsorption of TMA molecules. The O1s peak can be fitted into four components designated as O1, O2, O3 and O4. The components of O1 and O2 centering at 529.9 and 530.5 eV are due to the species of lattice oxygen and surface hydroxyl group, respectively. O3 and O4 can be attributed to the

carboxylate and carbonyl group moiety, situated at 531.5 eV and 532.5 eV, respectively.[2, 19]

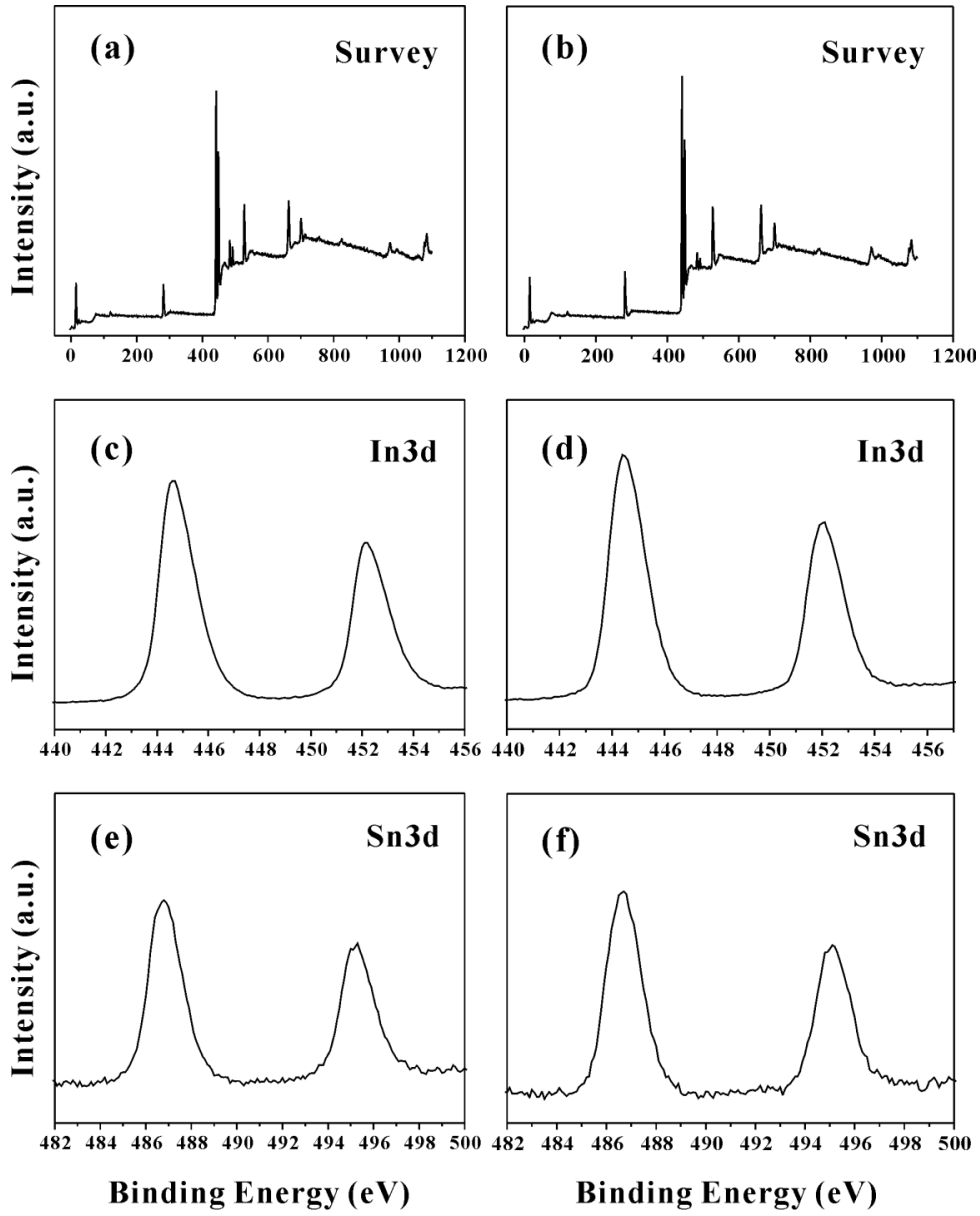

Figure 5-6: The XPS spectra of ITO nanoparticles before (a, c, e) and after (b, d, f) the adsorption of TMA molecules.

The O1s spectrum of ITO nanoparticles before the adsorption of TMA was also collected and the result is shown in Figure 5-7b as the comparison. Due to the surface OH and chemisorbed water on ionic metal oxide surface from the atmospheric preparation condition, a broad tail at higher binding energy of O1s spectrum can be observed frequently. To reduce their interferences in

peak assignment, here the peak fitting is conducted by following the same parameters as used in Figure 5-7a. The results show that the relative ratios of O3/O1 and O4/O1 were increased significantly from 0.47 to 0.8 and 0.33 to 0.65 respectively after the adsorption of TMA. Although the ratio of O2/O1 was also enhanced (from to 0.33 to 0.48), the results still can suggest that trimesic acid has attached onto the surface of ITO nanoparticles.

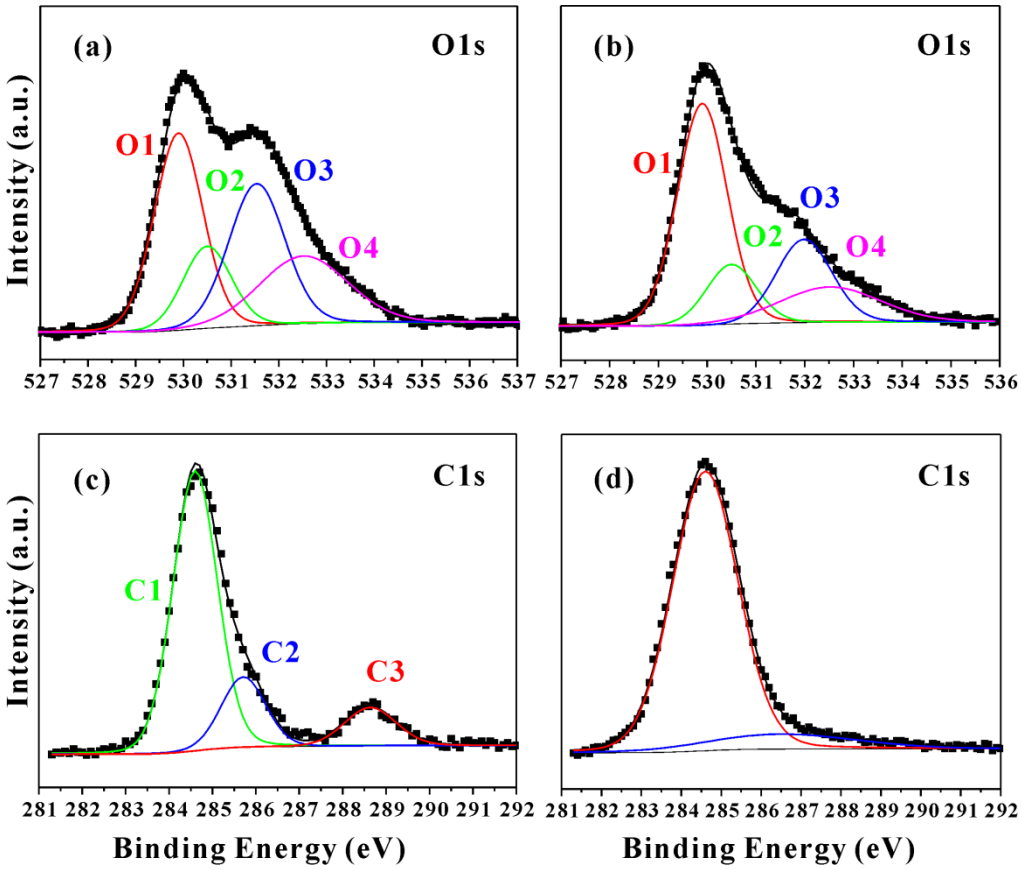

Figure 5-7: The O1s and C1s core-level XPS spectra of ITO nanoparticles with (a, c) and without (b, d) the adsorption of TMA molecules.

The statement can be further consolidated by the C1s XPS spectra. Figure 5-7c presents the C1s core-level spectrum of ITO nanoparticles after the adsorption of TMA. As can be seen, the peak comprises of three species, C1, C2 and C3. The first two are associated with the aliphatic carbon (284.6 eV) and C-O related carbon (285.7 eV) which can be frequently observed on metal

oxides. However, C3 component siting at high binding energy of 288.6 eV undoubtedly suggests the existence of carboxylate or carbonyl carbon on ITO surface.[2, 19] In contrast, ITO nanoparticles without the adsorption of TMA do not show any observable high binding energy peak (Figure 5-7d). Based on the detailed analysis discussed above, the XPS measurement suggests that trimesic acid molecules have been adsorbed on ITO nanoparticles to form carboxylate.

5.3.3 Adsorption of TMA on ITO (111) Surface

As discussed in the previous section, various spectroscopic results have consolidated the conclusion that trimesic acid molecules have been successfully attached onto ITO nanoparticles. However, they do not provide more information about the adsorption behaviors, such as adsorption geometry, adsorption site, etc. Therefore, in this section, the density functional theory was used to study the adsorption behavior of TMA on the ITO surface.

The (111) surface of bixbyite indium oxide is the most stable surface as it shows the lowest surface energy among the three low-index surfaces: $\gamma(100)>\gamma(110)>\gamma(111)$.[20-24] XRD patterns also confirm the (111) preferred orientation of In_2O_3 (data not shown) and ITO nanoparticles (Figure 5-1).

As shown in Figure 5-8, the ITO (111) surface slab consists of two stoichiometric ionic layers with each layer containing 15 In, 1 Sn and 24 O atoms. Each stoichiometric layer is non-polar in nature due to the charge neutral repeating unit of O_{12}-In_{16}(Sn)-O_{12} along the <111> direction.[21] Different from the (100) surface where oxygen dimmers[25] are formed to stabilize the polar surface, no significant structural reconstruction could be observed after geometrical relaxation of the ITO (111) surface.

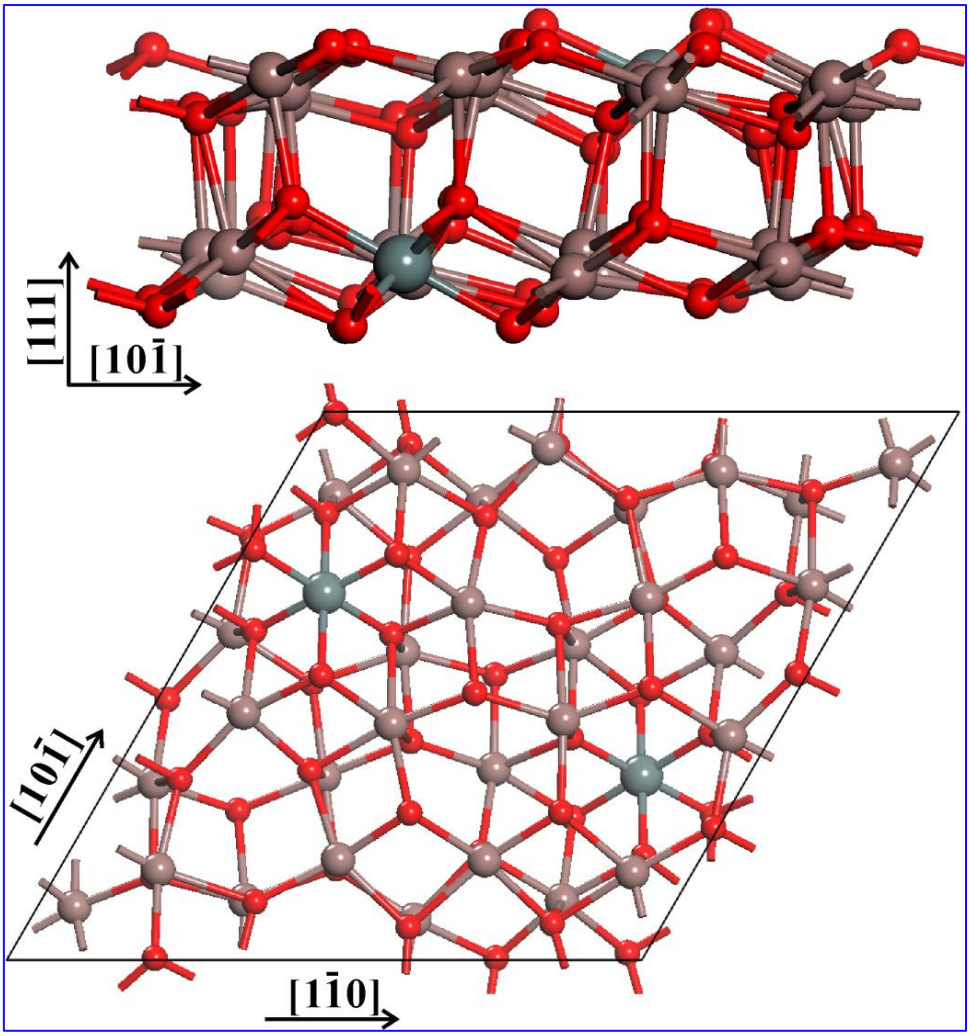

Figure 5-8: The side view and top view of the relaxed ITO (111) surface slab. Red, brown and grey balls denote oxygen, indium and tin atoms, respectively.

In ITO bulk, the coordination numbers of indium and oxygen are six and four, whereas on the surface, the coordination numbers are reduced to five and three, respectively. The top layer of ITO (111) surface slab is presented in Figure 5-9 to show the under-coordinated In and O atoms on surface. The clean (111) surface has 12 five-coordination indium and 12 three-coordination oxygen atoms, which are labeled to investigate possible adsorption sites (discuss later). The most stable structure of trimesic acid is also presented in Figure 5-9. The molecule is three-fold symmetrically planar with the size about 8 angstroms.

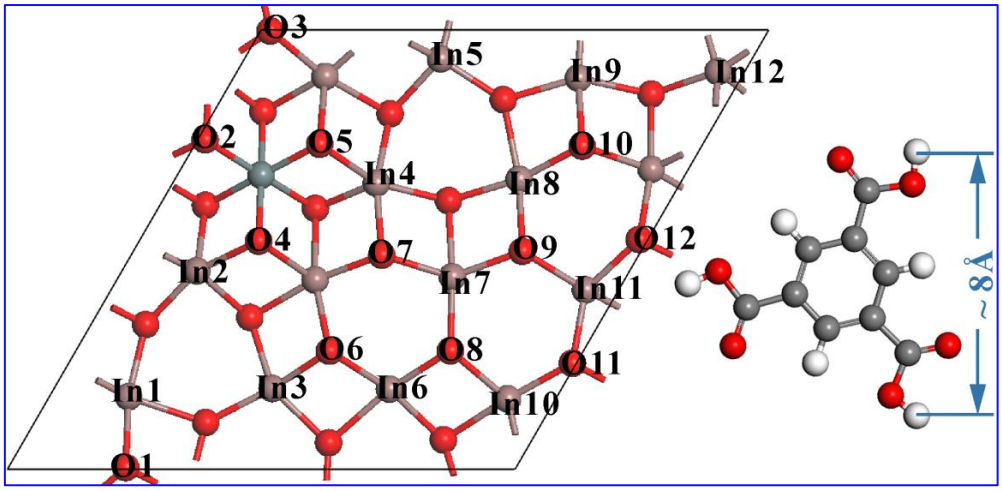

Figure 5-9: The ITO (111) slab with the surface atoms labeled (left) and the optimized structure of trimesic acid (right). Red, brown and grey balls denote oxygen, indium and tin atoms, respectively.

The previous works have shown that trimesic acids would like to be adsorbed on the rutile TiO_2 (110), Cu (110) and Au (111) surfaces via a flat-lying configuration.[2-3, 17, 26] However, our computations show that TMA does not prefer a flat-lying configuration on the ITO (111) surface. All the relaxations starting from a flat-lying structure give a tilted geometry with the carbonyl oxygen adsorbed onto one under-coordinated indium (data not shown).

Besides the flat-lying configurations, we have also calculated possible upstanding adsorption geometries. Since the energy variation during the geometrical optimization might be trapped at the local minimum, here we have considered a large amount of different adsorption configurations. The combination of the 12 indium sites and 12 oxygen sites gives rise to 24 possible adsorption configurations. The geometrical optimization of them all gives a stable structure.

Figure 5-10 shows the six most stable configurations. All the benzene rings of adsorbed TMA molecules are tilted slightly with respect to the surface

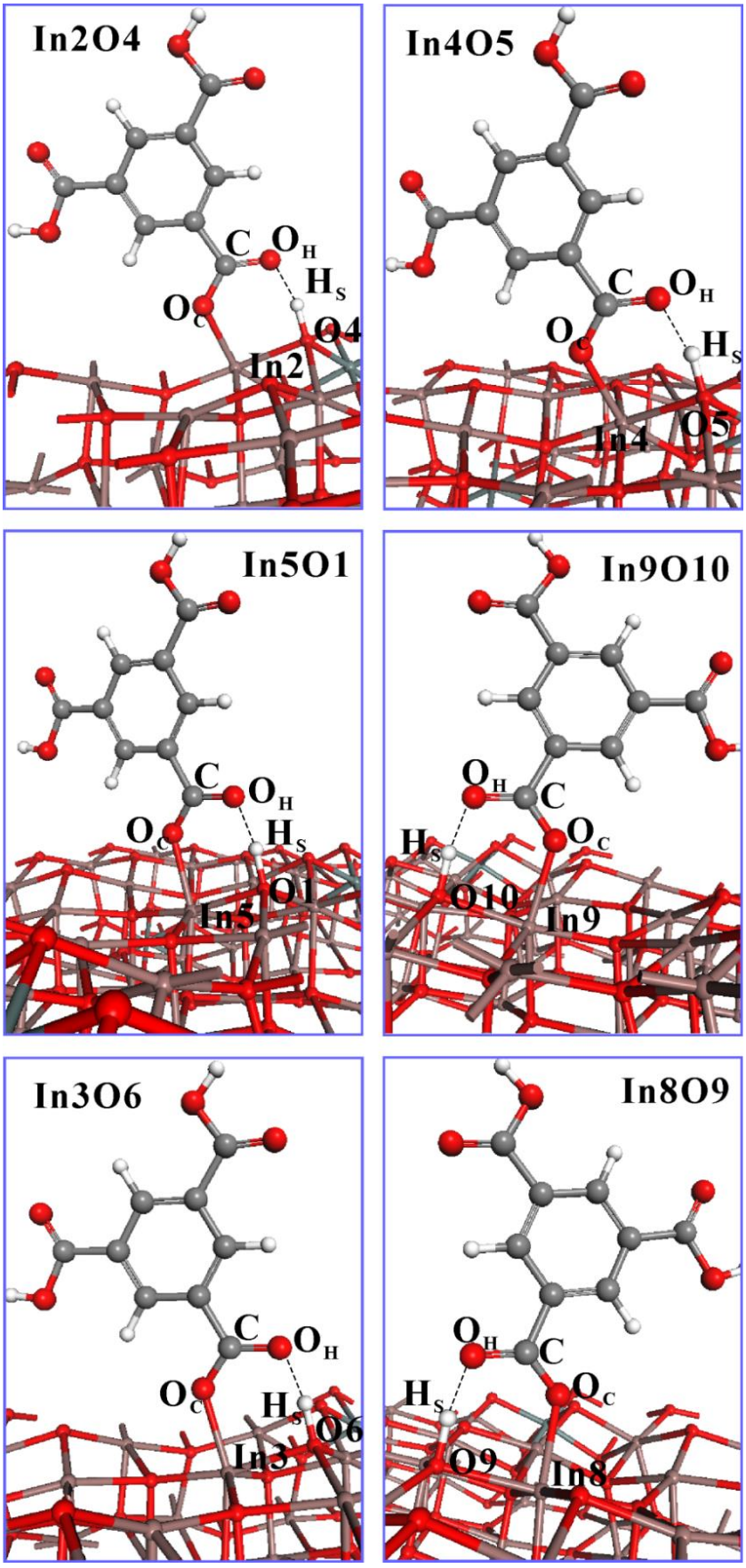

Figure 5-10: Perspective view of the six most stable structures of TMA adsorbed on ITO (111) surface.

normal. The free TMA molecule is a planar structure with all the three carboxylic groups and benzene ring on a same plane. In the adsorbed TMA, the benzene ring and two carboxylic groups far away from the surface remain on the same plane. However, the third carboxylic group is distorted after it forms chemical bonds with the ITO (111) surface.

Including the six configurations shown in Figure 5-10, all TMA molecules are spontaneously dissociated after being adsorbed onto the ITO (111) surface. For the convenience of description, we designate C and O_C as the carbon and oxygen atoms in the carbonyl group of TMA, as shown in Figure 5-10. O_H refers to the oxygen atom in the hydroxyl group. H_S stands for the hydrogen adsorbed on the surface, which originally belongs to the carboxylic group.

To evaluate the total energy variation of different configurations, here we define the dissociative chemisorption energy (ΔE) by Equation (5-1):

$$\Delta E = E_{(TMA+surface)} - E_{(TMA)} - E_{(surface)} \quad (5\text{-}1)$$

where $E_{(TMA+surface)}$, $E_{(TMA)}$ and $E_{(surface)}$ refer to total energies of the relaxed TMA-adsorbed surface slab, the relaxed free TMA molecule and the optimized clean surface respectively.

Table 5-3 lists the dissociative chemisorption energies and structural parameters of TMA molecules in the 24 relaxed configurations. For all 24 configurations, the bond lengths within the benzene ring and two farthest carboxylic groups remain intact compared with the free trimesic acid. The C-C bond between the benzene ring and third carboxylic group is slightly increased by 0.01 Å to 1.50 Å.

The bond lengths of In-O_C vary from 2.20 to 2.28 Å for all the optimized configurations, which are not significantly different from the surface In-O

Table 5-3: The bond lengths and dissociative chemisorption energies of the 24 possible adsorption configurations.

In_xO_y	In_x-O_c (Å)	O_y-H_s (Å)	C-O_c (Å)	C-O_H (Å)	O_H...H_s (Å)	ΔE (eV)
TMA			1.22	1.36	0.98	
In2O4	2.23	1.05	1.30	1.26	1.49	-1.416
In4O5	2.23	1.05	1.30	1.26	1.52	-1.411
In5O1	2.20	1.06	1.30	1.26	1.48	-1.329
In9O10	2.20	1.05	1.30	1.26	1.50	-1.328
In3O6	2.20	1.05	1.30	1.26	1.50	-1.325
In8O9	2.23	1.05	1.29	1.26	1.48	-1.304
In1O11	2.24	1.06	1.29	1.27	1.45	-1.298
In2O12	2.23	1.04	1.30	1.26	1.54	-1.298
In6O8	2.22	1.05	1.29	1.26	1.49	-1.297
In12O3	2.22	1.04	1.30	1.26	1.55	-1.297
In4O7	2.22	1.03	1.30	1.26	1.62	-1.287
In8O10	2.22	1.06	1.29	1.27	1.47	-1.189
In6O6	2.22	1.06	1.29	1.27	1.47	-1.188
In1O1	2.25	1.09	1.29	1.27	1.39	-1.186
In11O12	2.27	1.10	1.28	1.27	1.36	-0.941
In7O7	2.28	1.11	1.28	1.27	1.35	-0.940
In10O3	2.27	1.10	1.28	1.27	1.37	-0.935
In12O2	2.25	1.10	1.28	1.27	1.38	-0.929
In7O8	2.27	1.13	1.27	1.28	1.32	-0.857
In11O9	2.27	1.13	1.27	1.28	1.32	-0.853

In10O8	2.26	1.10	1.28	1.28	1.37	-0.846
In11O11	2.26	1.10	1.28	1.28	1.38	-0.841
In10O11	2.27	1.12	1.27	1.28	1.34	-0.839
In7O9	2.25	1.09	1.29	1.27	1.39	-0.833

bond lengths. However, after the adsorption and dissociation of TMA on the surface, the C-O_C bond is significantly elongated from 1.22 Å to about 1.3 Å. In contrast, the C-O_H bond is considerably shortened from 1.36 Å to about 1.27 Å. The two C-O bonds become close to each other, implying the formation of carboxylate,[1] which strongly supports the spectroscopic results discussed in Section **5.4.2**.

The Bader charge analysis[27-29] shows that the dissociation of O-H bond causes a very minor electron transfer from TMA to the ITO (111) surface. The net charges of the several important atoms are tabulated in Table 5-4. In all 24 adsorption configurations, the hydroxyl hydrogen is dissociated onto the surface, as indicated by the net Bader charge Q(H_s). Compared with free TMA, a redistribution of the charge within carboxylic group occurs after it is adsorbed onto the ITO surface. As shown in Table 5-4, the carbonyl carbon (O_c) loses partial electron which is redistributed when the carboxylate forms.

Table 5-4: The Bader atomic charges in the 24 possible adsorption configurations.

In_xO_y	**Q(In_x)**	**Q(O_y)**	**Q(C)**	**Q(O_c)**	**Q(O_H)**	**Q(H_s)**
TMA			+1.48	-1.10	-1.08	+0.63
In2O4	+1.63	-1.22	+1.51	-1.15	-1.13	+0.68

In4O5	+1.63	-1.21	+1.50	-1.14	-1.14	+0.67
In5O1	+1.62	-1.15	+1.48	-1.14	-1.10	+0.65
In9O10	+1.62	-1.15	+1.48	-1.14	-1.11	+0.65
In3O6	+1.63	-1.14	+1.52	-1.13	-1.11	+0.64
In8O9	+1.62	-1.15	+1.55	-1.13	-1.16	+0.63
In1O11	+1.62	-1.15	+1.54	-1.14	-1.14	+0.64
In2O12	+1.63	-1.15	+1.53	-1.14	-1.16	+0.63
In6O8	+1.62	-1.19	+1.51	-1.13	-1.13	+0.67
In12O3	+1.63	-1.15	+1.53	-1.14	-1.14	+0.63
In4O7	+1.63	-1.19	+1.54	-1.13	-1.14	+0.67
In8O10	+1.62	-1.16	+1.52	-1.14	-1.14	+0.67
In6O6	+1.62	-1.13	+1.55	-1.15	-1.16	+0.64
In1O1	+1.62	-1.13	+1.51	-1.13	-1.15	+0.65
In7O7	+1.63	-1.13	+1.55	-1.14	-1.13	+0.61
In10O3	+1.63	-1.13	+1.55	-1.12	-1.15	+0.61
In12O2	+1.62	-1.12	+1.52	-1.12	-1.13	+0.62
In7O8	+1.63	-1.13	+1.53	-1.12	-1.15	+0.62
In11O9	+1.62	-1.12	+1.55	-1.11	-1.15	+0.61
In10O8	+1.63	-1.15	+1.53	-1.13	-1.16	+0.64
In11O11	+1.63	-1.14	+1.52	-1.13	-1.12	+0.62
In10O11	+1.63	-1.15	+1.55	-1.11	-1.15	+0.65
In7O9	+1.63	-1.14	+1.52	-1.13	-1.13	+0.62
In11O12	+1.62	-1.01	+1.52	-1.04	-1.04	+0.62

5.3.4 Cyclic Voltammetry

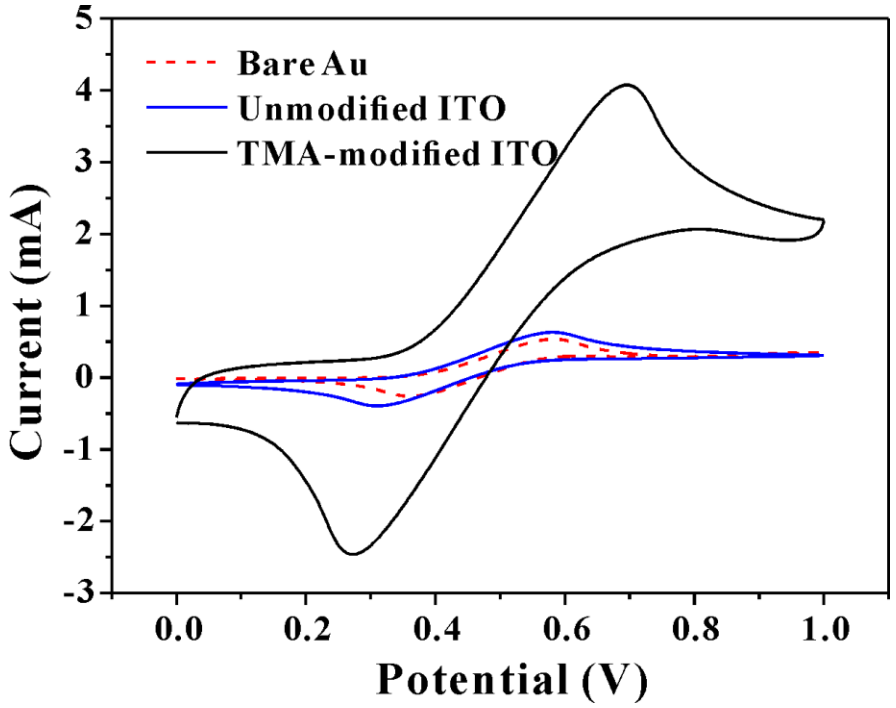

Figure 5-11: The normalized cyclic voltammograms of different electrode materials towards 1 mM Fc/Fc^+ in CH_3CN. (Scan rate: 50 mV/s)

The adsorption of TMA can alter the surface electronic properties and richen the surface chemistry of ITO nanoparticles for further modification. We have applied the TMA-adsorbed ITO nanocrystals in cyclic voltammetry measurement to examine the surface reactivity. The supporting electrolyte consists of 0.25 M $LiClO_4$/Acetonitrile containing probe molecules of 1 mM ferrocene (Fc). Figure 5-11 shows the CV behaviors for Fc/Fc^+ on the bare Au electrode, Au electrodes covered with different ITO nanoparticles. The bare gold electrode shows a very weak electrocatalytic effect towards Fc/Fc^+ redox couple, as indicated by the low peak currents of both oxidation (0.54 mA) and reduction (0.26 mA) sweeps. The Au electrode covered by the ITO nanoparticles without modification also displays a similarly weak electrocatalytic performance (Oxidation sweep: 0.63 mA, reduction sweep: 0.39 mA).[30] In contrast, the TMA-adsorbed ITO nanoparticles exhibit

significantly increased peak currents of more than six-fold (Oxidation sweep: 4.1 mA, reduction sweep: 2.5 mA). This implies that the adsorbed TMA molecules can effectively enhance the charge-transfer rate and electrocatalysis effect.[30-31] The modification of ITO surface with trimesic acids might be helpful to improve the efficiency of organic light emitting devices and organic photovoltaics, where rapid charge transfer through ITO surface is desired.[30-32]

5.4 Conclusion

To sum up, we have synthesized ITO nanocrystals with a uniformly small size of about 10 nm. Trimesic acid molecules were used to modify the ITO nanoparticles. The adsorption of TMA molecules on ITO nanoparticles was characterized by various spectroscopic techniques. To understand the adsorption behaviors, we have further studied the adsorption of TMA on the ITO (111) surface by the density functional theory. The conclusion is drawn as follows:

(1) The Raman, DRIFT, FTIR and XPS spectra indicate that TMA molecules are adsorbed on ITO nanoparticles to form carboxylate species.

(2) Computational results reveal that TMA molecules prefer an upstanding configuration on the ITO (111) surface, rather than the flat-lying adsorption geometry. The dissociation of O-H bond was found to spontaneously occur to form the carboxylate between TMA and ITO (111) surface. The theoretical studies strongly support the experimental results.

(3) The TMA-adsorbed ITO nanoparticles have shown significantly enhanced electrocatalysis effect towards ferrocene.

References

1. Armstrong, N. R.; Veneman, P. A.; Ratcliff, E., et al., *Accounts Chem. Res.* **2009,** *42*, 1748-1757.
2. Classen, T.; Lingenfelder, M.; Wang, Y., et al., *J. Phys. Chem. A* **2007,** *111*, 12589-12603.
3. Li, Z.; Han, B.; Wan, L. J., et al., *Langmuir* **2005,** *21*, 6915-6928.
4. Almeida Paz, F. A.; Klinowski, J., *Inorg. Chem.* **2004,** *43*, 3882-93.
5. Goebbert, C.; Nonninger, R.; Aegerter, M. A., et al., *Thin Solid Films* **1999,** *351*, 79-84.
6. Kresse, G.; Furthmuller, J., *Comput. Mater. Sci.* **1996,** *6*, 15-50.
7. Kresse, G.; Furthmuller, J., *Phys. Rev. B* **1996,** *54*, 11169-11186.
8. Blochl, P. E., *Phys. Rev. B* **1994,** *50*, 17953-17979.
9. Kresse, G.; Joubert, D., *Phys. Rev. B* **1999,** *59*, 1758-1775.
10. Perdew, J. P.; Burke, K.; Ernzerhof, M., *Phys. Rev. Lett.* **1996,** *77*, 3865-3868.
11. Mryasov, O. N.; Freeman, A. J., *Phys. Rev. B* **2001,** *64*, 233111.
12. Monkhorst, H. J.; Pack, J. D., *Phys. Rev. B* **1976,** *13*, 5188-5192.
13. Tourwé, E.; Baert, K.; Hubin, A., *Vib. Spectrosc.* **2006,** *40*, 25-32.
14. Mayo, D. W., *Course Notes on the Interpretation of Infrared and Raman Spectra*, John Wiley & Sons, Inc., **2004**, 101-140.
15. Arenas, J. F.; Montañez, M. A.; Otero, J. C., et al., *Vib. Spectrosc.* **1993,** *4*, 159-165.
16. Kim, Y.; Cho, K.; Lee, K., et al., *J. Mol. Struct.* **2008,** *878*, 155-161.
17. Han, B.; Li, Z. H.; Wandlowski, T., *Anal. Bioanal. Chem.* **2007,** *388*, 121-129.

18. Noei, H.; Qiu, H.; Wang, Y., et al., *Phys. Chem. Chem. Phys.* **2008,** *10*, 7092-7097.

19. Zhang, W.; Cao, L.; Wan, L., et al., *J. Phys. Chem. C* **2013,** *117*, 21351-21358.

20. Pussi, K.; Matilainen, A.; Dhanak, V. R., et al., *Surf. Sci.* **2012,** *606*, 1-6.

21. Walsh, A.; Catlow, C. R. A., *J. Mater. Chem.* **2010,** *20*, 10438-10444.

22. Paramonov, P. B.; Paniagua, S. A.; Hotchkiss, P. J., et al., *Chem. Mater.* **2008,** *20*, 5131-5133.

23. Li, H.; Paramonov, P.; Bredas, J. L., *J. Mater. Chem.* **2010,** *20*, 2630.

24. Agoston, P.; Albe, K., *Phys. Rev. B* **2011,** *84*, 045311.

25. Zhou, C. G.; Li, J. Y.; Chen, S., et al., *J. Phys. Chem. C* **2008,** *112*, 14015-14020.

26. Andreas, G.; Philipp, R.; Marcin, K., et al., *J. Phys. Condens. Mat.* **2010,** *22*, 345008.

27. Tang, W.; Sanville, E.; Henkelman, G., *J. Phys. Condens. Mat.* **2009,** *21*, 084204.

28. Sanville, E.; Kenny, S. D.; Smith, R., et al., *J. Comput. Chem.* **2007,** *28*, 899-908.

29. Henkelman, G.; Arnaldsson, A.; Jónsson, H., *Comput. Mater. Sci.* **2006,** *36*, 354-360.

30. Carter, C.; Brumbach, M.; Donley, C., et al., *J. Phys. Chem. B* **2006,** *110*, 25191-25202.

31. Donley, C.; Dunphy, D.; Paine, D., et al., *Langmuir* **2001,** *18*, 450-457.

32. Armstrong, N. R.; Carter, C.; Donley, C., et al., *Thin Solid Films* **2003,** *445*, 342-352.

Chapter 6

Summary and Future Work

6.1 Summary

A simple and effective solution process has been developed to prepare transparent conductive Sn-doped In_2O_3 thin films. The effective chelation of Sn^{4+} by acetylacetone was found to facilitate the formation of more uniform and smooth film microstructures. As a consequence, ITO thin film with a high transparency (90.2%) and low resistivity (7.2×10^{-4} Ω·cm) can be obtained. The highest figure of merit was achieved among all solution-processed ITO films, even comparable to that of the polycrystalline ITO film produced by DC magnetron sputtering. The high transparency, low sheet resistance (30 Ω/sq) and low surface roughness (1.14 nm) can meet the requirements for most practical applications. This makes the sol-gel process highly attractive for fabrications of TCO films at a large scale for broader optoelectronic applications.

Besides Sn, other group IVA elements, especially Si and Ge, are possibly effective n-type dopants for In_2O_3. DFT calculation was employed to investigate the geometrical and electronic structures of In_2O_3 substitutionally doped with the group IVA and other n-type dopants. The electronic structures revealed that the *n*s states of dopants, Si, Ge and Sn, are strongly hybridized with the O-*2p* states. Compared with other dopant elements, the three dopants would not alter the conduction band features of In_2O_3 host. The electrons were found to be more effectively delocalized in Si-, Ge- and Sn-doped In_2O_3 lattice.

Therefore, a large band width (>2 eV), low effective mass ($0.2m_0$) and high electron group velocity (>8.3×10^5 m/s) near Fermi level can be achieved. The low formation energies imply the large abundance of neutral and +1 charge state Ge and Sn dopant atoms under both oxygen-rich and indium-rich conditions. In contrast, Si only more possibly exists under indium-rich condition. Given the real oxygen-poor condition, Sn might be the most preferred dopant. Considering the superior electronic and transport properties, it can be understood that Sn-doped indium oxide is the most widely used In_2O_3-based TCO film.

DFT calculation has also been employed to design a new transparent conducting material using hexagonal GaS. The conduction band minimum (CBM) of two-dimensional GaS was mainly contributed by the highly delocalized Ga *4s* states. The hydrogenation of sulfur atom was found to increase the electrical conductivity of GaS by contributing electrons into the conduction band near CBM. A pronounced Burstein-Moss shift could enhance the visible transparency by increasing the optical band energy. The carrier transport properties of the H-doped GaS reveal a low resistivity (e.g. 2.43×10^{-4} Ω·cm) which is comparable with that of benchmark transparent conducting films. The fundamental study might be helpful to develop a novel two-dimensional GaS transparent conductor.

Trimesic acid (TMA) was utilized to modify ITO nanoparticles. The Raman, DRIFT, FTIR and XPS spectra indicated that TMA molecules were adsorbed on ITO nanoparticles to form carboxylate species. Computational investigations reveal that TMA molecules prefer an upstanding configuration on the ITO (111) surface, rather than the flat-lying adsorption geometry. The

dissociation of O-H bond can spontaneously occur to form carboxylate between TMA and ITO (111) surface, which strongly supports the experimental results. The TMA-adsorbed ITO nanoparticles have shown a significantly enhanced electro-catalysis effect towards the probe molecules of ferrocene, compared with the unmodified counterpart. The modification of ITO films by TMA might be useful to improve the charge transport efficiency in organic electronics, such as organic light-emitting diodes and organic solar cells.

6.2 Limitations and Future Work

The ITO films prepared by our solution process show a decreased resistivity after the annealing in H_2/Ar gas mixture. Due to the inaccessibility of necessary instruments, the origin of this improvement is not well understood. A Hall-effect measurement is extremely helpful to understand the origin. For example, it is due to an increased carrier concentration and/or an enhanced mobility.

Low-temperature deposition of transparent conducting oxide thin films is highly desired for flexible electronics where the commonly used polymer substrates cannot sustain high temperature (e.g. polyethylene terephthalate, T_g~80 ^oC). We have synthesized various metal ligand (hexafluoroacetylacetonate, HFAC) compounds, such as $In(HFAC)_3$, $Sn(HFAC)_2$, $Zn(HFAC)_2$, $Ga(HFAC)_3$ and $Al(HFAC)_3$ (data not shown in this thesis). Each shows a low decomposition temperature less than 150 ^oC. Therefore, they are highly promising precursors for the low-temperature deposition of transparent conducting oxide thin films, such as amorphous

IGZO, ITO, AZO and GZO films. Due to the time constraint, this work was not completed.

Appendix

The computations discussed in this thesis were performed by the software of Vienna Ab-initio Simulation Package, well known as VASP. The basic methodology of the calculations is the density functional theory (DFT) which predicts that the electronic properties of a system are solely related to its electron density. The fundamental theory of DFT will be briefly introduced below.

1. Born-Oppenheimer Approximation

Considering that the mass of proton and neutron is much larger than that of an electron, the motions of nucleus and electron can be separated mathematically. The electrons can be viewed as moving in a set of fixed atomic nuclei. The Schrödinger equation of a many-body system including N electrons is expressed as:

$$[-\frac{\hbar^2}{2m}\sum_{i=1}^{N}\nabla_i^2+\sum_{i=1}^{N}V(r_i)+\sum_{i=1}^{N}\sum_{j<i}U(r_i,r_j)]\psi=E\psi$$

The three terms on the left are the kinetic energy of each electron, the interaction energy between each electron and the collection of atomic nuclei, and the interaction energy between different electrons. *m* refer to the electron mass. The electronic wave function of ψ is a function of each electrons by $\psi=\psi(r_1,r_2,...,r_N)$. *E* corresponds to the ground state energy of electrons.

As shown in the previous equation, the Schrödinger equation deals with many-body problems involving the interactions between many electrons. Solving the equation is too complicated. However, the problem can be simplified by approximating the full electron wave function by each

individual wave function as $\psi = \psi_1(r)\psi_2(r),...,\psi_N(r)$, known as Hartree product.

It is noticed that the probability that the N electrons are found at particular set of coordinates, $r_1, r_2, ...r_N$ equals to $\psi^*(r_1,...,\mathrm{r}_N)\psi(r_1,...,r_N)$ (asterisk refer to the complex conjugate). In experiment, it is more of physical interest to find the electron density at a particular position, which can be expressed as:

$$n(r) = 2\sum_i \psi_i^*(r)\psi_i(r)$$

2. Hohenberg-Kohn-Sham (HKS) theorem

The HKS theorem proves that: (1) the ground state energy from Schrödinger equation is a unique functional of the electron density ($E_0 = E(r)$); (2) at the equilibrium density $n_0(\mathrm{r})$, this functional $E(\mathrm{r})$ has the minimum relative to variations $\delta n(\mathrm{r})$ of the electron density.

The energy functional can be written in terms of single-electron wave functions of $\psi_i(r)$ as:

$$E[(\psi_i)] = E_{known}[(\psi_i)] + \mathrm{E}_{XC}[(\psi_i)]$$

The known term is written as:

$$E_{known}[(\psi_i)] = -\frac{\hbar^2}{m}\sum_i \int \psi_i^* \nabla^2 \psi_i d^3r + \int V(r)n(r)d^3r + \frac{e^2}{2}\iint \frac{n(r)n(r')}{|r-r'|}d^3r d^3r' + E_{ion}$$

The terms on the right correspond to the electron kinetic energies, the Coulomb interactions between electrons and nuclei, the Coulomb interactions between electron pairs and the Coulomb interactions between ions, respectively. The other term, $E_{XC}[(\psi_i)]$ is the exchange-correlation functional, defined to include all the quantum mechanical effects that excluded in the $E_{known}[(\psi_i)]$.

3. Kohn-Sham equation

K-S equation defines a way to find the electron density by solving a set of equations of each single electron by:

$$[-\frac{\hbar^2}{2m}\nabla^2 + V(r) + V_H(r) + V_{XC}(r)]\psi_i(r) = \varepsilon_i\psi_i(r)$$

The terms in the bracket refer to the kinetic energy of a single electron, the interaction energy between an electron and the collection of all nuclei, the Hartree potential describing the Coulomb repulsion between the specific electron and the total electron density and the exchange-correlation potential, respectively. The Hartree potential should include a self-interaction contribution, since the electron in the K-S equation we are solving is also part of the total electron density. The self-interaction and other effects are corrected in V_{XC} defined by:

$$V_{XC}(r) = \frac{\delta E_{XC}(r)}{\delta n(r)}$$

K-S equation is usually solved in an iterative way:

(1) Define an initial and trial electron density of $n(r)$;

(2) Solve K-S equations using $n(r)$ to find the wave functions of each electron, $\psi_i(r)$;

(3) Calculate the electron density from the wave functions obtained in step (2) by $n_{KS}(r) = 2\Sigma\psi_i^*(r)\psi_i(r)$;

(4) Compare the two electron densities of $n(r)$ and $n_{KS}(r)$. If both are same, the ground-state electron density is obtained. If not, the trial electron density is updated and steps from (2) will be repeated.

4. Exchange-Correlation Functional

4.1 Local Density Approximation (LDA)

To solve Equation (5), $E_{XC}(\psi_i)$ must be specified. The existence of the exchange-correlation functional has been proved by the Hohenberg-Kohn-Sham theorem, but its true form is unknown. Local Density Approximation uses uniform electron gas model by defining that the electron density is constant at all points in a space. At this situation, the exchange-correlation functional can be obtained exactly.

4.2 Generalized Gradient Approximation (GGA)

After LDA, another approach, known as generalized gradient approximation, was developed. GGA is more physically meaningful than LDA, since it considers the local gradient in the electron density. Many GGA functionals have developed by computational scientists, including a widely used one called Perdew-Burke-Ernzerhof functional (PBE).

5. Bloch theorem and Plane Waves

VASP code uses periodic boundary conditions for DFT calculation. The Bloch theorem proves that under periodic boundary condition the single electron wave function satisfies:

$$\psi_k(r) = u_k(r)\,\mathrm{e}^{ik\cdot r}$$

$$u_k(r+R) = u_k(r)$$

R is the translational vector and $u_k(r)$ is a periodic function.

Based on Bloch theorem, all periodic functions can be described as a sum of plane waves:

$$u_{n,k}(r) = \frac{1}{\Omega^{1/2}} \sum_G C_{Gnk} e^{iGr}$$

$$\psi_{n,k}(r) = \frac{1}{\Omega^{1/2}} \sum_G C_{Gnk} e^{i(G+k)r}$$

However, the basis set of *G* is infinite. In practice, only the plane waves |G+k| are considered, which meet the requirement of $\frac{\hbar^2}{2m_e} |G+k|^2 < E_{cutoff}$. A higher cutoff energy implies a more accurate result, but in the cost of more computational resources.

Due to a large number of electrons presenting in a system, the plane waves are also in a large amount which requires high computing cost. To simplify the basis of plane waves, pseudopotentials are used by treating the core-level electrons at the frozen core. As a result, the explicit description of core electrons and rapid oscillations of the wave function near nucleus can be avoided. Norm-conserving pseudopotentials smoothen the wave function within the sphere with the radius R_c, but maintaining the charge same as before the modification. Ultrasoft pseudopotentials can further reduce the basis sets of plane waves by further smoothening the wave functions.

6. Projector Augmented Wave

Projector Augmented Wave method was developed by combing the accuracy of full electron wave function method and the efficiency of pseudopotential method. The reconstruction of exact wave functions in the core region is achieved by decomposition of wave functions into three parts: pseudo wave function, pseudo onsite wave function and exact onsite wave function. These auxiliary wave functions are translated into the true wave functions by the transformation theory.

D.S. Sholl, J.A. Steckel, *Density Functional Theory: A Practical Introduction*, John Wiley & Sons Inc., **2009**, 1-31.